UNIVERSITY OF CALIFORNIA

Santa Barbara

The Role of Oxides in Nanostructured Ferritic Alloys and Bilayers: Interfaces, Helium Partitioning and Bubble Formation

A dissertation submitted in partial satisfaction of the

requirements for the degree Doctor of Philosophy

in Materials

by

Tiberiu Stan

Committee in charge:

Professor G. Robert Odette, Chair

Professor Carlos G. Levi

Professor Tresa M. Pollock

Professor Michael J. Gordon

June 2017

The dissertation of Tiberiu Stan is approved.

_____

Carlos G. Levi

_____

Tresa M. Pollock

_____

Michael J. Gordon

_____

G. Robert Odette, Committee Chair

March 2017

The Role of Oxides in Nanostructured Ferritic Alloys and Bilayers: Interfaces, Helium Partitioning and Bubble Formation

by

Tiberiu Stan

ACKNOWLEDGEMENTS

Before recognizing the many direct contributors to this research, I first want to sincerely thank my family for their boundless love and support throughout the years. I thank my parents, Marius and Liliana, for their sage advice and for being role model scientists who I look up to each day. I thank my sister Patricia for being a calm and loving presence in my life. I also thank my girlfriend Gursharan for her continuous encouragement and for her unmatched ability to make me laugh.

I thank my advisor, Professor G. Robert Odette, for initially taking me in as an undergraduate researcher, and for giving me the opportunity to turn the exciting bilayer project into a full PhD. His wisdom and guidance have been invaluable in helping me become a better scientist and engineer. I am grateful to have had an advisor who truly cared about my development and growth. I also thank my committee members, Prof. Tresa Pollock, Prof. Carlos Levi, and Prof. Michael Gordon, for their feedback and advice throughout my studies.

The past and present members of the UCSB Materials Performance and Reliability Group (MR&PG) have made significant contributions to this work and to my overall experience as a graduate student. Notably, most of the transmission electron microscopy sample preparation and characterization presented in this dissertation was done by Dr. Yuan Wu. She has worked with me side-by-side since the inception of these projects, and I am grateful for everything she has taught me. I thank Dr. Takuya Yamamoto for his help in optimizing experimental parameters, analysis of results, and many fruitful discussions throughout the years. Many of the projects would not have been possible without guidance

from David Gragg, Kirk Fields and Doug Klingensmith who helped me design and machine numerous parts and pieces. I also thank the other MR&PG group members: Dr. Peter Wells, Dr. Soupitak Pal, Dr. Md Alam, Dr. Nicholas Cunningham, Erin Haney, Kevin Cunningham, and Nathan Almirall, for helping me learn materials science and for making my graduate student experience truly unforgettable.

Many other UCSB researchers and technical staff have contributed to this work. I especially thank Dr. Deryck Stave for teaching me about electron beam deposition, and for allowing me to make custom modifications to the instrument. I also thank Dr. Gareth Seward, who taught me everything I know about electron backscatter diffraction, my favorite characterization technique. Dr. Stephan Kramer, Tobias Brown-Heft, Prof. Chris Palmstrom, Dr. Miguel Zepeda, Dr. Youli Li, and Andy Weinberg have also aided with various parts of the research and given me guidance throughout the years.

I thank Dr. Kurt Sickafus (University of Tennessee), who mentored me during my summer undergraduate internships at LANL, and who, along with Prof. Odette, initially designed the bilayer project. I am very thankful for the collaboration with Prof. Yong Jiang (CSU) for providing crucial insights into metal-oxide interfaces, and for sponsoring my visit to China. I thank the following external researchers for their various contributions which are listed individually at the end of each chapter: Dr. Yongquiang Wang (LANL), Dr. Blas Uberuaga (LANL), Dr. Haidong Zhou (UT), Dr. Frances Allen (UCB), Prof. Peter Hosemann (UCB), Dr. Lynne Ecker (BNL), Dr. David Sprouster (BNL), Dr. Xunxiang Hu (ORNL), Dr. Richard Cox (PNNL), Dr. Ingrid Burgeson (PNNL), and Dr. Rick Kurtz

(PNNL). I also thank the Department of Energy Office of Fusion Energy Sciences which funded this work almost entirely.

Finally, I am truly thankful for all of my experiences at UCSB. During the past nine years as an undergraduate and graduate student, I obtained two degrees, took courses in over thirty subjects, learned from over one hundred professors, discovered my love for materials science and engineering, organized University events, played in hundreds of soccer games, won ten intramural championships, and made countless life-long friendships. I will forever be a UCSB gaucho. Olé!

CURRICULUM VITAE

TIBERIU STAN

Ph.D. Materials Science and Engineering

Materials Department, Bldg. 503, Rm. 3109 Tel: +1 (505) 310 – 2060
University of California Santa Barbara, California, 93106 Email: tstan@engineering.ucsb.edu

EDUCATION

Ph.D. – Materials Science and Engineering **03/2017**
University of California Santa Barbara
Thesis: "Fabrication and Characterization of He Implanted Fe – $Y_2Ti_2O_7$ Bilayers: Model Interfaces for Advanced Understanding of Nanostructured Ferritic Alloys"
Committee: G. Robert Odette (advisor), Tresa Pollock, Carlos Levi, Michael Gordon

B.S. – Physics **06/2011**
University of California Santa Barbara
College of Creative Studies

EXPERIENCE & KNOWLEDGE

Characterization	Deposition & Beamlines	Sample Preparation	Software
• SEM, EBSD, EDX	• E-Beam Deposition	• Polishing	• SRIM/TRIM
• XRD, SAXS, XAS	• Magnetron Sputtering	• Ball Milling	• Mathematica
• AFM	• Atomic Layer Deposition	• Cleanroom experience	• CrystalMaker
• TEM/HRTEM/STEM	• Tandem Ion Beam (LANL)	• Glovebox experience	• Gwyddion
• SIMS	• XPD-II beamline (at BNL)	• Plasma Cleaning	• SolidWorks
• Dektak	• X23A2 beamline (at BNL)	• Focus Ion Beam	• Mendeley
• Optical Microscopy	• 11-ID-C beamline (at ANL)	• Spark Plasma Sintering	• Microsoft Office

MENTORSHIP

Mentor – UC LEADS Program **2013**
- Co-advised an undergraduate student through a summer research project to develop and characterize a novel Scandium-based nanostructured ferritic alloy.

Teaching Assistant – Materials 100C: Fundamentals of Structural Evolution **2011**
- Guest lectured and designed homework problem sets on thermodynamic and kinetic principles governing structural evolution in materials.

WORK EXPERIENCE

Graduate Researcher – University of California Santa Barbara **2011 – Present**

- Studied fundamental properties of Nanostructured Ferritic Alloys (NFAs) to further the development of thermally stable and radiation tolerant materials.
- First to report self-selected crystallographic orientation relationships of metal-oxide interfaces fabricated by controlled deposition of Fe onto $Y_2Ti_2O_7$ single crystals.
- Improved an electron beam deposition system by adding and calibrating a rotating stage, designing custom holders, and optimizing operating parameters.
- Developed an extraction and filtration method to isolate a specific nano-oxide population, then characterized the samples and NFAs using synchrotron light sources (Argonne, Brookhaven NL).

Undergraduate Researcher – Los Alamos National Laboratory **2009 – 2011**

- Synthesized Mg_2TiO_4 pellets by ball milling, pressing, and sintering.
- Irradiated samples using Danfysik High Energy Ion Implanter at the LANL IBML and characterized the microstructure using XRD, SEM, and EBSD.
- Discovered that Mg_2TiO_4 is surprisingly radiation tolerant due to an induced phase transformation from inverse spinel to rocksalt.

Software Tester – Los Alamos National Laboratory **2006 – 2008**

- Helped develop the LANL Waste Compliance and Tracking System, a task-based software that tracks the lifetime of nuclear waste from generation to disposal.
- Wrote and executed test cases which serve as official documents.
- Updated system requirement files and created work flow diagrams.

Vice President – UCSB – Student Apartment Community Council **2008 – 2010**

- Organized competitions, conducted weekly meetings, and initiated charity events.
- Interviewed and recruited students to the council.
- Rewarded outstanding student behavior to maintain a productive environment.

AWARDS AND ACCOMPLISHMENTS

- International collaboration between UCSB and CSU – Central South University, China **2016**
- UCSB Doctoral Student Travel Grant – ICFRM-17 conference, Aachen Germany **2015**
- Best Presentation Award – TMS 2015 conference/MPIM, Orlando FL **2015**
- Best Poster Finalist – MRS 2013 conference, Anaheim CA **2013**
- Completion of Neutron Scattering in Nuclear Materials School – UC Berkeley **2012**
- Best Poster Award – Student Symposium, LANL **2011**
- Completion of Atomic Level Response of Materials to Irradiation School – Santa Fe NM **2010**
- Science Undergraduate Laboratory Internship – LANL **2010**
- Voice of the People award – Student Apartment Community Council, UCSB **2009**
- SPOT award for Student Symposium presentation – LANL **2007**

PUBLICATIONS

1. **T. Stan,** Y. Wu, G.R. Odette, T. Brown-Heft, C. Palmstrom, "Fabrication, Characterization and Helium Implantation of Fe-{110}$Y_2Ti_2O_7$ Bilayers", Acta Materialia, *Manuscript in Progress* (2017)
2. **T. Stan,** Y. Wu, G.R. Odette, H.D. Zhou, "Epitaxial Fe thin films on {100} $Y_2Ti_2O_7$: model interfaces for nano-oxide dispersion strengthened steels", Metallurgical and Materials Transactions A, *submitted* (2017)
3. **T. Stan,** D.J. Sprouster, G.R. Odette, L.E. Ecker, I. Charit, "X-ray absorption spectroscopy characterization of embedded and extracted nano-oxides", Journal of Alloys and Compounds, *Accepted* (2017). doi: 10.1016/j.jallcom.2016.12.350
4. D.J. Sprouster, J. Sinsheimer, E. Dooryhee, S.K. Ghose, P. Wells, **T. Stan**, N. Almirall, G.R. Odette, L.E. Ecker, "Structural characterization of nanoscale intermetallic precipitates in highly neutron irradiated reactor pressure vessel steels", Scripta Materialia, Vol. 113 (2016) pp. 18–22. doi: 10.1016/j.scriptamat.2015.10.019
5. **T. Stan**, Y. Wu, G.R. Odette, K.E. Sickafus, H.A. Dabkowska, B.D. Gaulin, "Fabrication and characterization of naturally selected epitaxial Fe – {111}$Y_2Ti_2O_7$ mesoscopic interfaces: some potential implications to nano-oxide dispersion strengthened steels", Metallurgical and Materials Transactions A, 44 (2013) 10, pp. 4505–4512. doi: 10.1007/s11661-013-1827-3

ORAL PRESENTATIONS AND POSTERS

1. **T. Stan,** Y. Wu, G.R. Odette, T. Yamamoto, J. Ciston, Y. Wang, R. Cox, "He Interactions With Embedded Nano-Oxides and Metal-Oxide Bilayers", TMS 2017, San Diego, CA (2017)
2. **T. Stan,** Y. Wu, G.R Odette, T. Brown, C. Palmstrom, F. Allen, P. Hosemann, "Investigation of He Implanted Fe – $Y_2Ti_2O_7$ Bilayers: Surrogate Interfaces to Further NFA Understanding", TMS 2016, Nashville, TN (2016)
3. **T. Stan,** D.J. Sprouster, A. Ofan, G.R. Odette, L. Ecker, "Bulk Extraction and XAS Characterization of Oxide Features in Nanostructured Ferritic Alloy MA957", TMS 2016, Nashville, TN (2016)
4. **T. Stan,** Y. Wu, G.R. Odette, "Fabrication and Characterization of Naturally Selected Fe – $Y_2Ti_2O_7$ Interfaces", UCSB Structural Seminar, Santa Barbara, CA (2016)
5. **T. Stan,** Y. Wu, S. Kraemer, G.R. Odette, "Investigation of Fe – {100} $Y_2Ti_2O_7$ Bilayers: Surrogate Interfaces to Further Nanostructured Ferritic Alloy Understanding", ICFRM-17, Aachen, Germany (2015)
6. **T. Stan,** Y. Wu, S. Kraemer, G.R. Odette, "Fabrication and Characterization of Naturally Selected Fe – $Y_2Ti_2O_7$ Interfaces", TMS 2015, Orlando, FL (2015) **Best Talk Award**
7. **T. Stan,** Y. Wu, S. Kraemer, G.R. Odette, "Fabrication and Characterization of Naturally Selected Fe – $Y_2Ti_2O_7$ Interfaces", UCSB Structural Seminar, Santa Barbara, CA (2015)
8. **T. Stan,** S. Kraemer, Y. Wu, G.R. Odette, "Fabrication and Characterization of Fe – {110} $Y_2Ti_2O_7$ Mesoscopic Interfaces", ANS 2014 - TOFE, Anaheim, CA (2014)
9. **T. Stan,** Y. Wu, G.R. Odette, "Creation and Characterization of Meso-scale Fe – $Y_2Ti_2O_7$ Interfaces", TMS 2014, San Diego, CA (2014)

10. **T. Stan,** Y. Wu, G.R. Odette, "Fabrication and Characterization of Naturally Selected Fe – $Y_2Ti_2O_7$ Interfaces", UCSB Structural Seminar, Santa Barbara, CA (2014)
11. **T. Stan,** Y. Wu, G.R. Odette, K. Sickafus, "Fabrication and Characterization of Naturally Selected Fe – {111} $Y_2Ti_2O_7$ Mesoscopic Interfaces: Potential Implications to Nano-oxide Dispersion Strengthened Steels", TMS 2013, San Antonio, TX (2013)
12. **T. Stan,** Y. Wu, G.R. Odette, "Fabrication and Characterization of Naturally Selected Fe – {111} $Y_2Ti_2O_7$ Interfaces", UCSB Structural Seminar, Santa Barbara, CA (2013)
13. **T. Stan,** Y. Wu, G.R. Odette, K. Sickafus, "Fabrication and Characterization of Oriented Fe – $Y_2Ti_2O_7$ Interfaces: Implications to the Development and Optimization of ODS Alloys", MRS 2012, San Francisco, CA (2012) **Best Poster Finalist**
14. **T. Stan,** Y. Wu, G.R. Odette, "Fabrication and Characterization of Naturally Selected Fe – {111} $Y_2Ti_2O_7$ Interfaces", UCSB Structural Seminar, Santa Barbara, CA (2012)
15. **T. Stan,** Y. Wu, G.R. Odette, K. Sickafus, "Fabrication and Characterization of Oriented Fe – $Y_2Ti_2O_7$ Interfaces: Implications to the Development and Optimization of Oxide Dispersion Strengthened Alloys", TMS 2012, Orlando, FL (2012)
16. **T. Stan,** M. Patel, J. Valdez, Y. Wang, K. Sickafus, "Light Ion Irradiation Effects on the Crystal Structure of Mg_2TiO_4", Student Symposium, LANL (2011) **Best Poster Award**
17. **T. Stan,** J. Valdez, M. Patel, K. Sickafus, "Light Ion Irradiation Effects on the Crystal Structure of Mg_2TiO_4", Student Symposium, LANL (2010)

EXTRACURRICULAR ACTIVITIES

Acting – "Breaking Bad" TV series, "Sarah Connor Chronicles" TV series, "Silent Heart" short, "Awkward Courage" short, "How to Charge Time" training videos for LANL.

Sports – Captain of multiple intramural soccer teams at UCSB, "Sundowners" ultimate frisbee club, former captain of the Los Alamos Rugby Team.

ABSTRACT

Despite the successful development of Tokamak nuclear fusion plasma physics devices, commercial power production remains elusive partly due to the severe environments produced during the deuterium-tritium fusion reaction. Nanostructured Ferritic Alloys (NFAs) are candidate structural materials for first-wall/blanket applications. The stainless steels are thermally stable up to 900 °C and remarkably irradiation tolerant. NFAs typically contain a high number density ($5x10^{23}/m^2$) of Y-Ti-O nano-oxides (NOs) with average diameters <d> ≈ 2.5 nm. Most of the smallest NOs are $Y_2Ti_2O_7$ (YTO) fcc pyrochlore. The NOs impede dislocation climb and glide, stabilize dislocation and grain structures, and trap He in fine-scale bubbles at matrix-NO interfaces. Detailed characterization and analysis of the NO-matrix interfaces is needed to develop first principles and atomic-scale models that are part of multi-scale efforts to predict the behavior of NFAs during processing and in irradiation service environments. YTO-matrix orientation relationships (ORs) are of particular interest because they impact selection of compositions and processing paths, service stability, mechanical properties and irradiation tolerance of NFAs.

X-ray absorption spectroscopy (XAS) measurements on embedded NOs are most consistent with $Y_2Ti_2O_7$, while the slightly larger extracted oxides are primarily consistent with Y_2TiO_5. A bulk extraction and selective filtration technique was developed to dissolve the ferritic matrix, trap the larger Y_2TiO_5 oxides, and yield samples well suited for XAS measurements. Further, a 14YWT alloy was annealed to coarsen the NOs, and He implanted to produce bubbles. High resolution transmission electron microscopy shows

two dominant ORs (cube-on-edge and cube-on-cube). The smaller NOs are associated with smaller bubbles, while some of the largest NOs (>6 nm) often have two bubbles. Most bubbles nucleate near dislocation cores at {111} NO facets.

The second research approach is to study a model bilayer system. For the first time, the dominant deposited Fe-YTO interface ORs are reported. Most Fe grains deposited on {111}YTO have the Nishiyama-Wasserman OR: {110}Fe//{111}YTO and <100>Fe//<110>YTO. The dominant OR for depositions on {100}YTO is: {110}Fe\\{100}YTO and <111>Fe\\<110>YTO. Finally, most Fe grains deposited on {110}YTO show axiotaxial texturing with off-normal {110}Fe planes parallel to off-normal {100}YTO planes. Room temperature He implantation of a Fe-{110}YTO bilayer shows a range of bubble sizes in the Fe film, and larger ~2 nm bubbles at the Fe-YTO interface. In this experiment, He did not diffuse into the YTO. In a second, high temperature implantation, 99.3% of the He remained in the Fe film and interfacial pores, but 0.7% was found in the YTO substrate. The studies performed in this dissertation provide crucial experimental inputs for the development of computational models that accurately predict NFA in-service behavior. The results provide an important step into turning the promise of fusion energy into a reality.

TABLE OF CONTENTS

LIST OF FIGURES

LIST OF TABLES

ABBREVIATIONS

APT	atom probe tomography
<d>	average diameter
dpa	displacements per atom
DuET	Dual Beam for Energy Science and Technology Facility
EDX	energy dispersive x-ray
EBSD	electron backscatter diffraction
EXAFS	extended x-ray absorption fine structure
FIB	focused ion beam
IPFZ	inverse pole figure z-direction
<N>	average number density
NFA	nanostructured ferritic alloy
NO	nano-oxide
ODS	oxide-dispersion strengthened
OR	orientation relationship
PF	pole figure
SEM	scanning electron microscopy
SIA	self-interstitial atom
SRIM	stopping and range of ions in matter
STEM	scanning transmission electron microscopy
TEM	transmission electron microscopy
TDS	thermal desorption spectroscopy
XAS	x-ray absorption spectroscopy
XANES	x-ray absorption near-edge structure
XRD	x-ray diffraction
YTO	$Y_2Ti_2O_7$
γ	interface energy

Chapter 1 Introduction

1.1 Overview

The worldwide demand for large-scale energy will increase under the combined pressure of population growth, increased urbanization and expanding access to electricity in developing countries. Nuclear fusion is one of the most promising options for generating very large amounts of energy. Future power stations will be: sustainable – fusion fuels are widely available, clean – there are no CO_2 emissions, and safe – no risk of unstable chain reactions.

Despite the successful development of Tokamak fusion plasma physics devices, commercial power production remains elusive partly due to the severe environments produced during the deuterium-tritium fusion reaction. The identification of first-wall and blanket structures capable of withstanding high heat fluxes and intense radiation environments is central to meeting the immense material challenges. Economical fusion power will require structural materials to operate at temperatures up to 800 ºC, to handle damage levels of 50-200 dpa, and to mitigate the deleterious effects of 100-2000 appm transmuted helium (He) over an estimated multi-year operation lifetime [1–3].

Nanostructured Ferritic Alloys (NFAs) are candidate structural materials for first-wall/blanket applications. The Fe-Cr-based stainless steels are thermally stable up to 900

°C and remarkably irradiation tolerant [2,4–6]. NFAs typically contain a high number density (5 x $10^{23}/m^2$) of Y-Ti-O nano-oxides (NOs) with average diameters <d> ≈ 2.5 nm [2,4]. The NOs impede dislocation climb and glide, stabilize dislocation and grain structures, and trap He in fine-scale bubbles at matrix-NO interfaces [1,4,6]. The high density of small bubbles prevents the formation of growing voids, and decreases He accumulation at grain boundaries which otherwise degrade the dimensional stability, creep, and fracture properties of most structural alloys. The NOs, and especially the He bubbles, also act as recombination sites for vacancies and self-interstitial defects, thereby promoting radiation damage self-healing.

Research to characterize NO compositions, misfit strains, core shell structures, interface characteristics, and NO-matrix orientation relationships (ORs) is ongoing [7–11]. Most of the smallest NOs are $Y_2Ti_2O_7$ (YTO) fcc pyrochlore [9–18]. The cuboidal NOs have multiple interfacial ORs, usually with low index {100}, {110}, and {111} YTO planes bonded to the surrounding matrix. Detailed characterization and analysis of the NO-matrix interfaces is needed to develop first principles and atomic-scale models that are part of multi-scale efforts to predict the behavior of NFAs during processing and in irradiation service environments. YTO-matrix ORs are of particular interest because they impact selection of compositions and processing paths, service stability, mechanical properties and irradiation tolerance of NFAs. Interface characteristics of interest include structures, local chemistries, defects, misfit strains, energies and NO interactions with He.

1.2 Outstanding Questions and Research Approach

One of the materials challenges addressed in this dissertation is related to the fate of the irradiation produced defects and transmutation produced He. Some of the outstanding questions regarding the interactions of defects and He with NFAs are graphically shown in Figure 1.1. Questions that this dissertation will address include: What are the NO chemistries and structures? Are there compositional differences between small and large NOs? What are the bulk and interfacial ORs between embedded NOs and the ferrite matrix? What are the preferred bubble nucleation sites at the NO-matrix interfaces? Is there a relationship between NO size and bubble size? Do multiple bubbles nucleate on NOs? At low implantation rates, if He atoms first enter the YTO NO structure prior to forming interface bubbles (as indicated from first-principles modeling [19,20]) what is the partitioning of He between YTO, the ferritic matrix, and the associated interface?

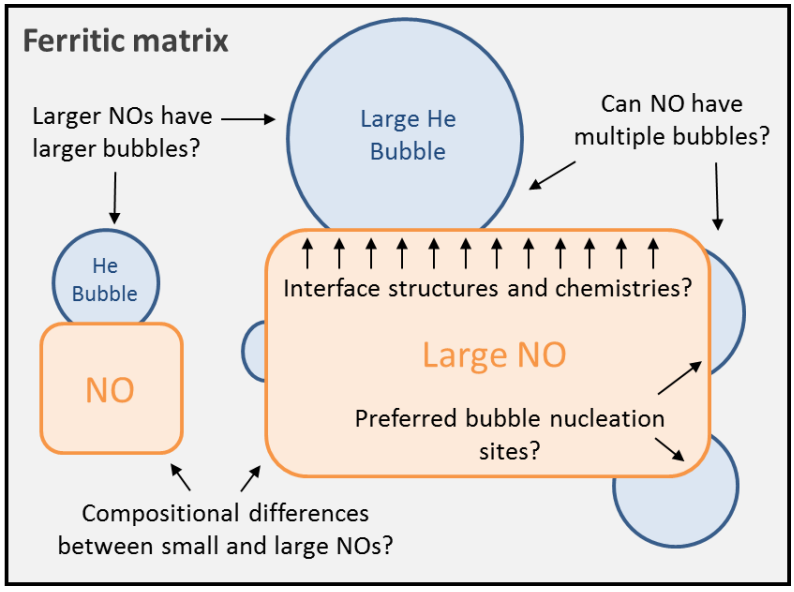

Figure 1.1 – Summary of questions regarding NOs and associated He bubbles.

In this dissertation, two approaches were used to gain insight into the previous questions. The first approach is to conduct studies on the alloys themselves. To characterize the chemical environments and structures present in NFAs, X-ray Absorption Spectroscopy (XAS) measurements were performed on embedded and extracted NOs (Chapter 3). As previously mentioned, the interactions between He and NOs are difficult to observe partly due to their small sizes (nm scale). Thus, an NFA was first annealed to coarsen the NOs and then He implanted to nucleate bubbles. Questions about the preferred bubble nucleation sites, relationships between NO size and bubble size, and the presence of multiple bubbles on NOs are addressed in Chapter 4.

The second research approach is to study a model bilayer system which has greater control over the Fe-YTO interfacial parameters. As previously mentioned, the faceted NOs usually have low index {100}, {110}, and {111} YTO planes bonded to the surrounding

matrix. Thus, Fe was deposited on bulk single crystals of YTO to create mesoscopic-scale interfaces that in principle are easier to study than those found in embedded NOs. Characterizations of Fe-{111}YTO, Fe-{100}YTO, and Fe-{110}YTO bilayers are reported in Chapters 5, 6, and 7, respectively. The larger interfaces found in the Fe-YTO bilayers are ideal for gaining insight into the partitioning of He between Fe and YTO. The results from low temperature and high temperature He implantation studies of bilayers are reported in Chapters 8 and 9, respectively.

A summary of the studies performed in this dissertation, the insight gained from the collective observations, and suggested future work is found in Chapter 10. The characterizations and observations performed on NFAs provide insights for the development and optimization of NFAs. By reporting, for the first time, the structures and chemistries of Fe depositions on YTO substrates, we advance the complex and ever-evolving field of metal-oxide interfaces. The studies performed in this dissertation provide crucial experimental inputs for the development of computational models that accurately predict NFA in-service behavior. The results provide an important step into turning the promise of fusion energy into a reality.

1.3 References

[1] G.R. Odette, D.T. Hoelzer, JOM 62 (2010) 84–92.

[2] G.R. Odette, M.J. Alinger, B.D. Wirth, Annu. Rev. Mater. Res. 38 (2008) 471–503.

[3] S.J. Zinkle, J.T. Busby, Mater. Today 12 (2009) 12–19.

[4] G.R. Odette, JOM 66 (2014) 2427.

[5] N. Cunningham, Y. Wu, D. Klingensmith, G.R. Odette, Mater. Sci. Eng. A 613 (2014) 296–305.

[6] Y. Dai, G.R. Odette, T. Yamamoto, The Effects of Helium in Irradiated Structural Alloys, 1st ed., Elsevier Inc., 2012.

[7] E.A. Marquis, Appl. Phys. Lett. 93 (2008) 10–13.

[8] S. Liu, G.R. Odette, C.U. Segre, J. Nucl. Mater. 445 (2014) 50–56.

[9] V. Badjeck, M.G. Walls, L. Chaffron, J. Malaplate, K. March, J. Nucl. Mater. 456 (2015) 292–301.

[10] Y. Wu, J. Ciston, S. Kräemer, N. Bailey, G.R. Odette, P. Hosemann, Acta Mater. 111 (2016) 108–115.

[11] Y. Miao, K. Mo, B. Cui, W. Chen, M.K. Miller, K.A. Powers, V. Mccreary, D. Gross, J. Almer, I.M. Robertson, J.F. Stubbins, Mater. Charact. 101 (2015) 136–143.

[12] J. Ribis, Y. De Carlan, Acta Mater. 60 (2012) 238–252.

[13] J. Ribis, S. Lozano-Perez, J. Nucl. Mater. 444 (2014) 314–322.

[14] K. Dawson, G.J. Tatlock, J. Nucl. Mater. 444 (2014) 252–260.

[15] M. Tamura, H. Sakasegawa, K. Shiba, H. Tanigawa, K. Shinozuka, H. Esaka, Metall. Mater. Trans. A 42 (2011) 2176–2188.

[16] Y. Wu, E.M. Haney, N.J. Cunningham, G.R. Odette, Acta Mater. 60 (2012) 3456–3468.

[17] A.J. London, B.K. Panigrahi, C.C. Tang, C. Murray, C.R.M. Grovenor, Scr. Mater. 110 (2016) 24–27.

[18] R. Kasada, N. Toda, K. Yutani, H.S. Cho, H. Kishimoto, A. Kimura, J. Nucl. Mater. 367–370 A (2007) 222–228.

[19] L. Yang, Y. Jiang, Y. Wu, G.R. Odette, Z. Zhou, Z. Lu, Acta Mater. 103 (2016) 474–482.

[20] L. Yang, Y. Jiang, G. Robert Odette, T. Yamamoto, Z. Liu, Y. Liu, J. Appl. Phys. 115 (2014) 143508.

Chapter 2 Background

2.1 Introduction

One of the challenges for the future of mankind is meeting the rapidly increasing demand for energy. The total world electricity consumption is projected to reach 239,000 TWh by 2040, a 48% increase from 2012 [1]. In 2013, the energy portfolio by power source was composed of: oil 31%, coal 29%, natural gas 23%, biofuels and waste 10%, nuclear 5%, and other (solar, wind, geothermal, etc.) 2% [2]. This distribution will change and continuously evolve as new technological advancements and socio-political movements arise. Concerns about pollution from fossil fuels such as oil, coal, and natural gas have led to an increase in international agreements to explore new energy avenues.

Nuclear fusion is one of the most promising options for generating very large amounts of energy, and can provide a safe, clean energy source for future generations [3–6]. Advantages include: (1) An abundant fuel supply – deuterium is easily extracted from seawater, and tritium can be produced in the fusion reactor itself through lithium which is found in the earth's crust. Fuel supplies will be available for millions of years. (2) Energy efficiency – one kilogram of fusion fuel can provide the same amount of energy as 10 million kilograms of fossil fuel. (3) Safety – the amounts of fuel used in fusion devices at any time are small, thus uncontrolled releases of energy will not occur. (4) Clean – nuclear

fusion is a carbon-free energy source, and the reaction by-product helium does not add to atmospheric pollution.

2.1.1 Nuclear Fusion Basics

Sir Arthur Eddington (1882-1944), a prominent astrophysicist, first postulated that the sun's energy came from the fusion of hydrogen atoms into helium [7]. To fuse atoms, their nuclei must be brought close enough together (a distance of ~10^{-15} m) such that the attractive nuclear strong force exceeds the repulsive electrostatic force, thus binding them into a heavier nucleus [5]. A significant amount of kinetic energy is needed to overcome the electrostatic Coulombic barrier before the fusion reaction can take place. For nuclei lighter than Fe^{56}, the fusion reaction is exothermic, thus releasing heat.

The sun's massive size, immense gravitational forces, and high temperatures provide the kinetic energy and conditions necessary for nuclear fusion to occur. Once an atom is heated above its ionization energy, the negatively charged electrons become unbound from the positively charged nucleus. The result is a hot cloud of ions, also known as a plasma. Because the charges are separated, plasmas are electrically conductive and magnetically controllable.

Many fusion devices are designed to take advantage of the plasma properties and control the particles as they are being heated. The Tokamak reactor, a Russian acronym for "toroidal chamber with axial magnetic field", is the most well-developed and well-funded approach to fusion energy [8]. The devices use magnetic and electric fields to heat and

squeeze the hydrogen plasma. Computer simulations indicate that the most efficient shape for the magnetically confined plasma is a donut shape (toroid). For example, the International Thermonuclear Experimental Reactor (ITER) in France will have a plasma toroid with a 2 m inner radius and a 6.2 m outer radius, and will be the largest Tokamak in the world [9,10]. ITER will be a self-contained reactor with parts that can be easily inserted and removed without having to tear down the entire structure for maintenance. The ITER project aims to bridge the gap between experimental studies of plasma physics and electricity-producing fusion power stations.

Generally, Tokamak reactors use high temperatures and large magnetic fields to fuse deuterium and tritium [6,8,11]. Deuterium (^2_1D) is the 1-neutron, 1-proton isotope of hydrogen which occurs naturally and is commonly extracted from seawater. Tritium (^3_1T) is the 2-neutron isotope of hydrogen, but because of its short half-life of 12.32 years, it is difficult to obtain and store. In a fusion device, deuterium and tritium atoms are fused into helium and a 14.1 MeV "fast" neutron:

$$^2_1D + {}^3_1T \rightarrow {}^4_2He(3.5\ MeV) + {}^1_0n(14.1\ MeV)$$

Figure 2.1 is a 3D rendering of a Tokamak reactor indicating many of the material components [8]. Lithium blanket structures outside of the plasma reaction chamber will absorb some of the high-energy neutrons, and the resulting reaction yields more tritium fuel, which is captured and used as fuel for the fusion reactor [12]. Depending on the future reactor design, liquids or alloys containing ^{6}Li and ^{7}Li will be used to produce more tritium though the two reactions shown below:

$$^{6}_{3}Li + \ ^{1}_{0}n \ \rightarrow \ ^{4}_{2}He + \ ^{3}_{1}T$$

$$^{7}_{3}Li + \ ^{1}_{0}n \ \rightarrow \ ^{4}_{2}He + \ ^{3}_{1}T + \ ^{1}_{0}n$$

The first wall, blanket, and divertor structures are primarily heated by radiation from the plasma, but also by deuterium, tritium, and neutrons. This heat is transferred by a water-cooling loop to a heat exchanger to make steam which drives electrical turbines to produce electricity. The power needed to start the fusion reaction is about 50 MW, but the power yielded is about 500 MW, nearly 10 times greater. Mass for mass, the fusion of deuterium and tritium releases roughly three times as much energy as U^{235} fission, and millions of times more energy than a chemical reaction such as the burning of coal.

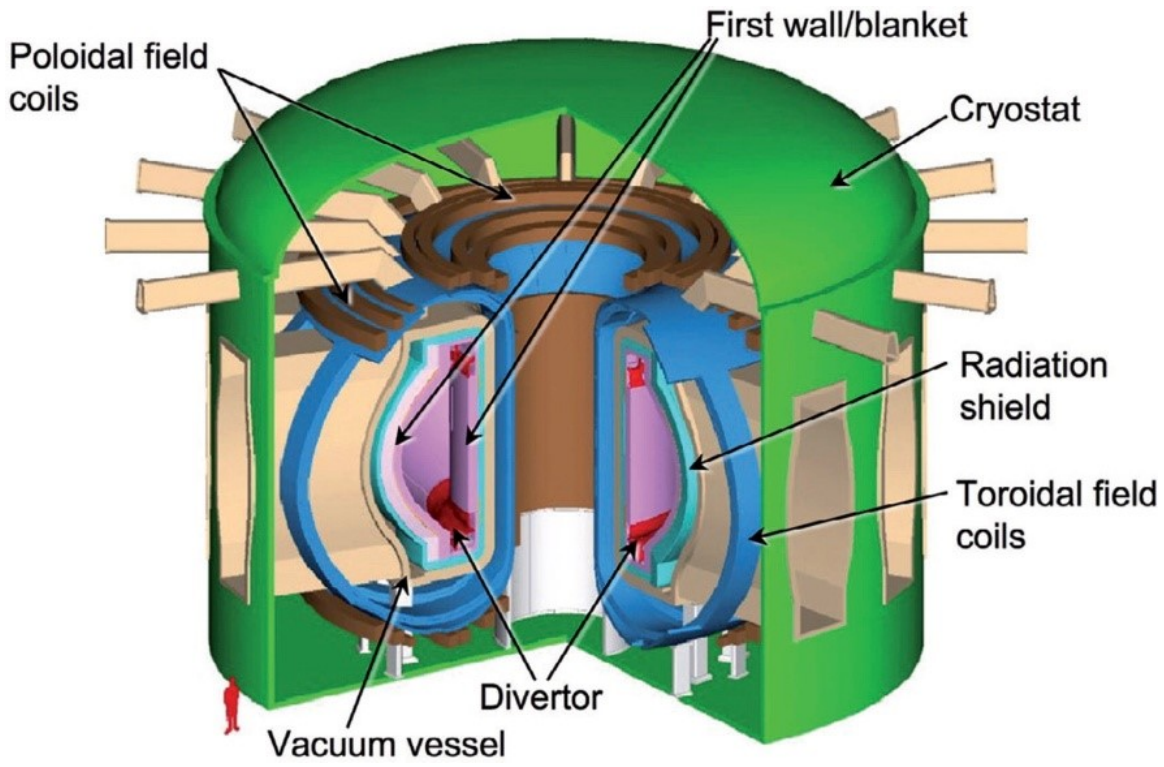

Figure 2.1 – 3D rendering of a Tokamak reactor. For scale, a human is shown in red at the bottom left of the image. Image reproduced from reference [8].

2.1.2 Materials Challenges

The future success of proposed fusion energy reactors lies heavily on the development of high-performance structural materials that must be radiation resistant, self-healing, thermally stable, structurally compatible, accident tolerant, and inexpensive. Reactor materials will be subject to unprecedented fluxes of high-energy neutrons, intense thermochemical stresses, and high temperature coolants that may induce corrosion [3,6,11,13]. Steady-state heat fluxes for first wall and divertor components are projected to

be in the range of 1 to 10 MW/m^2, which is substantially higher than the highest heat flux for structural materials in fission reactors (~1 MW/m^2 for the fuel cladding) [5]. Further, the fusion by-product 3.5 MeV helium, together with other low energy neutral and charged particles, can induce sputtering, erosion, and blistering in the plasma facing materials [14]. The materials effects are complex, synergistic, not fully understood, and cannot possibly be covered completely in this thesis. Researchers throughout the world are developing high-performance reactor materials to make fusion power a reality.

One of the materials challenges addressed in this thesis is related to the effect of 14.1 MeV neutrons on first wall structures, and specifically, the fate of the irradiation produced defects and transmutation produced helium (He). About 90% of the neutron's energy is transferred to the lithium-containing blanket structures, but 10% will be deposited in the first wall [14]. Neutrons that impact first wall structures have sufficient kinetic energy to displace a substantial number of atoms from their lattice sites over the projected reactor lifetime. The two resulting material defects are: self-interstitial atoms (SIAs) – dislodged atoms that now share lattice sites, and vacancies – the now-empty lattice sites. These two defects are produced together in equal amounts and referred to as Frenkel Pairs. The amount of radiation damage is quantified as displacements per atom (dpa) [15,16]. For example, a damage level of 200 dpa indicates that, on average, each atom was displaced two hundred times from its lattice site.

The 14.1 MeV neutrons transfer energy to the lattice through scattering and nuclear reactions to displace atoms from their normal sites [4,5,14]. The high energy recoil atoms

cause secondary recoils which then further displace other atoms from their sites. This process is referred to as a damage cascade. About 30% of the initially displaced atoms survive inter-cascade recombination. These residual defects undergo long-range diffusion through the lattice and almost all either recombine or annihilate at sinks which include: gas bubbles ($_b$), voids ($_v$), and dislocations ($_d$). The corresponding sink strengths (Z) are: $Z_b \approx 4\pi r_b N_b$ for bubbles, $Z_v \approx 4\pi r_v N_v$ for both vacancies and SIAs; $Z_{dv} \approx \rho$ for vacancies at dislocations, and $Z_{di} \approx \rho\ [1+B]$ for SIAs at dislocations. Here, r and N are the size and number densities of bubbles and voids, ρ is the dislocation density, and B is a bias factor due to the long-range strain fields of dislocations which preferentially attract SIAs. The bias also causes dislocation loops to nucleate and grow, and the preferential accumulation of SIAs at network dislocation segments cause climb. Loop growth and climb can lead to dislocation formation (through loops and Herring–Nabarro sources) and annihilation (through joining of oppositely signed network segments), ultimately leading to quasi-steady-state densities. Further, the excess vacancies diffuse to other neutral or less biased sinks and lead to cavity formation, growing voids, embrittlement, and degradation of material properties. Ultimate survival of only 0.1% of the dpa in the form of clustered vacancies can lead to 10% swelling at 100 dpa [14]. Understanding the effects of radiation damage on microstructures is critical to the development of fusion reactor materials.

2.1.3 Helium Effects

In addition to producing radiation damage, the 14.1 MeV neutrons lead to the formation of He within Fe-based alloys [4,17]. The neutron energy is far above the threshold for neutron to alpha (~5 MeV) and neutron to proton (~1 MeV) transmutation reactions in Fe [14]. The alpha particles (which become He with the addition of two electrons) are produced in amounts ranging from less than one to thousands of atomic parts per million (appm), depending on the neutron spectrum, fluence, and alloy composition. First wall fusion reactor materials are expected to reach a damage level of ~200 dpa and helium concentrations of ~2000 appm at the end of life (~10 years) [4,17].

The most important characteristic of He, which makes it significant to many irradiation damage phenomena, is that it is a noble gas and essentially insoluble in solids. In the temperature range where He is mobile, it diffuses through the matrix and precipitates to initially form bubbles, usually at microstructural trapping sites. The bubbles can serve as nucleation sites of growing voids in the matrix, and as creep cavities on grain boundaries, caused by radiation damage and mechanical stress, respectively. Small He pressurized bubbles absorb and emit vacancies in net numbers that exactly equal the number of SIAs that they absorb, and are thus stable in the matrix. Bubbles only grow by the addition of diffusing He atoms. However, when bubbles reach a critical size, they convert to unstably growing voids due to the previously-mentioned supersaturation of vacancies (SIAs are preferentially biased to dislocations) [14]. Voids grow through vacancy capture, and can

lead to swelling which degrades properties and leads to swelling-induced dimensional instabilities that are unacceptable for large-scale engineering structures.

At high temperatures, He degrades material properties primarily by enhancing grain boundary cavitation, in some cases severely. Further, the He generation rate can also affect precipitate, dislocation loop, and network dislocation evolutions. While He effects are primarily associated with cavities, all microstructural processes during irradiation are intrinsically coupled. The synergistic effects of He, displacement damage, temperature, stress, and their interactions depend on the combination of all the irradiation variables, as well as details of the alloy type, composition, and starting microstructure (material variables). The implications to the wide range of properties of concern are not well understood, and require further investigation.

2.1.4 Critical Bubble Model

The Critical Bubble Model (CBM) addresses the transition of stable He bubbles to unstably growing voids under irradiation-driven displacement damage. The CBM concept has provided insight into the effects of He on swelling [14,17] and provides a basis for developing microstructures that can manage He and thus mitigate its deleterious effects.

Generally, cavities (a term used to define both bubbles and voids) can contain an arbitrary number of vacancies and He atoms. Bubbles shrink or grow only by the addition of He, while the larger voids grow unstably by the continuous accumulation of vacancies. By definition, the bubble ($_b$) growth rate dr_b/dt equals 0, while the growth rate can be

positive or negative for cavities that are slightly smaller and larger than the bubble radius (r_b), respectively. In the case of voids, the growth rate is positive at all r_v greater than a critical radius (r_v*) [14]. In general, the growth rate of a cavity ($_c$) containing a number of He atoms (m) is:

$$\frac{dr_c}{dt} = \frac{D_v X_v - D_i X_i - D_{sd} \exp\{\left(\frac{2\gamma_{MC}}{r_c} - \frac{3\kappa mkT}{4\pi r_c^3}\right)\frac{\Omega_v}{kT}\}}{r_c}$$

Here, r_c is the cavity radius, t is time, D_v and D_i are diffusion coefficients of vacancies and interstitials respectively, X_v and X_i are concentrations of vacancies and interstitials respectively, D_{sd} is the self-diffusion coefficient of the matrix atoms, γ_{MC} is the matrix-cavity interfacial energy, T is temperature, k is the Boltzmann constant, and Ω_v is the vacancy volume. κ is the non-dimensional compressibility factor used for modifying the ideal gas law to account for the real gas behavior. A graphical representation of this equation is shown with a blue curve in Figure 2.2.

In the equation, the D_vX_v term describes the flow of vacancies into the cavity which causes it to grow, while the second term (D_iX_i) corresponds to the flow of interstitials toward the cavity and causes it to shrink. Dislocation-SIA interactions due to long-range strain fields lead to a preferential flow of SIAs to dislocations, which leaves behind a supersaturation of vacancies $\Lambda = (D_vX_v – D_iX_i)/D_{sd}$.

The third term in the equation represents the outward flux of vacancies through the cavity surface. The concentration of vacancies in the cavity in equilibrium with the matrix across the curved cavity interface (X_v) is greater than the equilibrium concentration of

vacancies (X_{ve}) by: $X_v = X_{ve} \exp(2\gamma_{MC}\Omega_v/kTr)$ [14]. Thus, there is a driving force for vacancies to leave the cavity and flow down the concentration gradient and into the matrix. A large matrix-cavity interface energy γ_{MC} is beneficial to material performance since it increases the value of X_v, increases the vacancy emission rate, and decreases the cavity growth rate. The outward flux of vacancies can be viewed as matrix atoms which move toward the cavity with a self-diffusion coefficient of $D_{sd} = D_v X_{ve}$.

The exponent multiplying D_{sd} contains an outward He pressure term ($3ZmkT/4\pi r_c^3$) and an inward interfacial pressure term ($2\gamma_{MC}/r_c$). The first term is due to helium atoms inside the cavity which provide an outward pressure on the cavity surface. The interfacial term is due to the Gibbs-Thomson effect; the curved matrix-cavity interface is an energy penalty and provides an inward pressure toward the cavity center. A large interfacial energy γ_{MC} is beneficial for material performance as it increases the inward pressure thus decreasing the cavity growth rate.

The third order growth rate equation has two real roots where $dr_c/dt = 0$, and is shown in blue in Figure 2.2. The smaller root is the stable bubble radius r_b (green star in Figure 2.2) and the larger root is the unstable void radius r_v^* (red star). When $r_c < r_b$, the growth rate is positive and the cavity will grow by vacancy capture until $r_c = r_b$. Growth toward a stable bubble is shown with green arrows in Figure 2.2. When $r_b < r_c < r_v^*$ the growth rate is negative and the cavity will shrink until $r_c = r_b$. When $r_c > r_v^*$, the growth rate is positive and the cavities grow unstably as voids. This boundless growth is shown

with red arrows in Figure 2.2. Growing voids degrade material properties, thus it is important to design materials which keep $r_c < r_v^*$.

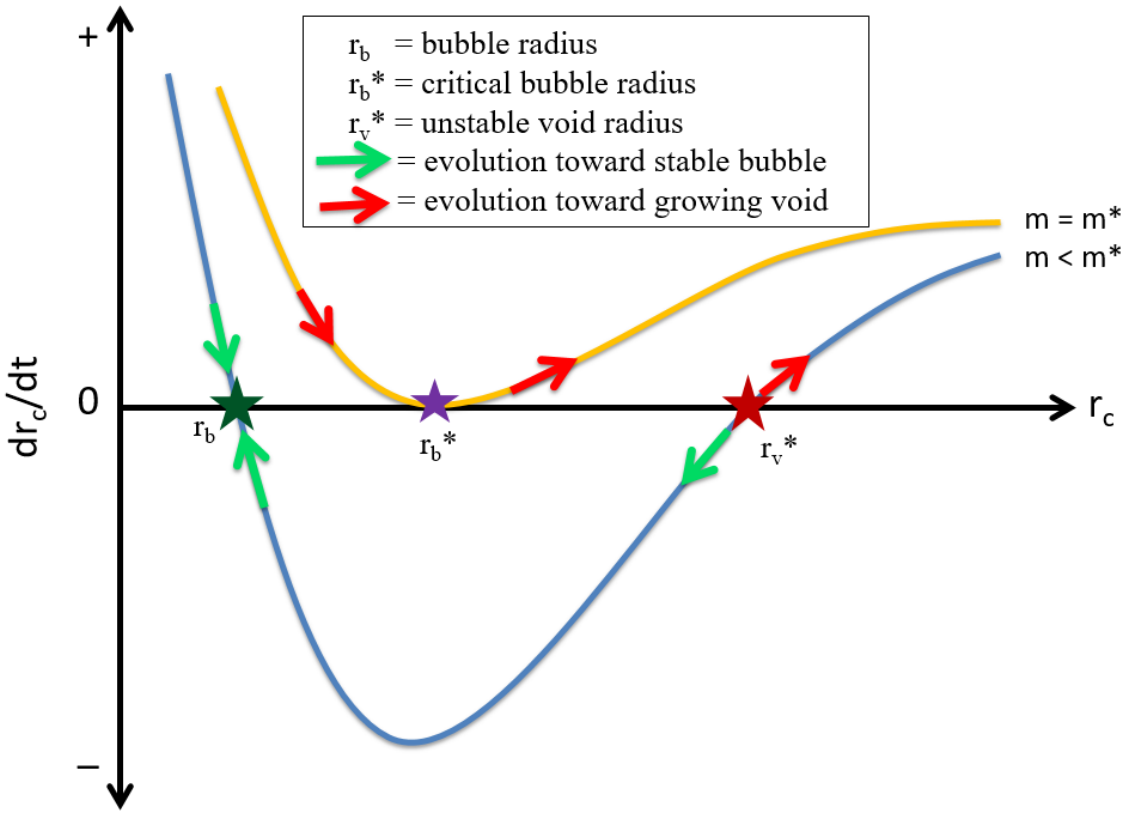

Figure 2.2 – Plot of cavity growth rate (dr_c/dt) versus cavity radius (r_c) when $m < m^*$ (blue curve), and when $m = m^*$ (yellow curve). Here m is the number of helium atoms in a bubble, and m* is the critical number at shich the bubble transforms into a growing void.

As materials undergo irradiation, He diffuses to cavities and the number of He atoms in the cavity (m) increases. The influx of He causes the growth rate curve to shift up, thus r_b increases and r_v^* decreases. Eventually, a critical value of He atoms (m*) will be reached and the equation will only have one root, here termed as the critical bubble radius r_b^* (purple star in Figure 2.2). This critical scenario is shown with a yellow curve in Figure

2.2. The addition of more He beyond m* causes the curve to shift up completely into the $dr_c/dt > 0$ region at which point the cavity will grow regardless of radius. The equations for m* and r_b* are [14]:

$$m^* = \frac{32F_V\theta_1\gamma_{MC}^3\Omega_V^2}{27(kT)^3\ln(\Lambda)^2}$$

$$r_b^* = \frac{4\theta_2\gamma_{MC}\Omega_V}{3kT\ ln(\Lambda)}$$

Here θ_1 and θ_2 are correction curves used to fit non-ideal gas behavior and F_V is a shape factor which equals $4\pi/3$ for full spheres, and less for heterogeneous nucleation. Both m* and r* are dependent on the matrix-cavity interface energy and on the supersaturation of vacancies (Λ). Thus, it is important to find materials that keep $r_c < r_b$*.

In conclusion, two of the key challenges in developing materials for fusion applications are managing displacement damage and managing very high levels of He.

2.2 Nanostructured Ferritic Alloys

Novel structural materials for fusion reactor applications are required to have superior strength, thermal creep resistance and radiation damage resistance. Little can be done to alter the initial neutron-induced displacement damage, and future reactor designs call for structural materials that will be exposed to damage levels up to 200 dpa. A key strategy for designing radiation resistant materials is to promote vacancy and SIA recombination, allowing the material to “self-heal”. As previously mentioned, voids can lead to macroscopic swelling and degradation of material properties. A way to manage He

is to immobilize it in small stable bubbles throughout the structure, thereby delaying the onset of void formation, protecting grain boundaries, and enhancing defect recombination.

Nanostructured Ferritic Alloys (NFAs) are a revolutionary class of Fe-Cr-based oxide dispersion strengthened (ODS) steels with potential applications for fusion and fission reactor systems. NFAs have many outstanding properties that include high tensile, creep, and fatigue strengths over a wide range of temperature; remarkable thermal stability up to 1000 °C; and unmatched radiation resistance, especially with respect to managing high levels of He [4,14,17,18]. The outstanding properties primarily stem from the presence of a high density of small Y-Ti-O nano-oxides (NOs). The NOs: (1) retard dislocation climb and glide thus increasing material strength; (2) stabilize grain and dislocation structures; and (3) act as deep traps for He, resulting in the formation of small, high-pressure gas bubbles at NO-matrix interfaces. The high density of small bubbles adds to the radiation tolerance of NFAs by acting as recombination centers for defects. Thus, NFAs may turn high He levels from a liability to an asset [14,18].

2.2.1 Composition and Structure

NFA compositions range from alloy to alloy. MA957, is a historically viewed as a reference NFA, and has a composition of 14 wt% Cr, 0.2 Y, 1.0 Ti, 0.2 O, 0.3 Mo, and bal. Fe [4,19,20]. Further, a best-practice heat termed NFA-1 has a composition of 14 Cr, 0.25 Y, 0.35 Ti, 0.08 O, 3 W, 0.016 Al, 0.002 N, and bal. Fe [4,21]. NFAs are typically fabricated by ball milling pre-alloyed metal 14Cr-Fe-Ti-W powders with yttria (Y_2O_3)

powders [17,21,22]. High-energy milling breaks apart the Y_2O_3 particles and forces the practically insoluble yttrium into solution. The milled powders are then canned, degassed, and usually consolidated by hot isostatic pressing or hot extrusion. The yttrium, titanium, and oxygen precipitate as NOs during consolidation. The NO number densities (N), average diameters (<d>), and size distributions depend on the alloy composition and consolidation history. As the consolidation temperature drops below 1150 °C, the NO density and volume fraction (f) increases whereas <d> decreases. Consolidation is usually carried out from 850 °C to 1150 °C, yielding $N = 10^{23\text{-}24}/m^3$, f = 0.5 to 1%, and <d> = 1 to 5 nm NOs [18].

The as-consolidated alloys usually have a bimodal grain size distribution, where smaller grains are <1 μm, and larger grains can be 10 μm or greater. Extrusion leads to elongated grains with a {110} fiber texture, and dislocation densities of $0.5x10^{15}/m^2$ to $2x10^{15}/m^2$ [4]. NFA consolidation is usually followed by thermo-mechanical processing steps to improve properties and obtain final product shapes.

2.2.2 Character of the Nano-Oxides (NOs)

Characterization the Y-Ti-O NOs is an ongoing effort by many researchers throughout the world. A key question is: what are the NO compositions, structures, and matrix interface orientation relationships (ORs)? Obtaining answers is complicated by: (1) the presence of many precipitate phases in NFAs over a wide range of sizes, (2) the variation in specific NO phases due to alloy chemistry and processing, and (3)

inconsistencies in the measurements obtained through a variety of characterization tools. Atom probe tomography (APT) results indicate that the smallest NOs (< 5 nm) are non-stoichiometric Guinier-Preston zone-like phases, with high Ti/Y ratios [23,24]. However, small-angle neutron scattering (SANS) results are not consistent with large Ti/Y ratios. Some transmission electron microscopy (TEM) studies found NOs with amorphous [25] or rock-salt structures [26]. Most TEM and x-ray diffraction (XRD) studies found fcc pyrochlore $Y_2Ti_2O_7$ for smaller NOs (<5 nm) [27], but orthorhombic Y_2TiO_5 [20,28] and cubic TiO [26] for larger NOs. TEM indicates Y/Ti ratios of 0.5 to 1.5. SANS and small angle x-ray scattering (SAXS) characterizations also indicate $Y_2Ti_2O_7$. Some APT and TEM observations suggest that NOs have a core-shell structure with $Y_2Ti_2O_7$ oxide core surrounded by a Ti-rich shell [24,29]. This would explain some of the discrepancies between SANS, APT and TEM. Also, a Y/Ti-rich NO termination is expected according to first principles modeling [30]. Note that the NO character depends on the alloy composition and processing, so variation in NO type is not entirely unexpected.

A recent study by Wu et al. [31] unambiguously showed that most of the NOs in a NFA MA957 alloy are pyrochlore $Y_2Ti_2O_7$ (YTO). Figure 2.3a is a bright field TEM image from a friction stir welded and annealed lift-out, showing the cuboidal NO features. NOs typically have elongated shapes with sizes widely ranging from ~1 to 12 nm. Figure 2.3b is a high resolution STEM image of a 1.8 nm x 3.8 nm pyrochlore $Y_2Ti_2O_7$ NO from the same alloy in Figure 2.3a.

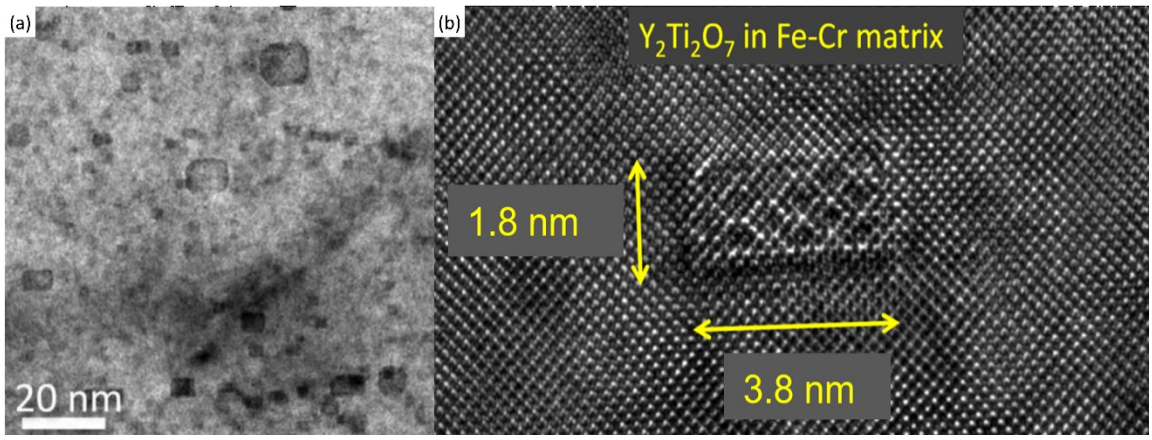

Figure 2.3 – (a) Bright field TEM image of cuboidal NOs in friction stir welded MA957. (b) High resolution STEM image of a nano-oxide. Images reproduced from reference [31].

2.2.3 NO – Matrix Orientation Relationships

The NO-matrix crystallographic orientation relationships (ORs) are of fundamental interest because they affect critical properties such as interface energies, misfit strains, and defect structures. These characteristics are important to NO interactions with point defects, He, and dislocations. Knowing the ORs is also critical to calibrating first principles and atomistic interface models [30,32,33].

There is a nomenclature difference between bulk ORs and interfacial ORs. Bulk ORs refer to the overall relationship between two crystal lattices. The nomenclature involves listing a pair of non-linearly related parallel planes and/or directions between the two lattices. Interfacial ORs describe the specific planes that are touching at an interface and at least one set of parallel directions along that plane. For example, the edge-on-cube interfacial OR: {110}Fe//{100}YTO with <110>Fe//<100>YTO indicates that the

{110}Fe plane is matched with the {100}YTO plane at the interface, and the <100>Fe direction is parallel to the <100>YTO direction along the interface.

Each embedded NO has only one bulk OR with the matrix (which can be named in multiple ways), but may have many different interfacial ORs depending on how the particle is faceted (each interface is characterized by the specific joining planes). In many cases, the NOs have been shown to be cuboidal with flat matrix-YTO interfaces. The bulk and associated interfacial ORs have been summarized in Table 2.1. Note that the literature on NOs is vast, and Table 2.1 only includes references where the interfacial ORs were reported.

The most common bulk ORs for embedded NOs are cube-on-cube and cube-on-edge. Depending on how the NOs are faceted, they can have multiple types of interfaces with different interfacial ORs. The NOs are not perfect cubes and have been reported to have {100}, {110}, and {111} YTO planes that match with the surrounding ferrite matrix. To further study the metal-YTO interfaces, bilayers were fabricated by Fe deposition on {100}, {110}, and {111} oriented single crystal $Y_2Ti_2O_7$ substrates. These results are discussed in detail in later chapters, but are also summarized in Table 2.1.

Table 2.1 – Summary of bulk and interfacial ORs for embedded $Y_2Ti_2O_7$ NOs and for Fe depositions on single crystal $Y_2Ti_2O_7$ (bilayers).

Bulk OR	Interface OR	Interface OR	Embedded NOs	Bilayers
Cube on Cube	Face on Face	{100}Fe // {100}YTO <100>Fe // <100>YTO <110>Fe // <110>YTO	Dawson [34] Ribis [35]	
Cube on Cube	Edge on Edge	{110}Fe // {110}YTO <100>Fe // <100>YTO <110>Fe // <110>YTO	Dawson [34]	
Cube on Cube	Corner on Corner	{111}Fe // {111}YTO <110>Fe // <110>YTO <112>Fe // <112>YTO	Dawson [34]	
Cube on Edge	Face on Face	{100}Fe // {100}YTO <110>Fe // <100>YTO <100>Fe // <110>YTO	Dawson [34] Wu [31] Miao [36]	Fe-100YTO patch
Cube on Edge	Edge on Face	{110}Fe // {100}YTO <100>Fe // <100>YTO <110>Fe // <100>YTO	Dawson [34]	
Cube on Edge	Face on Edge	{100}Fe // {110}YTO <100>Fe // <100>YTO <100>Fe // <110>YTO	Miao [36] Wu [31] Badjeck [37]	Fe-110TYO large area
Cube on Edge	Edge on Corner	{110}Fe // {111}YTO <100>Fe // <110>YTO <110>Fe // <112>YTO	Miao [36] Wu [unpublished]	Fe-111TYO dominant OR
Rotated Cube on Edge	Face on Edge	{100}Fe // {110}YTO <110>Fe // <100>YTO <110>Fe // <110>YTO	Miao [36]	
Rotated Edge on Cube	Rotated Edge on Face	{110}Fe // {100}YTO <111>Fe // <110>YTO <112>Fe // <110>YTO		Fe-100YTO dominant OR
Cube on Corner	112 on Edge	{112}Fe // {110}YTO <110>Fe // <110>YTO <111>Fe // <100>YTO	Ribis [38]	
Cube on Corner	Face on Corner	{100}Fe // {111}YTO <100>Fe // <110>YTO <100>Fe // <112>YTO		Fe-111YTO with interlayer
Axiotaxy on Edge	Axiotaxy on Edge	Axiotaxy // {110}YTO		Fe-110YTO dominant OR

2.2.5 Fe and $Y_2Ti_2O_7$ Bulk Properties

The two primary structures of interest in this study are Fe and $Y_2Ti_2O_7$. The room temperature α phase of Fe has a bcc structure with a lattice parameter of 2.88 Å and two atoms per unit cell. Upon cooling, pure Fe melts from liquid to α at 1811K, then transforms from α to fcc γ at ~1653K, then back to α at ~1160K [39]. In NFAs, the transformation to γ Fe is avoided due to the addition of Cr and other alloying elements.

$Y_2Ti_2O_7$ has a fcc pyrochlore structure (space group Fd-3m) with a lattice parameter of 10.095 Å and a total of 88 atoms per unit cell. The structure has two nonequivalent O sites (O and O') and Ti in octahedral symmetry sites. Y, Ti, O and O' atoms are located respectively at 16d (1/2, 1/2, 1/2), 16c (0, 0, 0), 48f (x, 1/8, 1/8) and 8b (3/8, 3/8, 3/8) Wyckoff positions with x = 0.328 [40]. The two non-equivalent oxygen sites, O and O', differ in chemical environment: each O resides in a Y + Ti-tetrahedron (defined by two Y and two Ti atoms), while each O' resides in a Y-tetrahedron (defined solely by Y atoms). Each O-site is displaced due to the neighboring unoccupied Ti-tetrahedrons (defined solely by Ti atoms). Pyrochlore $Y_2Ti_2O_7$ has a quite open structure and possesses two types of polyhedral interstitial sites. One is the tetrahedral interstitial site (Figure 2.4a), each surrounded by four Ti atoms, and the other is the octahedral interstitial site (Figure 2.4b), each surrounded by three Y and three Ti atoms. Figure 2.4c shows the geometric relation between the two interstitial types in $Y_2Ti_2O_7$. Each tetrahedron shares a face with four neighboring octahedra.

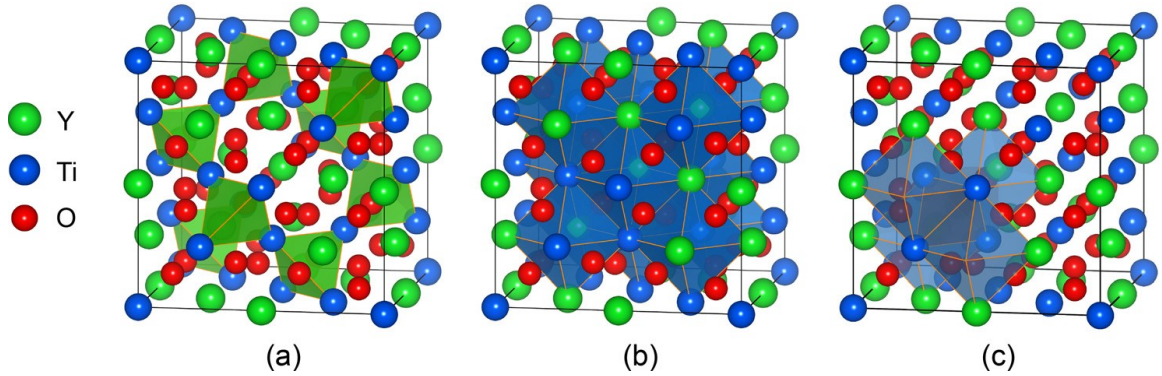

Figure 2.4 – $Y_2Ti_2O_7$ pyrochlore structure. (a) Tetrahedral sites are shown with green polygons. (b) Octahedral interstitial sites are shown in blue. (c) The tetrahedral-octahedral site geometric relation in $Y_2Ti_2O_7$. Figure reproduced from reference [41].

Table 2.2 contains many of the known properties of Fe and $Y_2Ti_2O_7$. The materials have different cubic crystal structures, lattice parameters, densities, and melting points. The thermal expansions, Young's moduli, bulk moduli, and Poisson ratios are similar.

Table 2.2 – Properties of bulk Fe and $Y_2Ti_2O_7$.

Property	**Fe**	**$Y_2Ti_2O_7$**
Crystal Structure	Bcc	Fcc
Lattice parameter (Å)	2.886	10.095
Atoms in unit cell	2	88
Atomic density ($x10^{28}/m^3$)	8.32	8.55
Melting point (K)	1811	2321
Density (g/cm^3)	7.87	4.84
Thermal Expansion ($x10^6$/K at 25 °C)	11.80	10.46
Young's modulus (GPa)	211	262
Shear modulus (GPa)	82	103
Bulk modulus (GPa)	170	190
Poisson ratio (GPa)	0.29	0.27

2.2.6 NFA Interactions with Helium

The details of He interactions with NFAs are not yet fully understood. Recent first principles modeling by Jiang et al. [30,32] have shed light on the underlying mechanisms. The calculated energies of He atoms at different sites in an NFA is shown at the top of Figure 2.5**Error! Reference source not found.**a [30,32]. A large YTO NO is shown in orange, He atoms are gray, and interfacial bubbles are green. The calculations indicate that He energies are lowest in the octahedral sites of oxide (He^{I}_{octa} = 0.94 eV/atom), and at the YTO-matrix interface (He_T = 0.95 eV/atom). These energies are nearly identical, and much lower than in the ferritic matrix (He_V = 2.28 eV/atom). Figure 2.5b shows a ~1 nm NO with a small interfacial bubble. The calculated matrix-NO interface energy for a Fe-YTO cube-on-cube OR is $\gamma_{MN} \approx 0.8$ J/m^2 [30]. The interface energies are expected to vary for different ORs.

Figure 2.5c shows the energy of He in a cavity as a function of radius (r_c). The horizontal black line indicates the energy of He in an interfacial bubble (He_T = 0.95 eV/atom). Thus, bubble nucleation and growth occurs only for cavities with a radius larger than $r_b \approx 0.5$ nm. That is, the NO interfaces act as heterogeneous sites for He bubble nucleation.

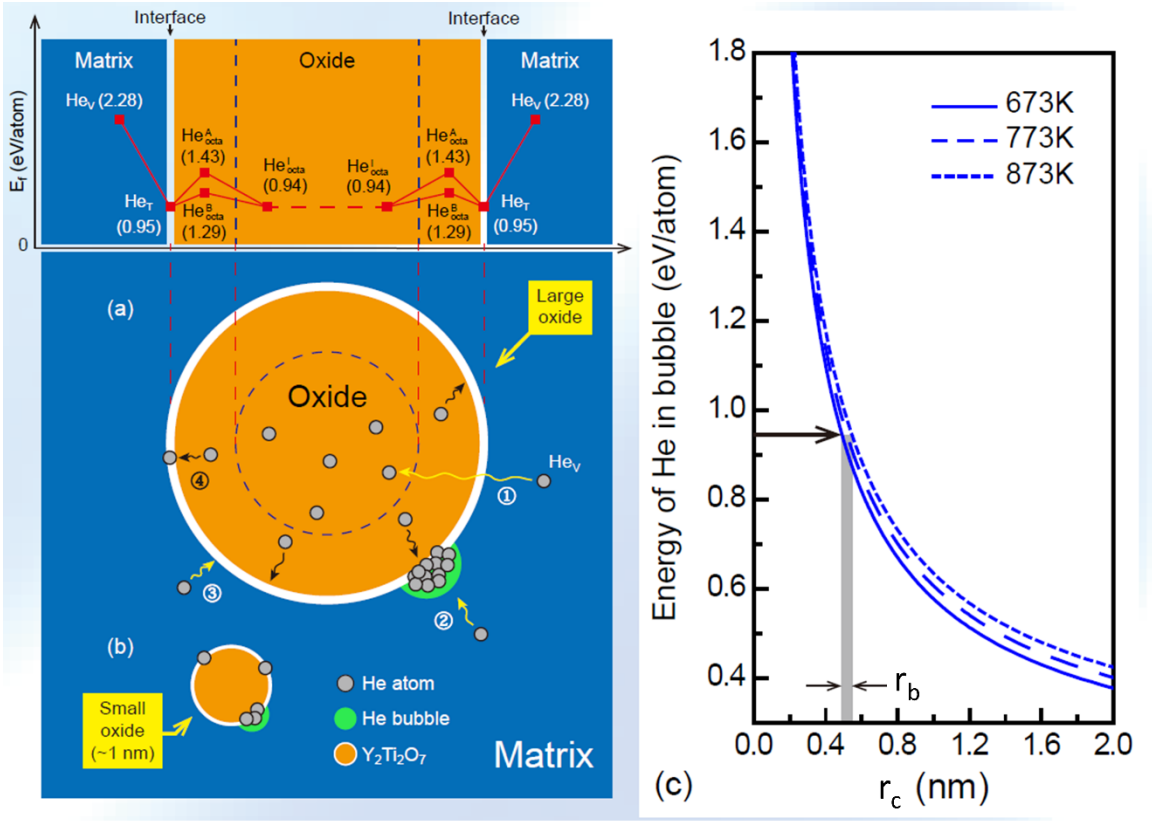

Figure 2.5 – First principles modeling results of: (a) an embedded $Y_2Ti_2O_7$ oxide in a ferrite matrix with corresponding He formation energies (top), and (b) a small NO. (c) Plot indicating the energy of He in a cavity of radius r_c and the radius for bubble formation r_b at an Fe-$Y_2Ti_2O_7$ interface. Image reproduced from reference [30].

The overall sequence of events is shown in Figure 2.6. He is produced in the through transmutation reactions (step 1 in Figure 2.6) and has an energy of 2.28 eV/atom. He can diffuse through the lattice until it finds a lower energy site. He atoms can cluster (step 2a) and start to form bubbles. In Fe, a bubble will nucleate (step 3a) if the radius r > 0.2 nm.

If a He atom instead diffuses to a NO (step 2b), it will enter the YTO structure and have a lower energy of 0.94 eV/atom. Bubbles can form at the YTO-matrix interface (step 3b) if the radius r > 0.5 nm. Inside the bubble, the energy per He atom decreases with increasing bubble size ($E \approx 4\gamma/r$). Once a sufficiently sized bubble has nucleated, He inside the NO will diffuse to the interfacial bubble (step 4b). Thus, the NOs act as "He storage tanks". Smaller NOs are expected to be associated with smaller bubbles, while larger oxides have larger bubbles. In NFAs, the ultrahigh number of very small NOs disperse He into small stable bubbles thus delaying the onset of void swelling.

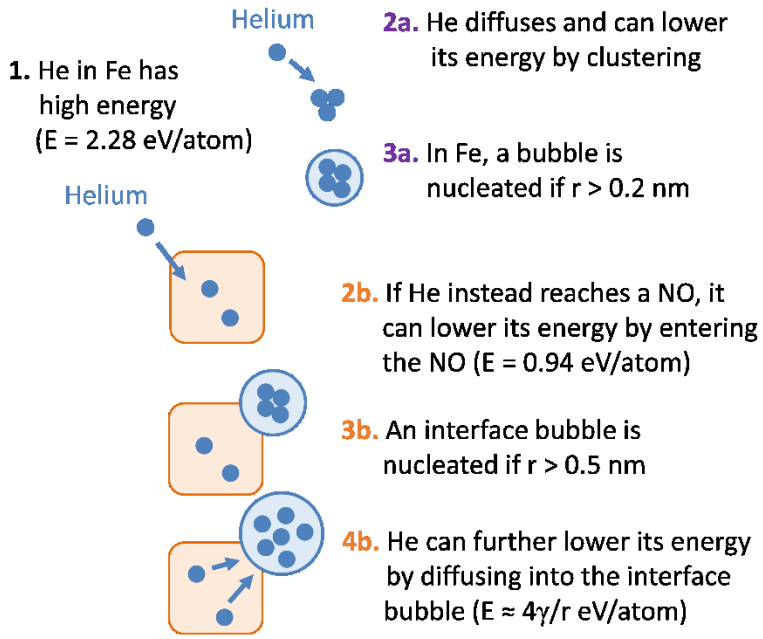

Figure 2.6 – Helium bubble formation mechanism in NFAs.

The heterogeneous nucleation of cavities at NO-matrix interfaces involves the balance of three interfacial energy terms: a matrix-NO interface (γ_{MN}), a matrix-cavity

interface (γ_{MC}), and a NO-cavity interface (γ_{NC}). Figure 2.7 shows a cavity at a NO-matrix interface with wetting angle θ. The tensions balance using Young's equation [42]:

$$\gamma_{MN} = \gamma_{NC} + \gamma_{MC}\cos\theta$$

Given approximate values for the three energies: $\gamma_{MN} \approx 0.8$ J/m^2 [30], $\gamma_{NC} \approx 1$ J/m^2 [40], and $\gamma_{MC} \approx 1.8$ J/m^2 [4], the wetting angle $\theta \approx 96°$. Thus, the bubbles weakly wet the NO surfaces. Large wetting angles are desired for the management of He in candidate structural alloys. If the wetting angle is small, the critical radius (r_c*) and number of He atoms (m*) for the conversion of bubbles to voids is reached with fewer He atoms than if the bubble were to homogeneously nucleate in the matrix. Thus, to minimize wetting, alloys should be designed to have small matrix-NO interface energies and large NO-cavity surface energies.

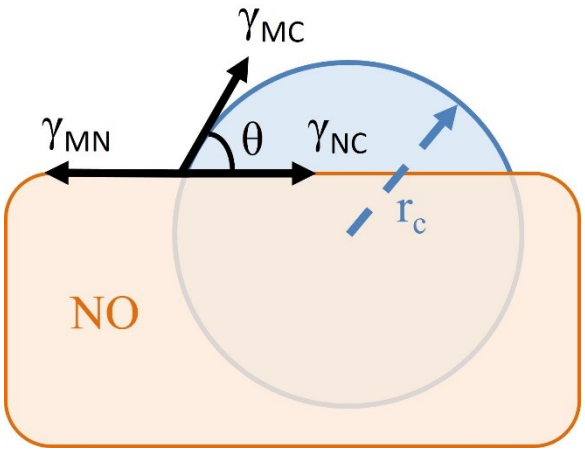

Figure 2.7 – Heterogeneous nucleation of a cavity on a NO involves three interfacial energies: matrix-NO (γ_{MN}), matrix-cavity (γ_{MC}), and NO-cavity (γ_{NC}).

2.3 Summary of Effects

In summary, structural materials with first wall/blanket applications will be subject to extreme conditions. The alloys must manage the defects produced by radiation damage and large quantities of transmutation-produced He, with end of life reactor goals of 200 dpa and 2000 appm He, respectively [4,17]. Schematic illustrations of some of the relevant mechanisms are shown in Figure 2.8 for (a) most materials, and (b) in NFAs which are strengthened a high number density of small NOs. In both cases defects are produced in equal numbers and can recombine in the matrix, or lose their identities at sinks in the material. As shown in Figure 2.8a, dislocations and loops preferentially attract interstitials (long red arrows) which leaves behind a supersaturation of vacancies which diffuse to helium bubbles, unstably growing voids, and stress-driven grain boundary cavities. These effects lead to a considerable amount of swelling in most materials and degradation of material properties. In NFAs (Figure 2.8b) the NOs pin dislocations and trap He in small stable bubbles. Importantly, NFAs do not swell because the He bubble radii are smaller than the critical value necessary for conversion into voids, and because NFAs have a high number density of neutral sinks which lowers the supersaturation of vacancies. For these reasons, and others described previously, NFAs show promise as good candidate structural materials for future fusion reactors.

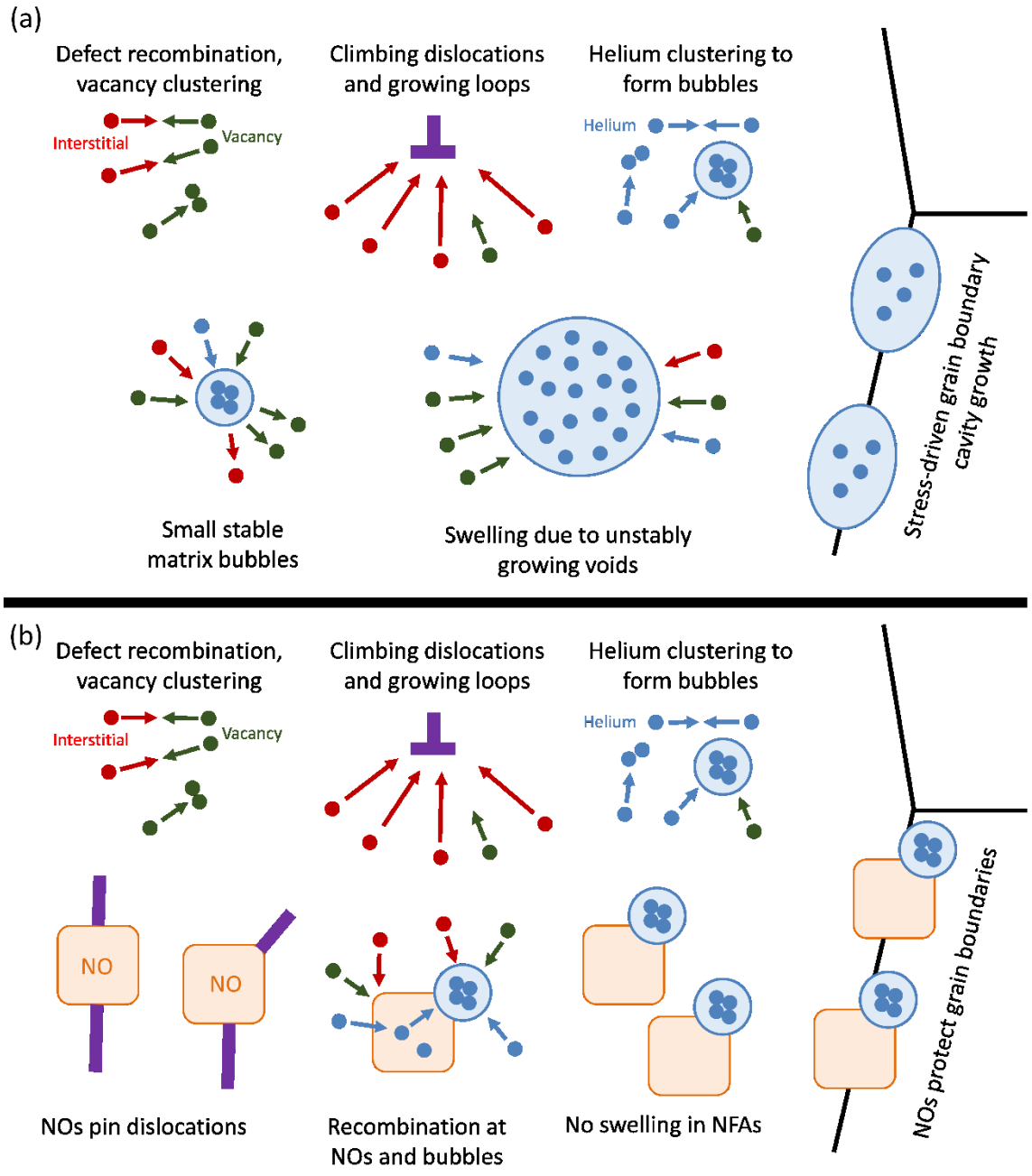

Figure 2.8 – (a) General effects due to radiation damage and presence of He in most structural materials, and (b) effects in NFAs containing a high number density of small NOs.

2.4 References

[1] International Energy Agency, Key World Energy Statistics 2016, Paris, 2016.

[2] J. Diefenderfer, M. assumptions Vipin Arora, L.E. Singer, DOE/EIA-0484 (2016) 202–586.

[3] E.E. Bloom, J.T. Busby, C.E. Duty, P.J. Maziasz, T.E. McGreevy, B.E. Nelson, B.A. Pint, P.F. Tortorelli, S.J. Zinkle, J. Nucl. Mater. 367 (2007) 1–10.

[4] G.R. Odette, JOM 66 (2014) 2427.

[5] S.J. Zinkle, J.T. Busby, Mater. Today 12 (2009) 12–19.

[6] E.E. Bloom, S.J. Zinkle, F.W. Wiffen, J. Nucl. Mater. 329 (2004) 12–19.

[7] A. Eddington, The Internal Constitution of the Stars, University Press, Cambridge, 1926.

[8] F. Najmabadi, A. Abdou, L. Bromberg, T. Brown, V.C. Chan, M.C. Chu, F. Dahlgren, L. El-Guebaly, P. Heitzenroeder, D. Henderson, H.E. St. John, C.E. Kessel, L.L. Lao, G.R. Longhurst, S. Malang, T.K. Mau, B.J. Merrill, R.L. Miller, E. Mogahed, R.L. Moore, T. Petrie, D.A. Petti, P. Politzer, A.R. Raffray, D. Steiner, I. Sviatoslavsky, P. Synder, G.M. Syaebler, A.D. Turnbull, M.S. Tillack, L.M. Waganer, X. Wang, P. West, P. Wilson, Fusion Eng. Des. 80 (2006) 3–23.

[9] N. Holtkamp, Fusion Eng. Des. 84 (2009) 98–105.

[10] N. Holtkamp, Fusion Eng. Des. 82 (2007) 427–434.

[11] E.E. Bloom, J. Nucl. Mater. 258 (1998) 7–17.

[12] A.R. Raffray, M. Akiba, V. Chuyanov, L. Giancarli, S. Malang, J. Nucl. Mater.

(2002).

[13] D.L. Smith, M.C. Billone, S. Majumdar, R.F. Mattas, D.-K. Sze, J. Nucl. Mater. 258 (1998) 65–73.

[14] Y. Dai, G.R. Odette, T. Yamamoto, The Effects of Helium in Irradiated Structural Alloys, 1st ed., Elsevier Inc., 2012.

[15] R.S. Averback, J. Nucl. Mater. 216 (1994) 49–62.

[16] S.J. Zinkle, B.N. Singh, J. Nucl. Mater. 199 (1993) 173–191.

[17] G.R. Odette, M.J. Alinger, B.D. Wirth, Annu. Rev. Mater. Res. 38 (2008) 471–503.

[18] G.R. Odette, D.T. Hoelzer, JOM 62 (2010) 84–92.

[19] M.J. Alinger, G.R. Odette, D.T. Hoelzer, Acta Mater. 57 (2009) 392–406.

[20] T. Stan, D.J. Sprouster, A. Ofan, G.R. Odette, L.E. Ecker, I. Charit, J. Alloys Compd. 699 (2017) 1030–1035.

[21] N.J. Cunningham, Y. Wu, A. Etienne, E.M. Haney, G.R. Odette, E. Stergar, D.T. Hoelzer, Y.D. Kim, B.D. Wirth, S.A. Maloy, J. Nucl. Mater. 444 (2014) 35–38.

[22] N. Cunningham, G.R. Odette, (n.d.) 1093–1094.

[23] M.K. Miller, E.A. Kenik, K.F. Russell, L. Heatherly, D.T. Hoelzer, P.J. Maziasz, Mater. Sci. Eng. A 353 (2003) 140–145.

[24] E.A. Marquis, Appl. Phys. Lett. 93 (2008) 10–13.

[25] M.C. Brandes, L. Kovarik, M.K. Miller, G.S. Daehn, M.J. Mills, Acta Mater. 60 (2012) 1827–1839.

[26] A. Hirata, T. Fujita, C.T. Liu, M.W. Chen, Acta Mater. 60 (2012) 5686–5696.

[27] A.J. London, B.K. Panigrahi, C.C. Tang, C. Murray, C.R.M. Grovenor, Scr. Mater. 110 (2016) 24–27.

[28] Y. Wu, E.M. Haney, N.J. Cunningham, G.R. Odette, Acta Mater. 60 (2012) 3456–3468.

[29] S. Liu, G.R. Odette, C.U. Segre, J. Nucl. Mater. 445 (2014) 50–56.

[30] L. Yang, Y. Jiang, Y. Wu, G.R. Odette, Z. Zhou, Z. Lu, Acta Mater. 103 (2016) 474–482.

[31] Y. Wu, J. Ciston, S. Kräemer, N. Bailey, G.R. Odette, P. Hosemann, Acta Mater. 111 (2016) 108–115.

[32] L. Yang, Y. Jiang, G. Robert Odette, T. Yamamoto, Z. Liu, Y. Liu, J. Appl. Phys. 115 (2014) 143508.

[33] L. Barnard, N. Cunningham, G.R. Odette, I. Szlufarska, D. Morgan, Acta Mater. 91 (2015) 340–354.

[34] K. Dawson, G.J. Tatlock, J. Nucl. Mater. 444 (2014) 252–260.

[35] J. Ribis, Y. De Carlan, Acta Mater. 60 (2012) 238–252.

[36] Y. Miao, K. Mo, B. Cui, W. Chen, M.K. Miller, K.A. Powers, V. Mccreary, D. Gross, J. Almer, I.M. Robertson, J.F. Stubbins, Mater. Charact. 101 (2015) 136–143.

[37] V. Badjeck, M.G. Walls, L. Chaffron, J. Malaplate, K. March, J. Nucl. Mater. 456 (2015) 292–301.

[38] J. Ribis, S. Lozano-Perez, J. Nucl. Mater. 444 (2014) 314–322.

[39] W. Xiong, P. Hedström, M. Selleby, J. Odqvist, M. Thuvander, Q. Chen, Calphad 35 (2011) 355–366.

[40] L. Yang, Y. Jiang, G.R. Odette, W. Zhou, Z. Liu, Y. Liu, Acta Mater. 61 (2013) 7260–7270.

[41] Y. Jiang, L. Yang, Y. Jin, G.R. Odette, (2014) 163.

[42] D.A. Porter, K.E. Easterling, M.Y. Sherif, Phase Transformations in Metals and Alloys, 3rd ed., CRC Press, Boca Raton, 2009.

Chapter 3 X-Ray Absorption Spectroscopy

3.1 Introduction

This chapter has been published in the Journal of Alloys and Compounds [1]. Some of the major challenges facing nanostructured ferritic alloys (NFAs) include characterization of the nano-oxide (NO) sizes, number densities, structures, compositions, and oxide-matrix interfaces. These characteristics depend on the alloy composition and processing history. NO characterization is complicated by the presence of many precipitate phases that range from one to hundreds of nanometers. Further, the various methods used to characterize NOs do not always yield the same results. Studies have been interpreted to show NOs that range from solute enriched clusters with core-shell structures to various complex oxides, such as fcc $Y_2Ti_2O_7$ and orthorhombic Y_2TiO_5. Some atom probe tomography (APT) studies suggest NOs are non-stoichiometric Guinier-Preston zone-like phases with high Ti/Y ratios [2–6]. However, most transmission electron microscopy (TEM) [7–13] and small angle neutron and x-ray scattering (SANS and SAXS) [10,14,15] studies report structures and chemistries that are primarily consistent with the fcc pyrochlore $Y_2Ti_2O_7$ phase.

Previous TEM and SANS studies on reference NFA MA957 indicate NO averages for number densities of $N \sim 5 \times 10^{23}$ m^{-3}, average diameters $\langle d \rangle \sim 2.5$ nm, and volume

fractions of <f> ~ 0.45% [16]. The smallest (d < 5 nm) NOs were found to be primarily $Y_2Ti_2O_7$, while larger (d > 6 nm) NOs were primarily orthorhombic Y_2TiO_5. Larger (d > 50 nm) Y_2O_3, TiO_x, Mo-rich, and C-N rich precipitates have also been observed. Unpublished x-ray diffraction (XRD) results also show the presence of TiO. Given the low volume fractions and ultra-small NO sizes, a synchrotron light source is needed to obtain reliable x-ray measurements. In this study, we performed a comprehensive x-ray absorption spectroscopy (XAS) analysis as a complement to XRD and SAXS measurements.

The wide variety of precipitate phases and sizes in NFAs complicates conventional XAS analysis. The many scattering environments cause significant overlap in spectrum features characteristic of the individual phases. In the particular case of NFA MA957, ≈ 2/3 of the total Ti is left in solution and only 1/3 is contained in the various nano-oxides [17]. A previous XAS report by Liu et al. indicated nearly equal amounts of $Y_2Ti_2O_7$, Y_2TiO_5, and Y_2O_3 in MA957[18].

In this study, we build on previous XAS work by using the log-ratio method to analyze the complex MA957 XAS spectra. We also detail a bulk extraction and selective filtration method to dissolve the alloy matrix and isolate one component of the NOs populations. We demonstrate that the filtration procedure not only yields samples that are geometrically ideal for XAS measurements, but also removes the problematic environments that hinder conventional analysis.

3.2 Bulk Extraction and Filtration Method

INCO NFA MA957 with a nominal composition of 14.9Cr, 1.1Ti, 0.17Mo, 0.13Y, 0.88O, bal. Fe (at%), along with trace impurity elements such as Al, Mn, Si and C [19] was examined in this study. The alloy was extruded at ~1060 °C. XAS measurements were performed on the as-extruded MA957 alloy containing embedded NOs, and on filters containing extracted NOs.

A bulk extraction and selective filtration method was used to isolate a NO population. The procedure is outlined in Figure 3.1. MA957 was placed in a platinum wire mesh (Figure 3.1a) and submerged into a 1 L solution composed of 100 mL acetyl acetone, 10 g of tetra methyl ammonium chloride, and a balance of methanol. A 20 V potential was used to dissolve the MA957 matrix. The non-acetic solution is dark red at the end of the 24 h process (Figure 3.1b). A 100 nm-pore filter was first used to remove very large particles (not shown in Figure 3.1). The remaining liquid was drained through a polysulfone 10 nm-pore filter for 50 h. The process was accelerated by connecting a fume-hood vacuum to the filtration capsule (Figure 3.1c). The filter containing NOs was used for XAS measurements (Figure 3.1d). This procedure yields a roughly spatially uniform distribution of NOs in the filter, which is ideal for XAS studies.

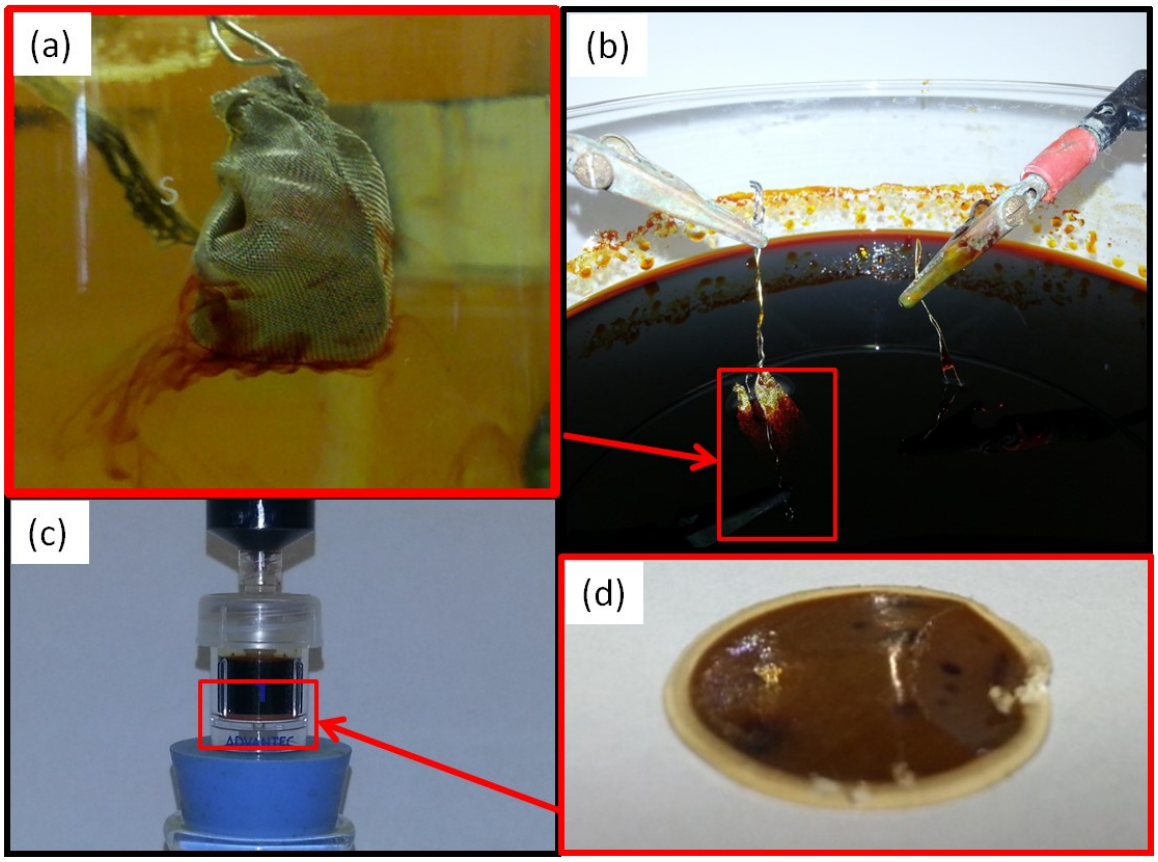

Figure 3.1 – (a) MA957 in platinum wire mesh being dissolved; (b) The initially clear yellow liquid is dark red at the end of the process; the liquid is then pre-treated by 100 nm-pore filtration (not shown); (c) a vacuum under a 10 nm-pore filter is used to accelerate the process; and, (d) the filter containing NOs is removed and used for XAS measurements.

3.3 XAS Parameters

Both as-received MA957 alloy containing embedded NOs, and filters containing selectively extracted NOs, were studied using XAS fluorescence and transmission-mode measurements at beamline X23A2 of the National Synchrotron Light Source at Brookhaven National Laboratory. Ambient temperature XAS spectra were measured at the

Ti and Y *K*-edges (4.492 keV and 17.038 keV, respectively), at a photoelectron wavenumber (*k)* value of 13 $Å^{-1}$. Ti metal and Y_2O_3 powder were simultaneously measured in transmission mode for energy calibration. Background subtraction, spectra alignment, and normalization of the extended x-ray absorption fine structure (EXAFS) data were carried out using the ATHENA code [20]. The positions of the Ti and Y edges were determined from the reference absorption spectra using known features. Isolated EXAFS spectra were then Fourier Transformed (FT) over a *k* range of 3.0 – 11 $Å^{-1}$ and back FT over a non-phase-corrected radial distance of 0.9 – 2.4 Å to isolate the signal from the first nearest neighbor atoms (Ti-O and Y-O bonds).

Application of model-dependent analysis methods (using a combination of Artemis, IFEFFIT and FEFF) was found to be difficult due to structural disorder and weak signals present in the samples. Instead, structural parameters were determined using the model-independent, or log-ratio, method [21]. This purely empirical technique is most useful for data where the signals from nearest neighbor (NN) atoms are spectrally isolated from the rest. The log-ratio method is commonly used to probe atomic changes with temperature/pressure, and has been used in both crystalline and amorphous materials [22]. Fitting of the log-ratio of amplitudes ($\ln[A_{NO}(k)/A_S(k)]$) and phase-difference [$\Phi_{NO}(k)$-$\Phi_S(k)$] of the isolated first NN atoms was performed using ATHENA over a *k* range of ~3 – 8 $Å^{-1}$ (depending on the edge) with polynomials of the forms shown below:

$$\frac{\Phi_{NO}(\mathrm{k}) - \Phi_S(\mathrm{k})}{2k} = (BL_{NO} - BL_S) - \frac{4}{3}k^2(C_{3NO} - C_{3S})$$

$$\ln\left(\frac{A_{NO}(k)}{A_S(k)}\right) = \ln\left(\frac{CN_{NO}}{CN_S}\right) - 2k^2(\sigma_{NO}^2 - \sigma_S^2)$$

The log-ratio technique yields *differences* in the structural parameters between the sample under investigation (subscript NO) and a known standard (subscript S). The reported differences in the bond length ($\Delta BL = BL_{NO} - BL_S$), Debye – Waller factor ($\Delta\sigma^2 = \sigma_{NO}^2 - \sigma_S^2$), asymmetry parameter ($\Delta C_3 = C_{3NO} - C_{3S}$) and ratio of the coordination numbers (CN_{NO}/CN_S) are relative to the bulk standards, and were allowed to vary.

3.4 XANES Results

The XAS spectra are plotted as absorption versus x-ray energy, and consist of an x-ray absorption near edge structure (XANES) region with a broad edge and, in some cases, a pre-edge peak at lower energy, and an extended x-ray absorption fine structure (EXAFS) oscillating region at energies beyond the edge. The Ti and Y *K*-edge XANES spectra are shown in Figure 3.2 for the embedded and extracted oxides, along with those for bulk standards. In Figure 3.2, some curves have been vertically offset for clarity. The pre-edge peaks and broad features observed in the XANES spectra result from multiple-scattering resonances, and can be used to identify the crystallographic phase, symmetry and oxidation state of the metal ions [23,24]. At the Ti edge in Figure 3.2a, the Ti atoms in the bulk MA957 (embedded) show a complex mixture of environments, similar to metallic Ti, $Y_2Ti_2O_7$ and TiO. Note the higher intensity in the 4.99 – 5.02 keV range and subtle shifts relative to the bulk standards.

In contrast, the extracted NOs show a sharp pre-edge peak that is more characteristic of the Y_2TiO_5 phase. Additionally, the general shape and the features in the edge (~4.98 – 5.0 keV) are most similar to the Y_2TiO_5 phase. The broad features in the XANES spectrum suggest structural disorder in the extracted NOs, likely due to their small size and complex chemistry. This observation is consistent with other nanoparticle studies, where changes in the XANES regions from structural and chemical disorder are reported [25].

The XANES spectra at the Y edge (Figure 3.2b) show features for the embedded NOs that are almost identical to the $Y_2Ti_2O_7$ standard. A small Y_2O_3 component may also be present in the embedded measurement as indicated by a subtle increase in intensity between 17.05 – 17.07 keV and 17.10 – 17.12 keV, where Y_2O_3 has similar XANES features.

The spectrum for the extracted NOs again shows very broad features that are more consistent with the Y_2TiO_5 phase. Further, the features observed in the XANES Y edge for the extracted NOs are consistent with the Ti edge data and a disordered atomic environment.

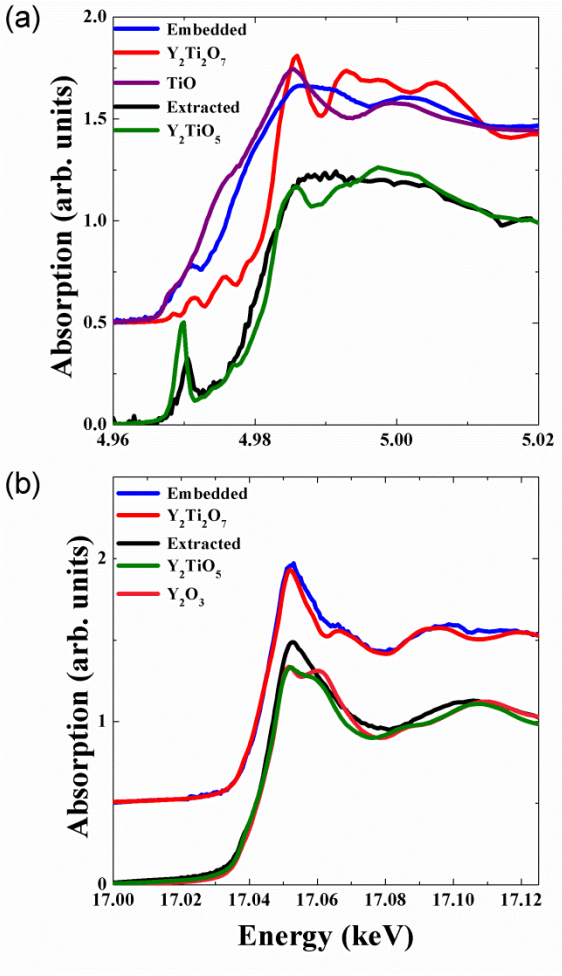

Figure 3.2 – XANES spectra at the K-edge for (a) Ti and (b) Y for the embedded and extracted measurements. The TiO, Y_2O_3, Y_2TiO_5 and $Y_2Ti_2O_7$ bulk standards are shown for reference.

3.5 EXAFS Results

The EXAFS spectra, $k^2\chi$ ($Å^{-2}$), and the magnitude of the Fourier Transformed spectra, $|\chi(R)|$ ($Å^{-3}$), for the Ti *K*-edge are shown in Figure 3.3a and Figure 3.3b, respectively, and for the Y K-edge in Figure 3.3c and Figure 3.3d, respectively. The

different spectral features (oscillations in the $k^2\chi$ and peaks in the $|\chi(R)|$) result from single and multiple scattering from atoms around the absorbing atom of interest. The Ti *K*-edge EXAFS data for the as-received MA957 (embedded) is complex, with multiple environments giving rise to the observed fine structure. For example, the first peak at ~1.5 Å in the embedded spectrum is attributed to Ti-O bonds. The large intensity is indicative of multiple environments or bulk like structure. The second peak at ~2.5 Å is similar in position to the metallic Ti in solution. These features are consistent with previous studies where multiple Ti environments were also observed [18]. The extracted EXAFS show significantly less structure at the Ti edge, with a small peak at about 1.25 Å, but overall weak signal beyond ~2 Å.

The Y *K*-edge EXAFS spectra (Figure 3.3d) show that atomic environments for the embedded NOs are complex with bond lengths of ~1.6, 2.4 and 3.4 Å, similar to a mixture of the $Y_2Ti_2O_7$, Y_2O_3 and Y_2TiO_5. The extracted NOs again have a different structure, more closely resembling that of the Y_2TiO_5 and Y_2O_3 phases. The heights of the first peaks are, however, much lower in intensity compared to the standards potentially due to larger structural disorder and relatively small NO sizes.

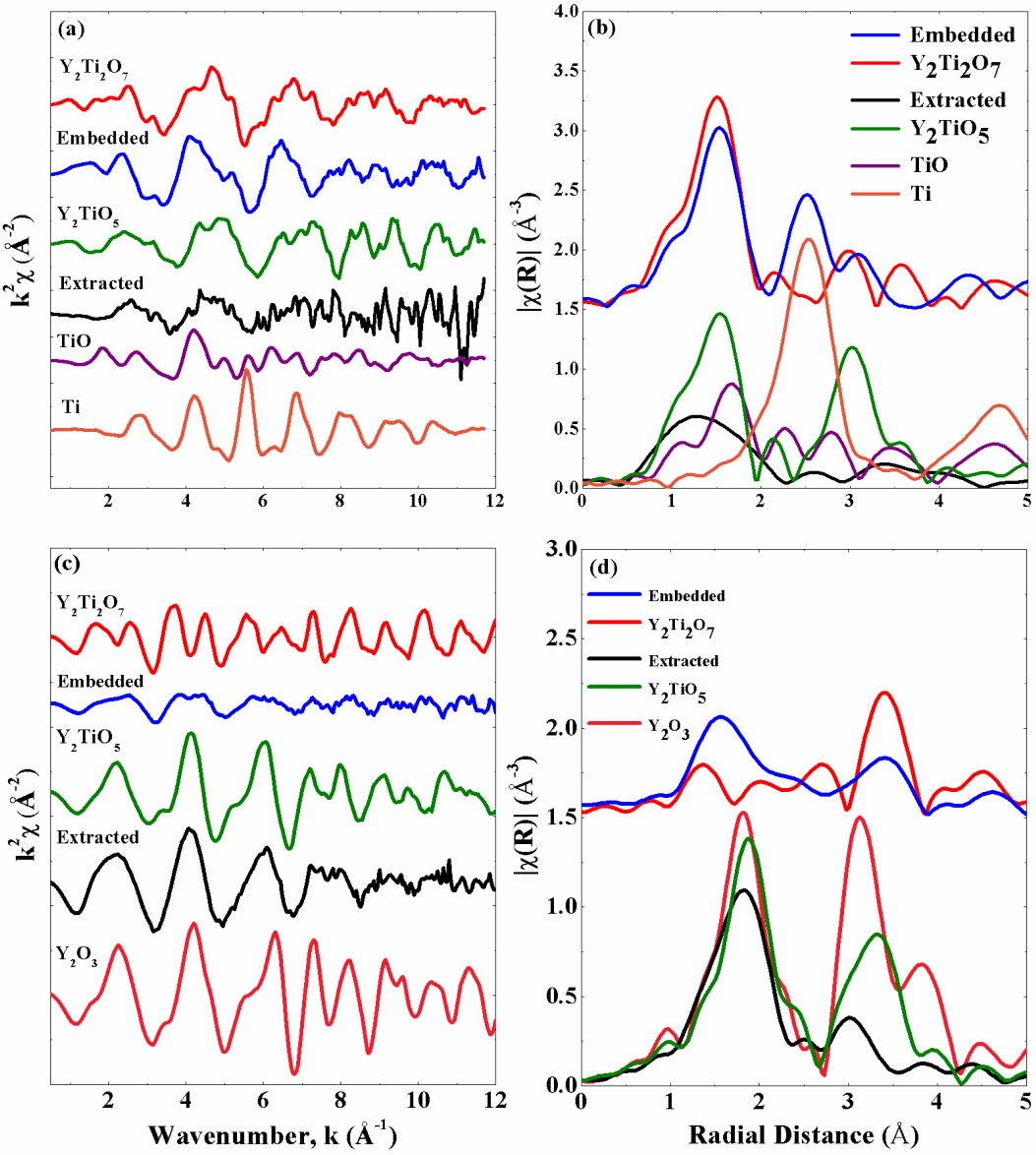

Figure 3.3 – EXAFS spectra $k^2\chi$ (Å^{-2}) and the magnitude of the Fourier Transformed spectra, $|\chi(R)|$ (Å^{-3}), for the Ti K-edge are shown in (a) and (b), respectively, and for the Y K-edge in (c) and (d), respectively

3.6 Quantitative Results

Table 3.1 shows the coordination number ratios (CN_{NO}/CN_S), differences in bond length (BL_{NO}-BL_S), differences in Debye – Waller factor (σ^2_{NO}-σ^2_S), and differences in asymmetry parameter (C_{3NO}-C_{3S}) between the nano-oxide and the standards. For each type of sample (embedded or extracted) and each edge (Ti or Y), the spectrum was analyzed relative to the two standards that most resemble the observed spectral features from the XANES. For example, the Ti edge of the embedded spectrum most resembles the $Y_2Ti_2O_7$ and Y_2TiO_5 standards. Note that the embedded spectra have multiple Ti and Y environments and overlapping first nearest neighbor distances. Thus, the values for the embedded samples are an average of the multiple environments.

The Ti edge for the as-received MA957 (embedded) case have coordination number ratios close to 1. This value is considered large for nano-sized particles, and is likely due to the overlapping environments of the oxide phases. The changes in the Ti-O bond length (BL) were smaller for the $Y_2Ti_2O_7$ phase than the Y_2TiO_5 phase, consistent with the previous discussion.

The quantitative analysis of the embedded case at the Y edge indicates a mixture of the Y_2O_3 and $Y_2Ti_2O_7$ phases. However, the multiple overlapping environments hinder a full quantitative description of the structural parameters for both Ti and Y edges. As noted previously, the log-ratio method requires spectrally isolated nearest neighbor atoms.

The Ti *K*-edge quantitative results for the extracted NOs show a lower CN compared to the Y_2TiO_5 and TiO standards. An increase in the σ^2, slight bond length

expansion and increase in asymmetry are also observed. The extracted NO structural parameters at the Y edge show similar trends, with a decrease in the coordination number, subtle changes in bond length and increase in σ^2. A decrease in CN and increase in the σ^2 are commonly observed in nanoparticle systems due to finite-size effects and large surface to volume ratios. These specifically include an increase in the number of under coordinated surface atoms and relaxation/reconstruction of surface atoms away from their ideal positions. Additionally, the C_3 is a measure of the asymmetric deviation from a Gaussian interatomic distance distribution and a positive value indicates that the BL distribution is skewed toward longer bond lengths. The positive ΔC_3 values for the extracted NO are potentially the result of surface atoms reconstructing away from the particle core. The results at both edges again indicate that the extracted NOs have a structure similar to Y_2TiO_5 phase (albeit with slightly different CN, BL and σ^2 due to finite size effects). All the structural changes in the extracted NO sample are consistent with the atomic environment commonly observed for other nanoparticle systems, where an increase in the surface-to-volume ratio results in an under-coordinated (low and reconstructed surface [25,26].

Table 3.1 – Quantitative results from the EXAFS fitting indicating coordination number (CN_{NO}/CNs), bond length (ΔBL), Debye – Waller factor ($\Delta\sigma^2$) and asymmetry parameter (ΔC_3). The subscripts NO and S are for nano-oxide and standard, respectively. *The embedded sample has multiple Ti and Y environments, and overlapping first nearest neighbour distances. Thus, values are an average of the multiple environments.

Nano-oxide	**Edge**	**Standard**	**CN_{NO}/CN_S**	**$BL_{NO} - BL_S$ (Å)**	**$\sigma^2_{NO} - \sigma^2_S$ ($x10^{-3}$ Å^2)**	**$C_{3NO} - C_{3S}$ ($x10^{-4}$ Å^3)**
Embedded*	Ti	$Y_2Ti_2O_7$	0.96 (0.07)	0.0924 (0.001)	3.69 (0.13)	3.7 (0.3)
Embedded*	Ti	Y_2TiO_5	1.10 (0.05)	0.156 (0.001)	3.56 (0.13)	11.8 (0.2)
Embedded*	Y	Y_2TiO_5	0.64 (0.02)	0.058 (0.002)	4.74 (0.62)	34.8 (0.4)
Embedded*	Y	Y_2O_3	0.65 (0.03)	0.083 (0.001)	5.42 (0.7)	31.8 (0.3)
Extracted	Ti	Y_2TiO_5	0.55 (0.04)	0.039 (0.003)	2.93 (0.047)	15.4 (0.6)
Extracted	Ti	TiO	0.60 (0.03)	0.076 (0.002)	2.46 (0.037)	13.1 (0.4)
Extracted	Y	Y_2TiO_5	0.87 (0.07)	-0.005 (0.001)	4.82 (0.36)	2.7 (0.2)
Extracted	Y	Y_2O_3	0.84 (0.06)	0.037 (0.001)	8.05 (0.29)	2.9 (0.2)

3.7 Discussion

The Ti and Y *K*-edge environments were probed in both MA957 containing embedded NOs, and in filters containing extracted NOs. The broad first peak in the embedded case indicates that Ti is in multiple environments which include $Y_2Ti_2O_7$, Y_2TiO_5, TiO, and metallic matrix Ti. Further, the Y spectrum is most consistent with $Y_2Ti_2O_7$ and Y_2O_3. The Y_2TiO_5 component of the Y-edge was nearly undetectable.

The bulk extraction and selective filtration procedure successfully captured the larger Y_2TiO_5 particles (and perhaps others), and allowed a more discriminating analysis. The larger particles were trapped in the filters during extraction, while the smaller ones passed through. The Ti-edge spectrum from the extracted NOs had a pre-edge feature very

similar to Y_2TiO_5. Further, the Y-edge features closely resemble those of Y_2TiO_5 and Y_2O_3.

The use of the log-ratio method in this study, to quantify changes in NN bonding (Ti-O and Y-O bonds), is quite advantageous. The NN peaks for the extracted NOs are well isolated (no multiple scattering paths overlap) and correspond to common metal-oxygen bonds. Thus, quantitative analysis yields information on the structural state of the NOs relative to the bulk standards. Another advantage is that the log-ratio method does not assume any structure, thus the scattering amplitudes and phase shifts are not needed prior to analysis [27]. The combination of the qualitative XANES and quantitative EXAFS results clearly demonstrate that the extraction process is capable of isolating a minor component that is essentially overwhelmed by the large and complex environment observed when the NOs are embedded in a matrix.

The authors are aware that the extraction process may affect the character of the NOs. For example, possible segregation of Ti, O, and Cr to NO interfaces cannot be observed by XAS since the matrix is dissolved during particle extraction. Further, the extracted NOs may partially restructure when they are released from the matrix. However, such extraction effects are not believed to be significant with respect to the core NOs, especially since they generally resemble those seen in TEM observations [8].

3.8 Conclusions

In conclusion, the chemistries and structures of NOs in NFA MA957 were characterized by XAS for both embedded and extracted precipitates. The log-ratio method was used to successfully analyze the spectra and provide structural parameters relative to the known standards. Measurements on embedded NOs in bulk MA957 are most consistent with $Y_2Ti_2O_7$, while the slightly larger extracted oxides are primarily consistent with Y_2TiO_5. Analysis of the as-received MA957 was difficult due to the multiple Ti environments including $Y_2Ti_2O_7$, Y_2TiO_5, TiO, and dissolved metallic Ti. The bulk extraction and selective filtration technique successfully removed the matrix, trapped the larger Y_2TiO_5 particles, and yielded samples well suited for XAS measurements. The smaller $Y_2Ti_2O_7$ oxides passed through the filters but were the predominant embedded phase. This will be further confirmed in the future by XAS measurements on the residues in the filter effluent. The described methods and analysis are an important complement to the other characterization techniques that have been applied to NFAs, a remarkable alloy system of rapidly growing worldwide interest, especially for advanced fission and fusion energy applications.

3.9 Acknowledgements

I would like to thank I. Charit (UI) for providing part of the MA957 material, A. Ofan (BNL) for XAS measurements on MA957, B. Ravel (BNL) for help with the XAS

data acquisition on filters, D. Sprouster (BNL) for the data analysis, and L. Ecker (BNL) and G.R. Odette (UCSB) for guidance and support.

3.10 References

[1] T. Stan, D.J. Sprouster, A. Ofan, G.R. Odette, L.E. Ecker, I. Charit, J. Alloys Compd. 699 (2017) 1030–1035.

[2] N.J. Cunningham, Y. Wu, A. Etienne, E.M. Haney, G.R. Odette, E. Stergar, D.T. Hoelzer, Y.D. Kim, B.D. Wirth, S.A. Maloy, J. Nucl. Mater. 444 (2014) 35–38.

[3] E.A. Marquis, Appl. Phys. Lett. 93 (2008) 10–13.

[4] C.A. Williams, P. Unifantowicz, N. Baluc, G.D.W. Smith, E.A. Marquis, Acta Mater. 61 (2013) 2219–2235.

[5] D.J. Larson, P.J. Maziasz, I.S. Kim, K. Miyahara, Scr. Mater. 44 (2001) 359–364.

[6] M.K. Miller, E.A. Kenik, K.F. Russell, L. Heatherly, D.T. Hoelzer, P.J. Maziasz, Mater. Sci. Eng. A 353 (2003) 140–145.

[7] Y. Wu, J. Ciston, S. Kräemer, N. Bailey, G.R. Odette, P. Hosemann, Acta Mater. 111 (2016) 108–115.

[8] Y. Wu, E.M. Haney, N.J. Cunningham, G.R. Odette, Acta Mater. 60 (2012) 3456–3468.

[9] J. Ribis, E. Bordas, P. Trocellier, Y. Serruys, Y. de Carlan, A. Legris, J. Mater. Res. 30 (2015) 2210–2221.

[10] S.Y. Zhong, J. Ribis, N. Lochet, Y. de Carlan, V. Klosek, M.H. Mathon, J. Nucl.

Mater. 455 (2014) 618–623.

[11] J. Ribis, Y. De Carlan, Acta Mater. 60 (2012) 238–252.

[12] V. Badjeck, M.G. Walls, L. Chaffron, J. Malaplate, K. March, J. Nucl. Mater. 456 (2015) 292–301.

[13] K. Dawson, G.J. Tatlock, J. Nucl. Mater. 444 (2014) 252–260.

[14] M. Ohnuma, J. Suzuki, S. Ohtsuka, S.-W. Kim, T. Kaito, M. Inoue, H. Kitazawa, Acta Mater. 57 (2009) 5571–5581.

[15] M. Dumont, L. Commin, I. Morfin, F. DeGeuser, F. Legendre, P. Maugis, Mater. Charact. 87 (2014) 138–142.

[16] N.J. Cunningham, Thesis Univeristy Calif. St. Barbar. (2012).

[17] M.J. Alinger, G.R. Odette, D.T. Hoelzer, Acta Mater. 57 (2009) 392–406.

[18] S. Liu, G.R. Odette, C.U. Segre, J. Nucl. Mater. 445 (2014) 50–56.

[19] J.J. Fischer, Dispersion Strengthened Ferritic Alloy for Use in Liquid-Metal Fast Breeder Reactors (LMFBRS), 1978.

[20] B. Ravel, M. Newville, J. Synchrotron Radiat. 12 (2005) 537–541.

[21] G. Bunker, Nucl. Instruments Methods Phys. Res. 207 (1983) 437–444.

[22] P. Fornasini, S. a Beccara, G. Dalba, R. Grisenti, A. Sanson, M. Vaccari, F. Rocca, Phys. Rev. B 70 (2004) 174301.

[23] L.A. Grunes, Phys. Rev. B 27 (1983) 2111–2131.

[24] F. Farges, G.E. Brown, J.J. Rehr, Phys. Rev. B 56 (1997) 1809–1819.

[25] L.L. Araujo, R. Giulian, D.J. Sprouster, C.S. Schnohr, D.J. Llewellyn, P. Kluth, D.J.

Cookson, G.J. Foran, M.C. Ridgway, Phys. Rev. B 78 (2008) 94112.

[26] A.I. Frenkel, C.W. Hills, R.G. Nuzzo, J. Phys. Chem. B 105 (2001) 12689–12703.

[27] C.S. Schnohr, M.C.R. Editors, Springer Series in Optical Sciences 190 X-Ray Absorption Spectroscopy of Semiconductors, Springer, 2015.

Chapter 4 Annealed and He Implanted NFAs

4.1 Introduction

Fusion reactors will require advanced materials with tolerance to intense high-energy neutron fluxes that generate helium (He) concentrations reaching thousands of atomic parts per million and hundreds of atomic displacements per atom over the operating lifetime. Neutron irradiation along with other synergistic effects can lead to void swelling, embrittlement and irradiation creep [1–3]. Managing transmutation-produced helium is a grand challenge for turning the promise of C-free fusion power into a reality. Nanostructured ferritic alloys (NFAs) are promising candidate structural materials, which are dispersion strengthened by an ultrahigh density of order $\approx 5x10^{23}/m^3$ of Y-Ti-O nano-oxides (NOs) averaging ≈ 2.5 nm in diameter, with volume fractions of order 0.5% [1–3]. NOs, significantly, trap otherwise highly damaging helium in harmless nm-scale interface bubbles [1–3]. Preventing the formation of larger bubbles allows NFAs to manage very high concentrations He produced in fusion reactors. Understanding the characteristics of the NO-bubble association is important to developing, qualifying and optimizing NFAs.

Very small NOs and bubbles (<2 nm), are difficult to image simultaneously using conventional transmission electron microscopy (TEM) techniques. Thus, to facilitate characterization, a 14YWT-NFA alloy was annealed to coarsen the NOs, prior to He

implanted to form bubbles. The resulting microstructures were analyzed using bright field TEM and high resolution scanning transmission electron microscopy (STEM). A schematic of the general approach taken in this study. The alloy was first annealed to coarsen the NOs, then He implanted to nucleate bubbles.

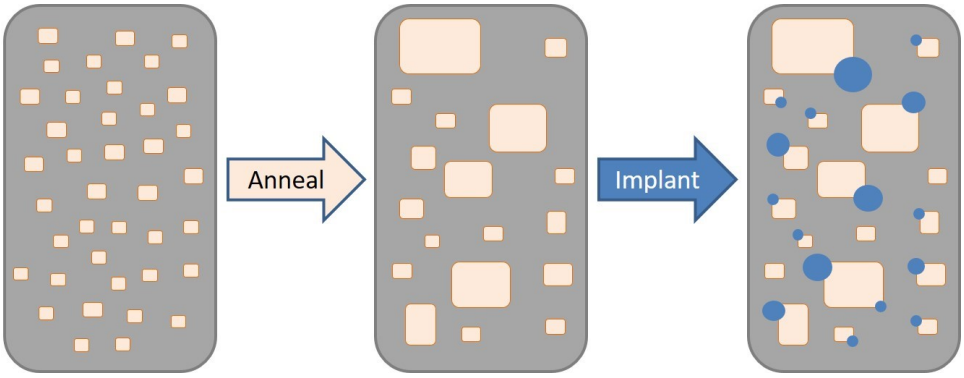

Figure 4.1 – Schematic of the general approach taken in this study. A 14YWT NFA containing ~ 2 nm NOs was first annealed to coarsen the NOs, then implanted with He to nucleate bubbles.

4.2 Experimental

A coupon of NFA-14YWT (V540H) was annealed at 1200 °C for 8.2×10^5 seconds (228 hrs) in vacuum. 1 MeV He^+ ions were implanted at the Kyoto University DuET facility in Japan at 700°C at a dose rate of 1.2×10^{12} He/cm^2/s. A spinning degrader foil was used to spread the He implantation profile, which is shown as a red solid curve in Figure 4.2. TEM examinations were carried out over the full ≈ 1.5 μm implanted region. The peak He concentration is 4100 appm at a depth of ~ 1.2 μm.

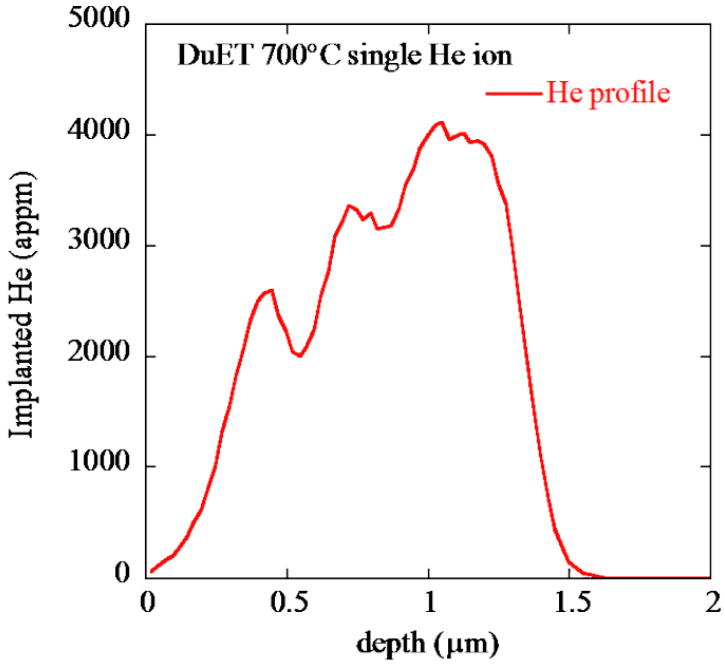

Figure 4.2 – SRIM simulation of the He implantation profile.

Electron backscatter diffraction (EBSD) was carried out on an FEI Quanta 400F field-emission scanning electron microscope (SEM). Four TEM lift-outs were fabricated using a FEI HELIOS Focused Ion Beam (FIB) tool. A 2 kV, 5.5 pA low energy ion beam was used to clean the lift-out and remove residual gallium damage. Preliminary TEM characterization was done on a 300 keV FEI Titan at UCSB to check the lift-out orientations and thicknesses. Foils were then imaged using the TEAM 1 aberration corrected TEM at LBNL in both high resolution TEM and high resolution STEM modes. The lattice spacings and inter-planar angles were measured using ImageJ.

4.3 SEM and EBSD Characterization

Figure 4.3 shows EBSD data form the 14YWT alloy. The band contrast image in Figure 4.3a shows the wide variation in grain sizes from <0.5 μm to >30 μm. The inverse pole figure z-direction map in Figure 4.3b is colored according to the out-of-plane crystallographic orientation of the grain. For example, a green grain indicates {110} type surface orientations. EBSD was used to identify grains with a <100> zone axis used for TEM. Further, since the implantation depth of interest is ~ 1.2 μm, grains of similar or slightly larger size were studied.

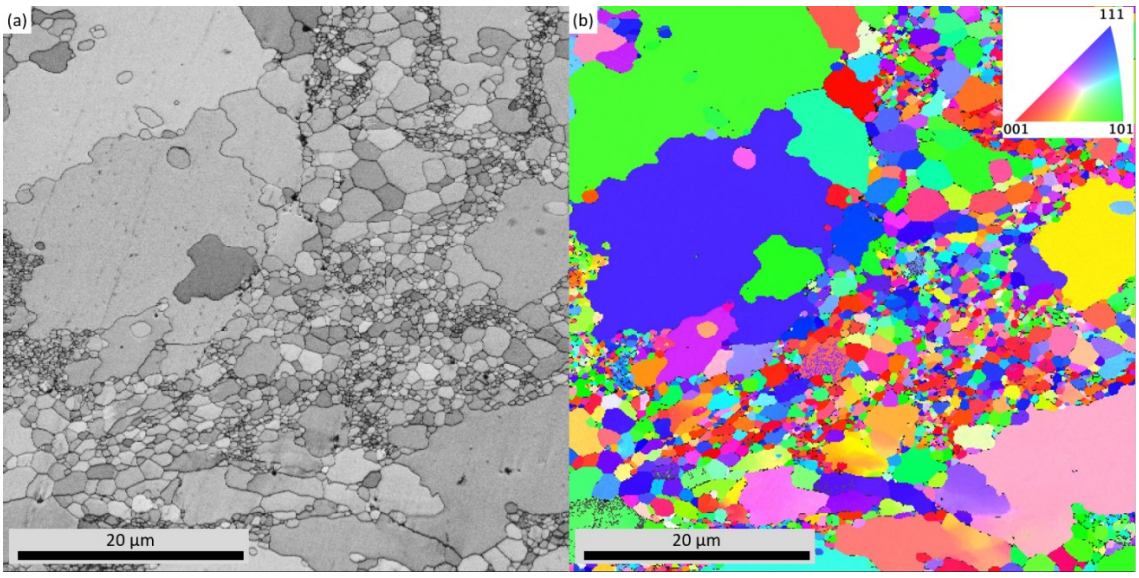

Figure 4.3 – (a) EBSD band contrast and (b) inverse pole figure z-direction maps from the surface of a 14YWT alloy.

4.4 TEM Characterization

Figure 4.4a shows a cross-sectional view of the 14YWT alloy. The large 2.5 x 2.8 µm grain is viewed through the <100> zone axis and appears dark. He was implanted through the top surface, as indicated by the yellow arrow, to a maximum depth of ~ 1.5 µm. Figure 4.4b is a higher magnification under-focused bright field TEM image from a 200 x 180 nm region just below the grain surface where the expected He concentration is <250 appm. In the under-focused condition, the cuboidal NOs have a black outline and bubbles appear as white circles. Most bubbles in this region have a diameter of d ≈ 3.5 nm, and are found at the corners of cuboidal precipitates (black arrows in Figure 4.4b). This result is significant because it indicates that the preferred bubble nucleation site on NOs is at the corners. Smaller d < 2 nm bubbles may also exist in the area, but could not be imaged due to limitations of the microscope and interfering signals from other features.

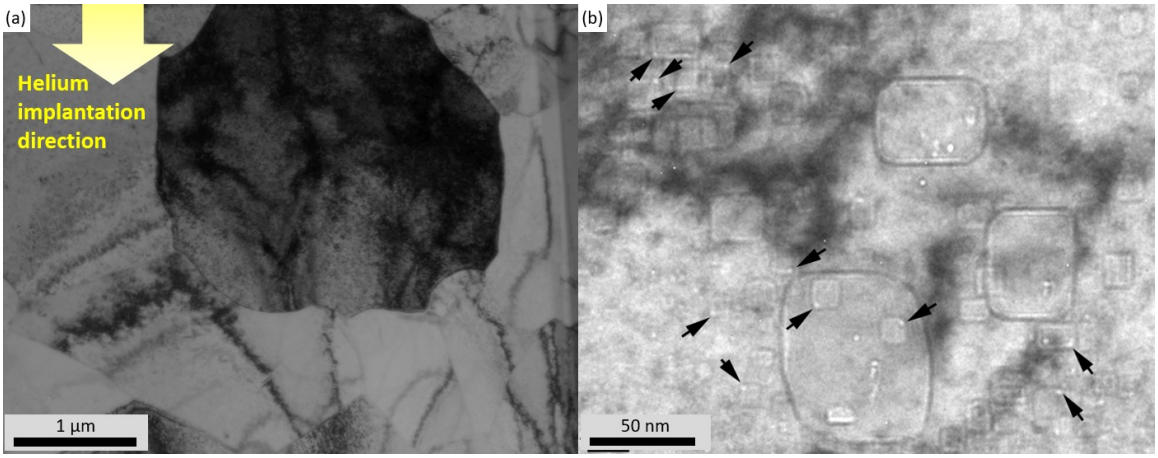

Figure 4.4 – (a) Low magnification bright field TEM image of a large grain for a <100> zone axis. (b) An under-focused bright field TEM image from the top of the dark grain in

(a) showing faceted NOs. Black arrows indicate the location of bubbles, most of which reside on NO corners.

The HRSTEM image in Figure 4.5a was taken using the TEAM 1 aberration corrected TEM at LBNL. Figure 4.5b shows the same image as Figure 4.5a, but some of the NOs have been outlined in yellow, and bubbles in blue. The images show cuboidal NOs (medium intensity) and attached bubbles (dark contrast). Two crystallographic orientation relationships (ORs) with the matrix were identified. The 7.1 nm NO has a cube-on-cube OR {100}Fe//{100}NO with <100>Fe\\<100>NO. The 6.1 nm NO has a cube-on-edge OR {100}Fe//{110}NO with <100>Fe//<100>NO. The plot in Figure 4.5c shows the correlation between bubble size and NO size. The red trend line has a positive slope indicating that larger NOs have larger bubbles attached to them. On average, the bubble size is ~ 75% of the NO size.

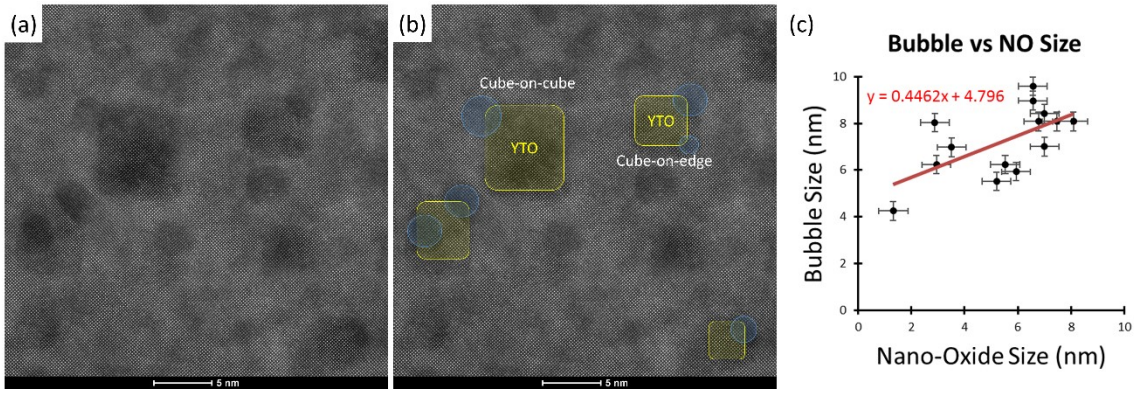

Figure 4.5 – (a) Raw HRSTEM image of an area near the peak He implanted region showing NOs and attached bubbles. (b) The same image as (a), but NOs are outlined in yellow, and bubbles are marked with blue. (c) Plot showing the positive correlation between bubble size and NO size.

Table 4.1 summarizes the characteristics from some of the NOs and bubbles observed in this study, including those from Figure 4.5. Larger NOs have larger bubbles, and some of the largest NOs (>6 nm) have two bubbles.

Table 4.1 – Summary of NOs and bubbles observed in this study.

NO index	NO size (nm)	Orientation Relationship	# of bubbles attached to the NO	Bubble diameter (nm)
1	8.0	Cube-on-edge	2	2.6
2	6.2	Cube-on-cube	2	2.4
3	7.0	Not available	2	3.25
4	2.8	Not available	1	1.4
5	3.3	Not available	1	1.7
6	4.7	Not available	1	1.3
7	4.2	Not available	1	1.4

Figure 4.6a and Figure 4.6c are HRSTEM images showing two 3 – 5 nm NOs associated with 1 – 2 nm bubbles (dark contrast). Figure 4.6b is a processed image of Figure 4.6a, more clearly showing the location of atomic columns. The black arrow indicates the location of a dislocation near the bubble-NO interface. The NO in Figure 4.6c has the $Y_2Ti_2O_7$ pyrochlore structure, and a cube-on-edge orientation relationship with the matrix. This OR was previously seen by Wu et al. [4]. The dark areas indicate the presence of bubbles, which are found at NO the corners. Figure 4.6d and Figure 4.6e are inverse Fast Fourier Transformed (FFT) images of the NO in Figure 4.6c, and were obtained by isolating {400} and {440} reflections, respectively. The inverse FFT analysis reveals dislocations along the NO – matrix interfaces, some of which are marked with white

arrows. The atomic lattice mismatch between the $Y_2Ti_2O_7$ NO and the matrix leads to interfacial misfit dislocations, shown with white arrows in Figure 4.6d and Figure 4.6e.

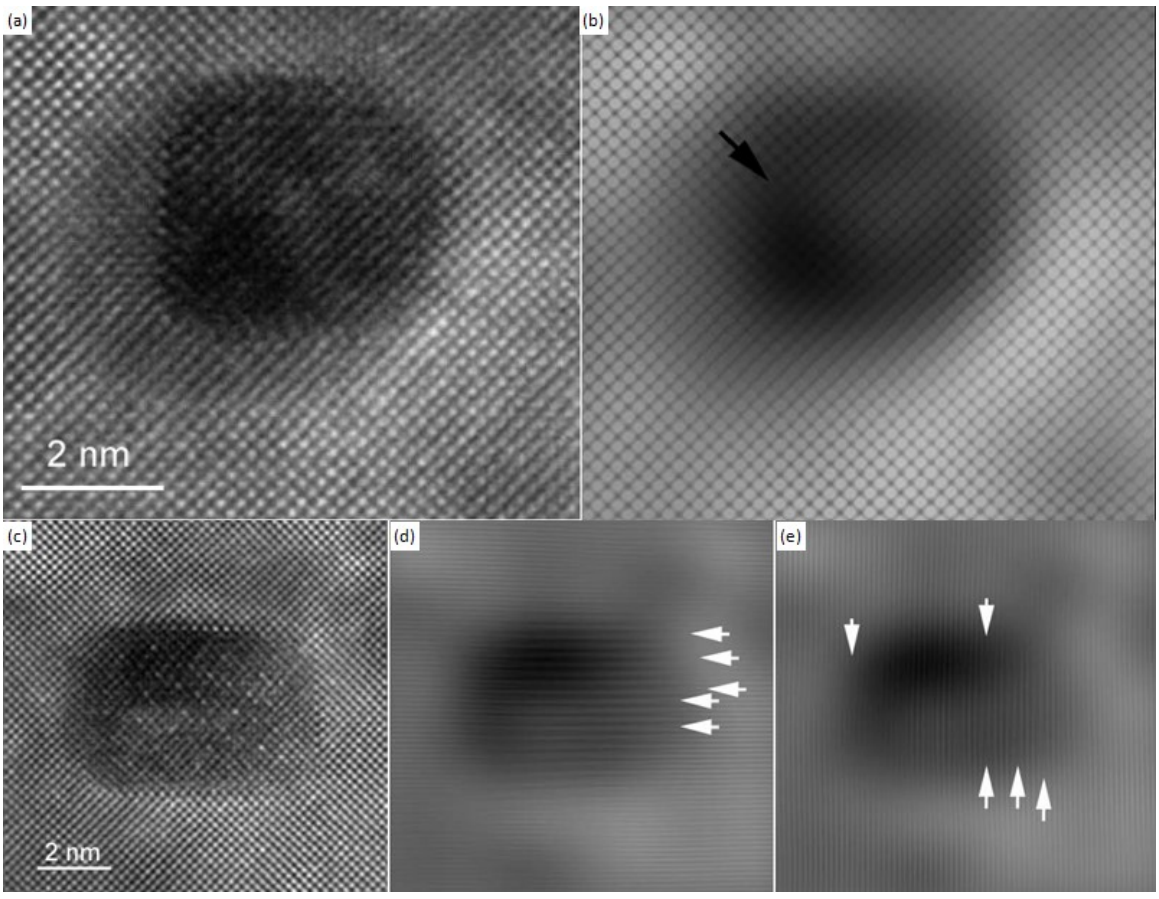

Figure 4.6 – (a) and (c) HRSTEM images of 3 – 5 nm NOs and 1 – 2 nm bubbles (dark contrast). (b) Processed image of the NO in part (a) showing the location of a misfit dislocation near the NO – bubble interface. Inverse FFT images of the NO in (c) are shown for the (d) {400} and (e) {440} reflections. White arrows indicate the location of misfit dislocations.

Figure 4.7a shows a raw HRSTEM image of a NO and two bubbles which were selected for in-depth analysis. Figure 4.7b shows the NO outline in yellow dashed lines,

and the bubbles in blue. The faceted NO is 3.5 x 5.9 nm, and has two bubbles with d = 2.6 nm and 1.3 nm. A 3D rendering of the NO and bubbles is shown in Figure 4.7c. FFT analysis indicates that the NO has the $Y_2Ti_2O_7$ pyrochlore structure, a cube-on-edge OR with the matrix, and is viewed through the <110>$Y_2Ti_2O_7$ zone axis. The 3D rendering in Figure 4.7d shows the many faces, edges, and corners of the polyhedral $Y_2Ti_2O_7$ precipitate as viewed edge-on. The largest facets are {100} cube faces, followed by {111} corners, while the {110} edges are the smallest. The size of each facet is indicated in Figure 4.7b.

The matrix-oxide interfacial ORs were obtained by indexing the NO surfaces, and are shown Figure 4.7e. The top and bottom interfaces have the rotated cube-on-cube OR: {100}Fe//{100}NO with <100>Fe//<100>NO. The cuboidal NO has six faces, but the two on the top and bottom have a different OR than the other four. Two of the four faces are labeled with {100} face in Figure 4.7d, and have an edge on cube OR: {110}Fe//{100}NO with <100>Fe//<100>NO. The side interfaces have a cube-on-edge OR: {100}Fe//{110}NO with <100>Fe//<100>NO. And the diagonal OR is edge-on-corner: {110}Fe//{111}NO with <100>Fe//<110>NO. Notably, this OR is also found for thin film Fe deposition on {111} $Y_2Ti_2O_7$ single crystal substrates [5]. Clearly, by comparing Figure 4.7c with Figure 4.7e, the smaller bubble is attached to the {111} NO facet, while the larger bubble is centered on the {111}NO facet, but has grown to the point where it is is wetting the surrounding NO facets. Finally, Figure 4.7f is an inverse FFT image where black arrows indicate dislocation cores. The dislocations are on {111} NO planes and near

the bubbles. Thus, bubbles likely nucleate at dislocations on {111} NO surfaces, then grow and envelop other NO facets.

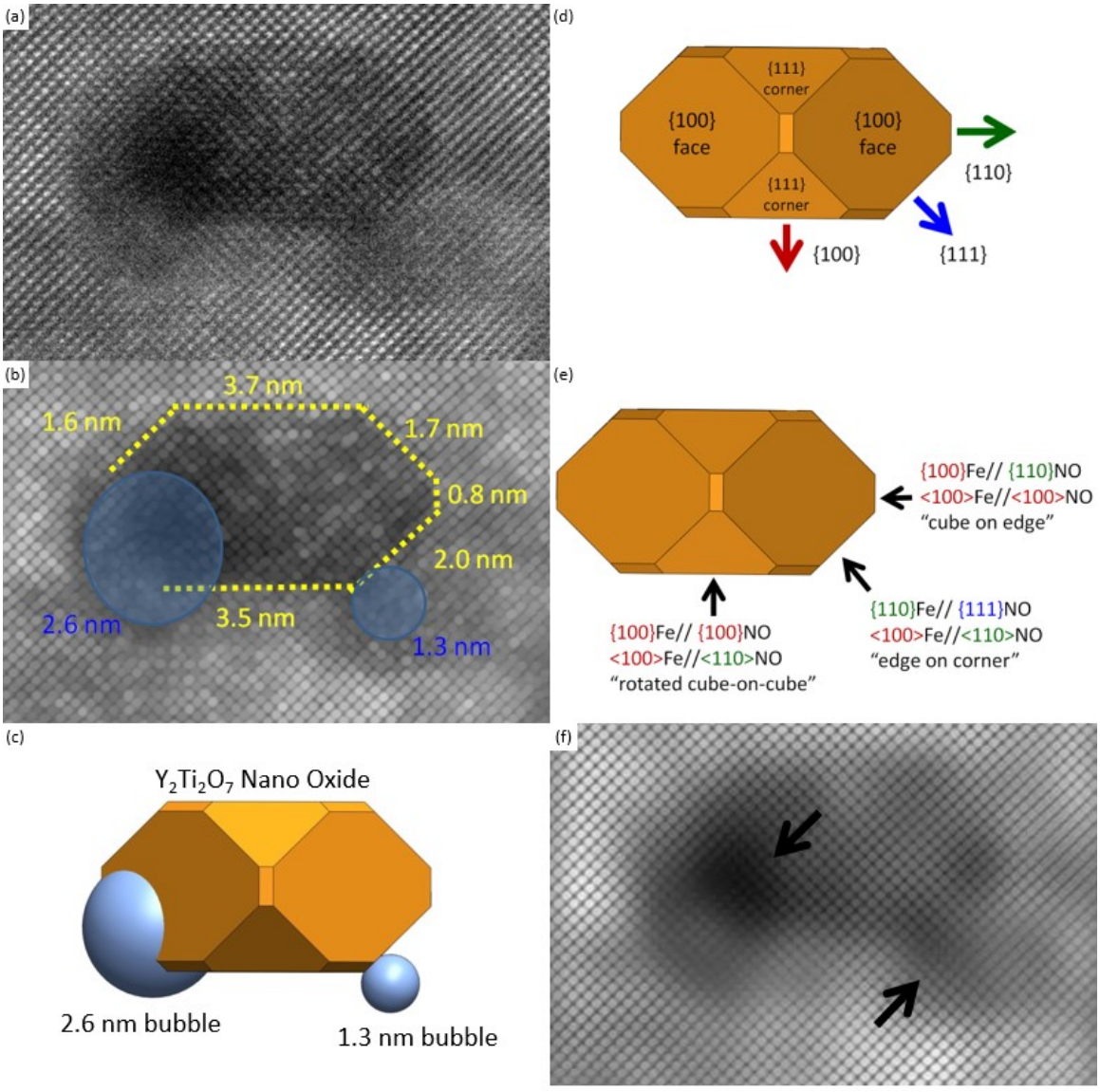

Figure 4.7 – (a) Raw HRSTEM image. (b) Processed image outlining a NO with yellow dashed lines, and two bubbles. (c) 3D rendering of the NO and bubbles. (e) Indexed NO surfaces and (f) the interfacial orientation relationships with the matrix. (f) Inverse FFT images indicating dislocations near the bubble – NO interfaces.

4.5 Summary

To further the understanding of the interaction between helium and nano-oxides (NOs) in nanostructured ferritic alloys (NFAs), a 14YWT alloy was annealed to coarsen the NOs, and He implanted to produce bubbles. High resolution transmission electron microscopy shows two dominant orientation relationships (cube-on-edge and cube-on-cube). The smaller NOs are associated with smaller bubbles, while some of the largest NOs (>6 nm) often have two bubbles. Most bubbles nucleate at {111} NO facets. Future studies include further TEM observation using the TEAM-1 aberration corrected TEM at LBNL, and electron energy loss spectroscopy (EELS) measurements on bubbles to obtain He densities.

4.6 Acknowledgements

I would like to thank N. Cunningham (UCSB) for annealing the MA957, T. Yamamoto (UCSB) for the DuET He implantation, Y. Wu (UCSB) for the low magnification TEM, J. Ciston for the aberration corrected TEM (LBNL), and G.R. Odette (UCSB) for guidance and support.

4.7 References

[1] G.R. Odette, M.J. Alinger, B.D. Wirth, Annu. Rev. Mater. Res. 38 (2008) 471–503.

[2] G.R. Odette, JOM 66 (2014) 2427.

[3] Y. Dai, G.R. Odette, T. Yamamoto, The Effects of Helium in Irradiated Structural Alloys, 1st ed., Elsevier Inc., 2012.

[4] Y. Wu, J. Ciston, S. Kräemer, N. Bailey, G.R. Odette, P. Hosemann, Acta Mater. 111 (2016) 108–115.

[5] T. Stan, Y. Wu, G.R. Odette, K.E. Sickafus, H.A. Dabkowska, B.D. Gaulin, Metall. Mater. Trans. A Phys. Metall. Mater. Sci. 44 (2013) 4505–4512.

Chapter 5 Fe – {111}YTO Bilayers

5.1 Introduction

This chapter has been published in Metallurgical and Materials Transactions A [1]. In nanostructured ferritic alloys (NFAs), the interfaces between the ferritic matrix and nano-oxides (NOs) trap He in fine bubbles and pin dislocations [2,3]. However, the details of important mechanisms and processes, such as helium trapping and thermal stability, are not well understood. The objective of this work is to fabricate and characterize Fe-$Y_2Ti_2O_7$ mesoscopic-scale interfaces with self-selected orientation relationships (ORs) by Fe deposition on $Y_2Ti_2O_7$ (YTO) single crystal substrates. While they may differ from those for embedded NOs, the study of these mesoscopic surrogates will facilitate developing a fundamental understanding of the metal-oxide interfaces in NFA, especially with respect to their structures and functional properties.

5.2 Experimental

A pure single crystal of YTO was acquired from McMaster University. The crystal was grown in a two-mirror NEC floating zone image furnace. The starting materials for the polycrystalline rods were 99.999% pure Y_2O_3 and 99.995% pure TiO_2, both from Alfa Aesar. The feed rods were synthesized following Gardner et al. [4]. The final single crystal

was grown using the floating zone technique at 5 mm/hr in air [5]. A 1.8 mm thick wafer was cut to serve as a substrate for the experiment. X-ray diffraction (XRD) measurements indicate that the crystal was miscut ≈ 5º from the {111}YTO orientation. An Allied Multiprep instrument was used to polish the wafer using a sequence of 15 (for flattening), 9, 6, 3, 1, 0.5 and 0.1 μm papers for 10 minutes each at 75 rpm. The final 15 minute polishing step used a 0.02 μm colloidal silica suspension. Atomic force microscopy (AFM) scans indicated that the YTO crystal had an average surface roughness of ≈ 1 nm.

An electron beam system was used to deposit Fe on the YTO crystal wafer substrate and on a pyrex glass substrate. The substrates were held in place by thin niobium plates, which also helped getter oxygen. The deposition vacuum was $7x10^{-6}$ torr and the substrates were heated to 800 °C. Fe was deposited at a rate of 0.3 nm/s for 600 s, producing a total Fe layer thickness of ≈ 200 nm. The Fe coated substrates were then slowly cooled to room temperature at a rate of ≈ 0.16 °C/s.

A XPERT MPD Thin Film Texture XRD was used to obtain gonio scans and pole figures. A MFP-3D AFM was used to measure the topology of surfaces. An FEI Quanta 400F field-emission environmental scanning electron microscope (SEM) with an electron backscatter diffraction (EBSD) detector was used to obtain the inverse and Euler pole figures and maps. A FEI HELIOS Focused Ion Beam (FIB) tool was used to micro-machine < 30 nm thick electron transparent lift-outs of the interface Fe-YTO interfaces. Platinum was deposited over the Fe for protection, and a low energy gallium beam with 2 KeV 5.5 pÅ was used as a final sample cleaning step. Effects of FIB on microstructure

include amorphization, surface roughness or thickness non-uniformities, induced defects, ion beam and atomic mixing, and alterations due to beam heating [6]. These effects were not observed and were prevented by the protective platinum layer. HRTEM, STEM, and EDX was performed on a 300 keV FEI Titan TEM.

5.3 Fe on Amorphous Pyrex

Fe was first deposited on pyrex glass to determine the naturally preferred Fe orientation on an amorphous substrate. The deposited Fe film is composed by many grains with an average grain size of 0.5 μm and a surface roughness of about 40 nm, as seen in the AFM scan in Figure 5.1a. XRD gonio scans (not shown) indicate that the Fe grains have a {110} out of plane pole orientation. The XRD <100>Fe pole figure (Figure 5.1b) has a radial coordinate χ which ranges from the center ($\chi = 0^{o}$) to the rim of the pole figure ($\chi = 90^{o}$). The polar coordinate φ ranges from 0^{o} to 360^{o}. Figure 5.1b shows a high intensity ring at $\chi = 45^{\circ}$. As expected, there is no in-plane orientation between the Fe crystals and the amorphous pyrex glass.

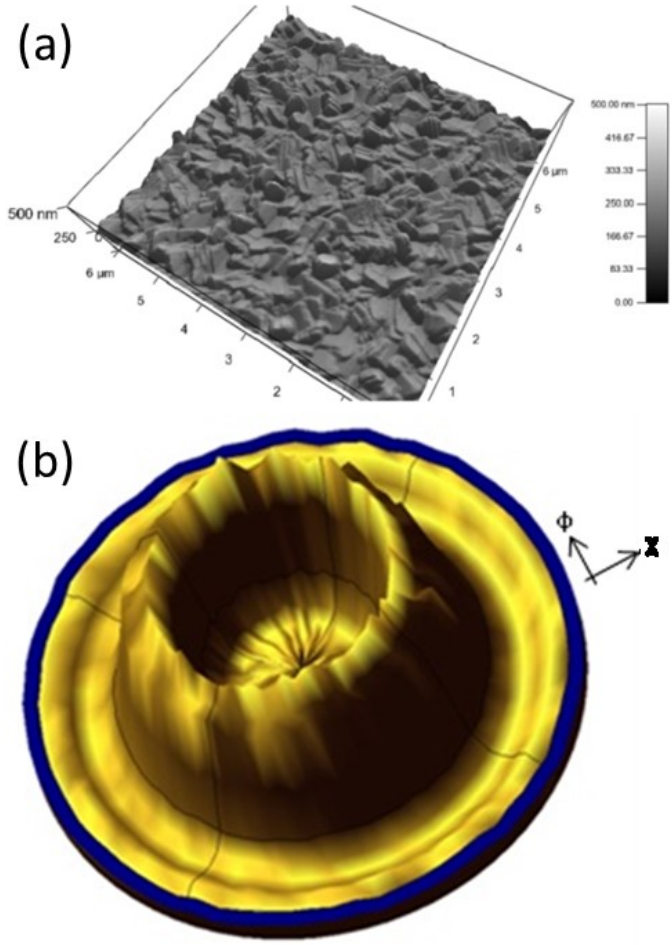

Figure 5.1 – (a) AFM 3D reconstruction of a 6 µm x 6 µm area of Fe grains on amorphous pyrex glass. (b) XRD <100>Fe pole figure showing no in-plane orientation between the Fe grains and the pyrex substrate.

5.4 SEM/EBSD of Fe on {111}YTO

The same conditions used for the amorphous substrate were applied to deposit Fe on the {111}YTO substrate. Figure 5.2a shows the EBSD inverse pole figures (IPFs) from the $Y_2Ti_2O_7$ substrate, which were obtained by scanning an area of the sample which was

not covered with Fe grains. Similar to Figure 5.1b, the IPFs have a radial coordinate χ and a polar coordinate φ. The <100> IPF in Figure 5.2a has three peaks at $\chi = 55^{\circ}$. The <110> IPF has three peaks at $\chi = 35^{\circ}$ and six peaks at the $\chi = 90^{\circ}$ rim. Note that some of the spots at the $\chi = 90^{\circ}$ rim in the <110> IPF are not visible because the SEM probe was aligned with the substrate surface normal, not with the {111}YTO planes. The two IPFs in Figure 5.2a show spots that were expected from a good quality single crystal with a {111} orientation.

Figure 5.2b shows a scanning electron microscopy (SEM) image of Fe grown on the {111}YTO single crystal substrate. The topography of the Fe film is similar to that of the Fe found on the control sample. The Fe grains have an average diameter of ≈ 0.5 μm, similar to those in the control sample. Some grains coalesced and formed larger islands, while others remained as isolated grains. The sample was polished with 0.02 μm colloidal silica for five minutes to improve the surface quality of the EBSD scans. Some silica particles remained embedded on the Fe surface as seen in Figure 5.2b.

The EBSD inverse pole map in Figure 5.2c shows the out of plane crystallographic orientation of the Fe grains in Figure 5.2b. All of the Fe crystallographic surface orientations are assigned an individual color, which is shown in the octant at the top right of Figure 5.2c. Most Fe grains are either {110} oriented (green) or {100} oriented (red). A few grains (yellow) have an orientation between {100} and {110}, and a few grains (light blue/purple) have an orientation between {110} and {111}. There were no {111} oriented grains, and no grains with an orientation between {100} and {111}. The white areas of

Figure 5.2c are places where EBSD could not determine the Fe orientation. This may partly be due to the electron beam hitting the edge of an island grain or hitting a grain-grain boundary. Overlaying Figure 5.2b and Figure 5.2c shows that some {110}Fe grains and some {100}Fe grains remained as isolated islands, while both like and unlike grains frequently coalesced. An EBSD texture analysis of Figure 5.2c shows that ≈ 55% of the grains have a {110} orientation, ≈ 36% of grains have a {100} orientation, and ≈ 9% do not have a clear orientation.

Figure 5.2d shows the same crystallographic information about the Fe grains as Figure 5.2c, but represented as IPFs. The <100> IPF in Figure 5.2d shows a red hot spot at the center indicating that there are many Fe grains with the {100} orientation. The six green spots at $\chi = 45^{o}$ are associated with the {110} textured grains. There are also spots at the rim of the <100> IPF associated with both {110} and {100} textured grains.

The <110> IPF in Figure 5.2d has a green hot spot at the center showing that there are many {110} textured grains. There are twelve red spots at $\chi = 45^{o}$ from the {100} grains, and twelve green spots (in pairs) at $\chi = 60^{o}$ from the {110} grains. There are also spots at the rim of the <100> pole figure from both {110} and {100} textured grains.

The in plane Fe-YTO ORs are obtained by comparing the spots from each Fe pole figure in Figure 5.2d to each YTO pole figure in Figure 5.2a. The only $\chi \neq 0^{o}$ Fe spots that overlap with YTO spots are on the rim of the <100> IPF in Figure 5.2d and on the rim of the <110> IPF in Figure 5.2a. Thus the following Fe to YTO crystallographic ORs are observed:

OR1: {110}Fe//{111}YTO and <100>Fe//<110>YTO

OR2: {100}Fe//{111}YTO and <100>Fe//<110>YTO

Figure 5.2e derives from the same EBSD scan as Figure 5.2c and Figure 5.2d, but shows the orientations of the Fe grains represented as an Euler map. The full crystallographic orientation of each grain is assigned a color that is associated with a series of three rotations around three Euler axis. Note that the pink and powder blue orientations are very similar but have been assigned different colors because they lie close to where the Euler 1 angle loops from 360º to 0º. The crystallographic information from the Euler map is also represented in the Euler pole figures in Figure 5.2f. The colors in the Euler pole figures match the grain colors in the Euler map. Figure 5.2f is used to identify the in plane orientations of the Fe crystals, and to identify the $\chi \neq 0$ peaks from Figure 5.2d.

The <100> Euler pole figure in Figure 5.2f shows a hot spot at the center due to the surface orientation of {100} grains. The {110} grains produce six spots at $\chi = 45^{\circ}$ which come in pairs of two same-color spots, $\varphi = 180^{\circ}$ apart. There is a pair of dark orange spots, a pair of dark green spots, and a pair of pink/powder blue spots. Comparing the <100> Euler pole figure in Figure 5.2f with the <100> IPF in Figure 5.2a shows that the pairs of Fe spots have the same φ angles as the YTO peaks, but at different χ angles. This means that the three in-plane orientations of the {110} grains match the three-fold symmetry of the {111}YTO substrate planes.

The <110> Euler pole figure shows a hot spot at the center due to the surface orientation of {110} grains. As expected, the three in-plane orientations of the {110}

grains give a set of 4 spots at $\chi = 60^{o}$. The {100} grains give twelve spots at $\chi = 45^{o}$ which derive from three sets of four spots, each $\varphi = 90^{o}$ apart. This means that the three in-plane orientations of the {100} grains also match the three-fold symmetry of the {111}YTO substrate planes.

Sketches of the substrate orientation and of the grain orientations are shown in Figure 5.2g. The first sketch shows three {110} cubes which have their <100> directions matched with the three <110> in-plane directions of the substrate. The second sketch shows three {100} oriented cubes with their <100> directions matched with <110>YTO. The colors of the grains in Figure 5.2g match the colors of the grains in the Euler map and in the Euler pole figures. All of the ORs cited above were confirmed using XRD gonio scans and XRD pole figures (not shown). In conclusion, most Fe grains were epitaxially grown on the YTO substrate with two ORs.

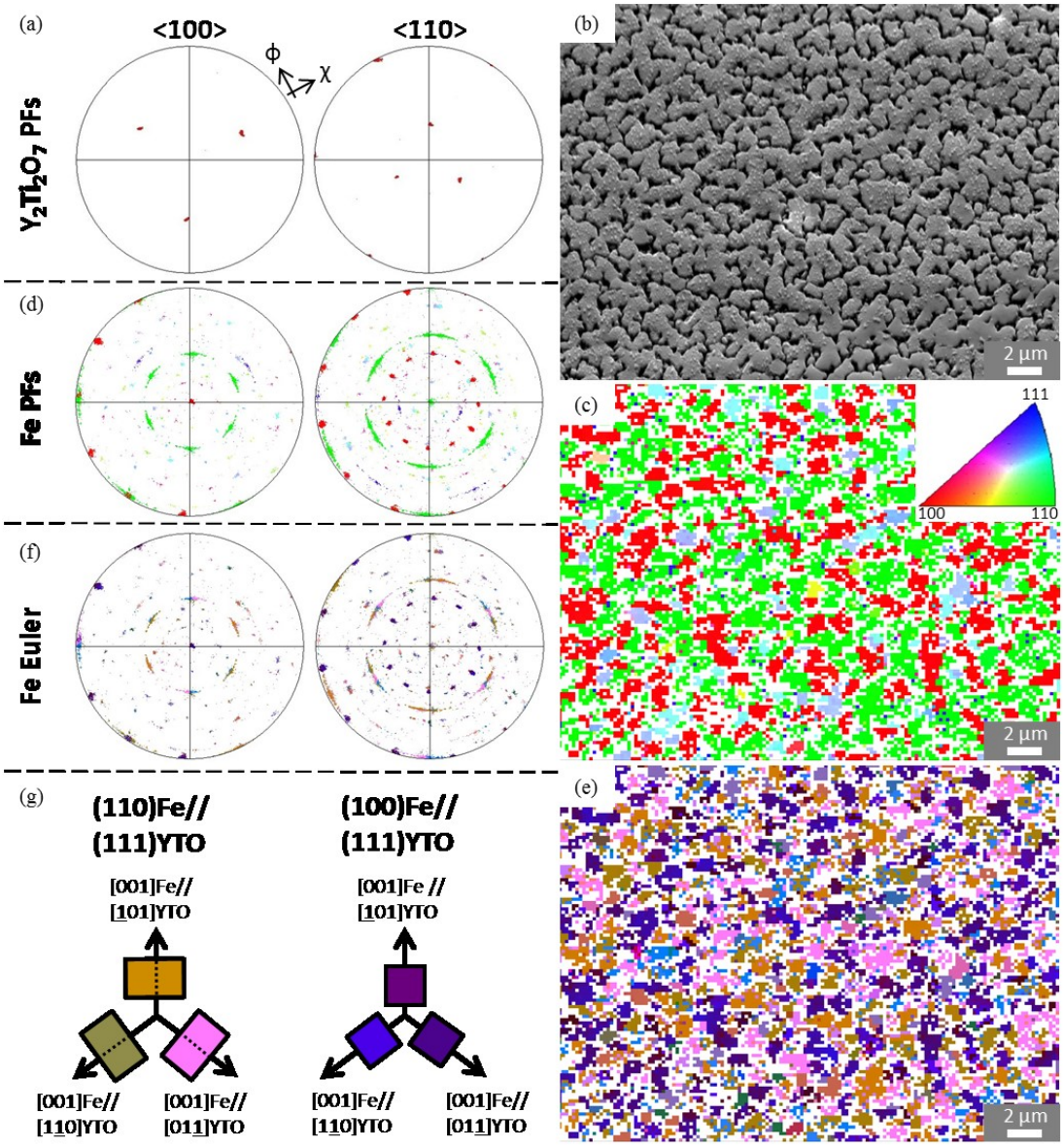

Figure 5.2 – (a) EBSD PFs of the {111}YTO substrate. (b) SEM of Fe grains. (c) EBSD inverse pole map of the Fe grains. The octant in the top right indicates the surface orientations of the Fe grains. (d) PFs showing date from {110}Fe grains in green and {100}Fe grains in red. (e) Euler map. (f) Euler pole figures showing the crystallographic orientation of each grain in the Euler map. (g) Schematic showing how the <100>Fe directions align with the three <110> directions of the {111} substrate.

5.5 TEM Characterization

A detailed cross-sectional TEM and HRTEM study was conducted to explore the structure of the Fe-YTO interface. The cross sectional TEM micrographs in Figure 5.3a and Figure 5.3b show the island type growth of the Fe on the YTO substrate. The grains range in cross-sectional size from 15 nm wide x 75 nm tall to 1000 nm wide x 500 nm tall. Thirteen grains were closely examined to determine crystalline orientation relative to the YTO substrate and their interfacial structure. Figure 5.3c illustrates the crystallographic orientations of the grains and substrate. The {100}Fe, {110}Fe, and {111}YTO surface orientations point upwards while the <110>YTO and TEM beam directions point into the page. The 13 grains studied are marked by arrows in Figure 5.3a and Figure 5.3b.

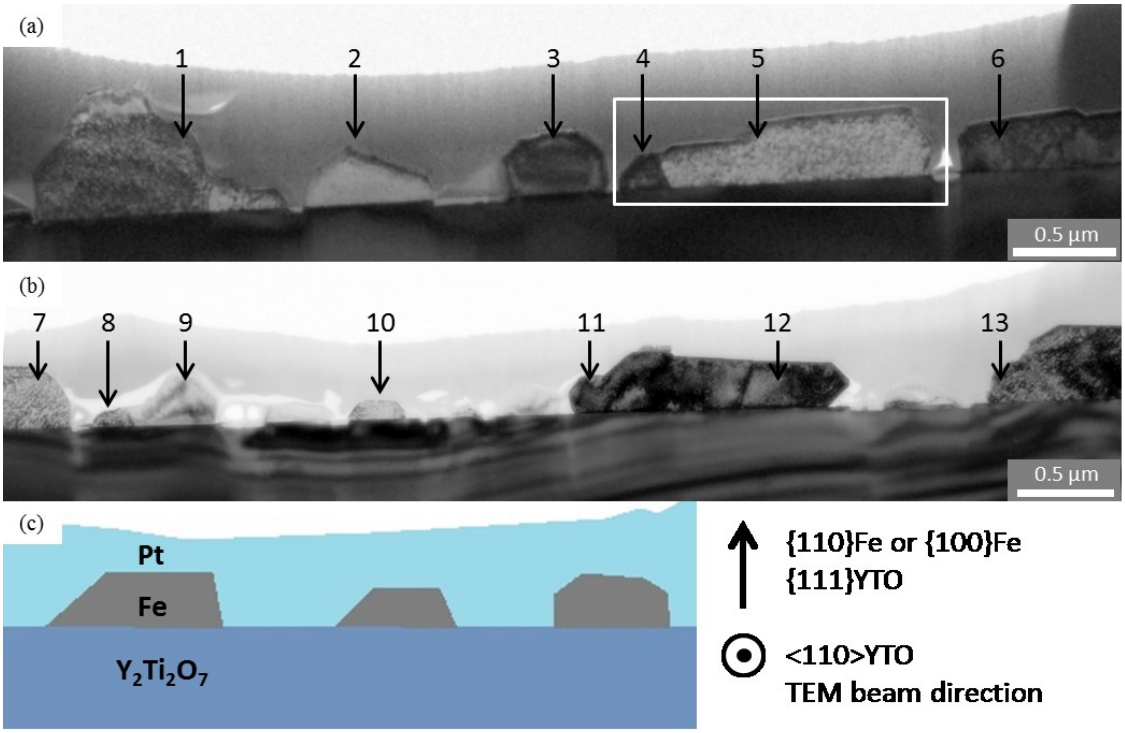

Figure 5.3 – (a) and (b) Cross-section TEM images of Fe grains on the {111} YTO substrate. (c) Sketch of (a) and (b) showing the crystallographic orientation of the grains and substrate.

The grain sizes and ORs of the 13 grains are summarized in Table 5.1 and are consistent with SEM, EBSD and XRD results. Diffraction pattern analysis shows that seven Fe grains have the OR: {110}Fe//{11}YTO and <111>Fe//<110>YTO (the in-plane OR is off 5°-10°) which is close to the Kurdjumov-Sachs (KS) OR. The KS OR is obtained from the Nishiyama-Wasserman (NW) orientation by a 5.26˚ rotation about the interface normal [7]. Thus the true OR of the seven Fe grains is NW OR1: {110}Fe//{111}}YTO and <100>Fe//<110>YTO. Four grains have OR2: {100}Fe//{111}YTO (off ≈ 1°) and <100>Fe//<110>YTO. Two grains have no OR with the {111}YTO substrate.

There does not seem to be a correlation between a grain's shape and it's crystallographic orientation. As seen in Figure 5.3a and Figure 5.3b, grains 3 and 10 are similar in size and shape but do not have the same OR. Grains 3 and 6 have different shapes but have the same OR.

Table 5.1 – Summary of grain sizes and ORs found for the 13 grains observed with HRTEM.

Grain	Size	Orientation
No.1	600 nm x 500 nm	NW OR1: {110}Fe//{111}YTO <111>Fe//<110>YTO
No.2	500 nm x 200 nm	No OR
No.3	400 nm x 300 nm	OR2: {100}Fe//{111}YTO <100>Fe//<110>YTO
No.4	250 nm x 200 nm	OR2
No.5	1000 nm x 300 nm	NW OR1
No.6	1000 nm x 250 nm	OR2
No.7	1000 nm x 500 nm	NW OR1
No.8	15 nm x 75 nm	NW OR1
No.9	500 nm × 500 nm	No OR
No.10	250 nm x 100 nm	NW OR1
No.11	1000 nm x 400 nm	OR2
No.12	500 nm x 300 nm	NW OR1
No.13	1000 nm x 500 nm	NW OR1

Fe grains 4 and 5, marked by the rectangular area in Figure 5.3a, are shown at higher magnification in Figure 5.4a. The two adjacent grains have different orientations shown by the nano-diffraction patterns in Figure 5.4b and Figure 5.4c. The selected area

diffraction pattern from the YTO substrate is shown in Figure 5.4d. Grain 4 is OR2 while grain 5 is NW OR1.

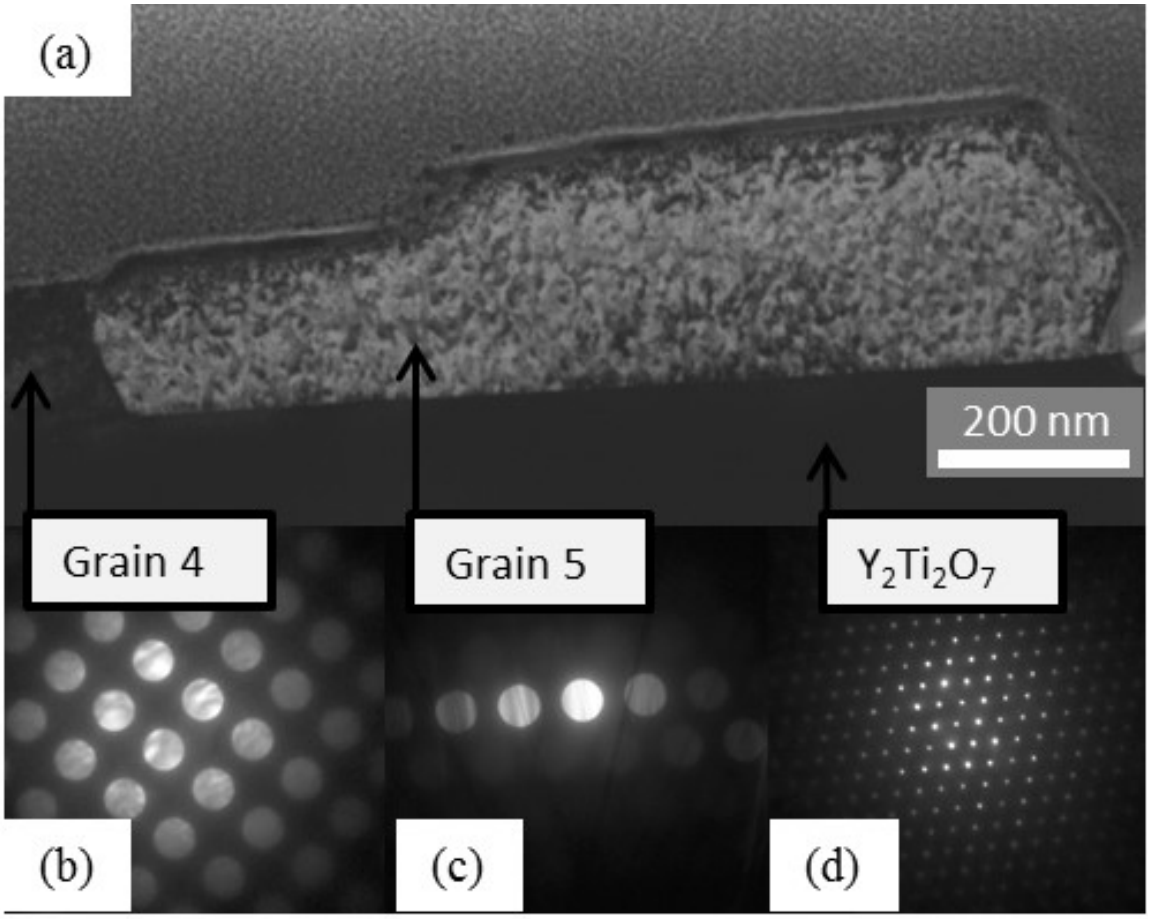

Figure 5.4 – (a) TEM image of grain 4 and grain 5 on the YTO substrate. (b) Nano diffraction pattern from grain 4. (c) Nano diffraction pattern from grain 5. (d) Select area diffraction pattern from the YTO substrate.

HRTEM was used to closely examine the interfaces between grains and the substrate. Figure 5.5 shows the interface structure that is typical of NW OR1 grains. This interface is sharp and flat at the near atomic scale. The substrate {111}YTO planes are

visible and marked by red lines in Figure 5.5. The termination of red lines at ledges accommodate the 5° surface miscut from {111}YTO. These ledges likely did not exist in the as-mechanically polished substrate. Thus the {111}YTO surface reconstructed to form ledges when it was at the deposition temperature of 800 °C. It is not clear if the reconstruction is enhanced or modified by the Fe deposition.

The light and dark regions about 8 nm apart coincide with the ledges and indicate that there is stress at the interface. This is likely the result of three {110}Fe planes fitting into the {111}YTO ledges with a 2% misfit. Note in view of the large nominal geometric Fe-YTO misfits for the NW OR1 interface, it is somewhat surprising that large strains are seen only at the ledges and other misfit dislocations are not observed. However, this may be partly due to the small dimensions of the discontinuous Fe island grains. In Figure 5.5, the row of light regions in the YTO substrate (≈ 6 nm below the interface) seems to be correlated with the light regions in the Fe. The source of these light regions is not understood.

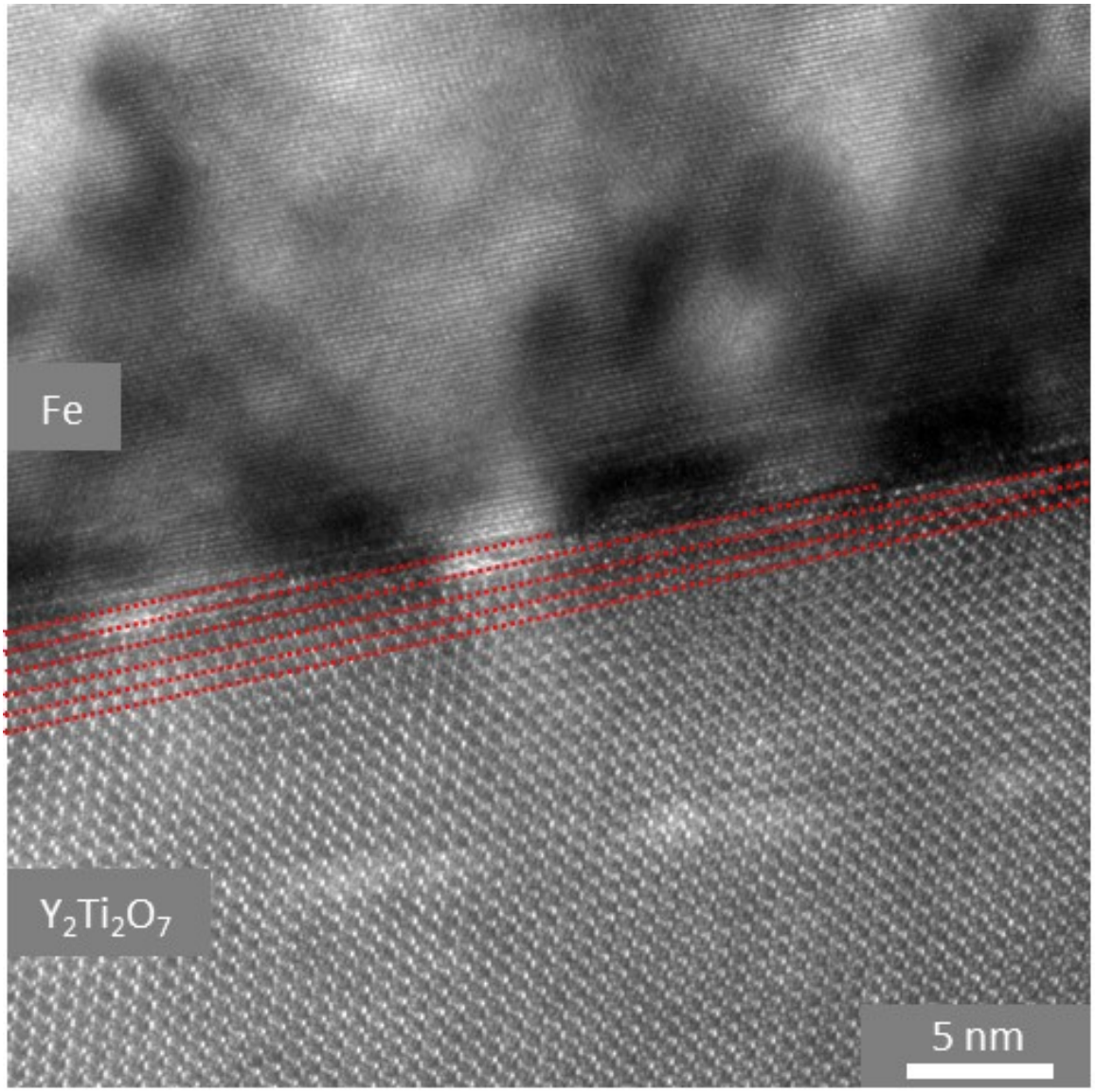

Figure 5.5 – HRTEM image from a grain with the {110}Fe//{111}YTO and <100>Fe//<110>YTO NW OR1. The red lines show {111}YTO planes. Dark and light strained areas are seen at substrate ledges.

Figure 5.6a shows a HRTEM image of the interface between the substrate and a grain with OR2. There is a 2-3 nm thick transition layer at the interface. The STEM/EDX

spectrum in Figure 5.6b shows that the transition layer is rich in Ti, O, and Fe and is consistent with a MO_x metallic oxide. However, the exact composition of the transition layer has not been measured. The {100}Fe grains are still close to parallel (off ≈ 1°) to the {111}YTO substrate despite the uneven transition layer.

Grains with OR2 are probably the result of a low deposition rate leading to oxidation of the Fe atoms at the hot substrate. In a second study using the same conditions, except that Fe was deposited at 2 nm/s (nearly seven times faster than in the current study), OR2 grains were not observed and all the grains selected the NW OR1 orientation. This observation supports the hypothesis that: a) the low Fe deposition rates result in interface oxidation; and, b) the {100}Fe oriented grains are a consequence of the oxide layer. Therefore OR2 can be considered to be an artifact.

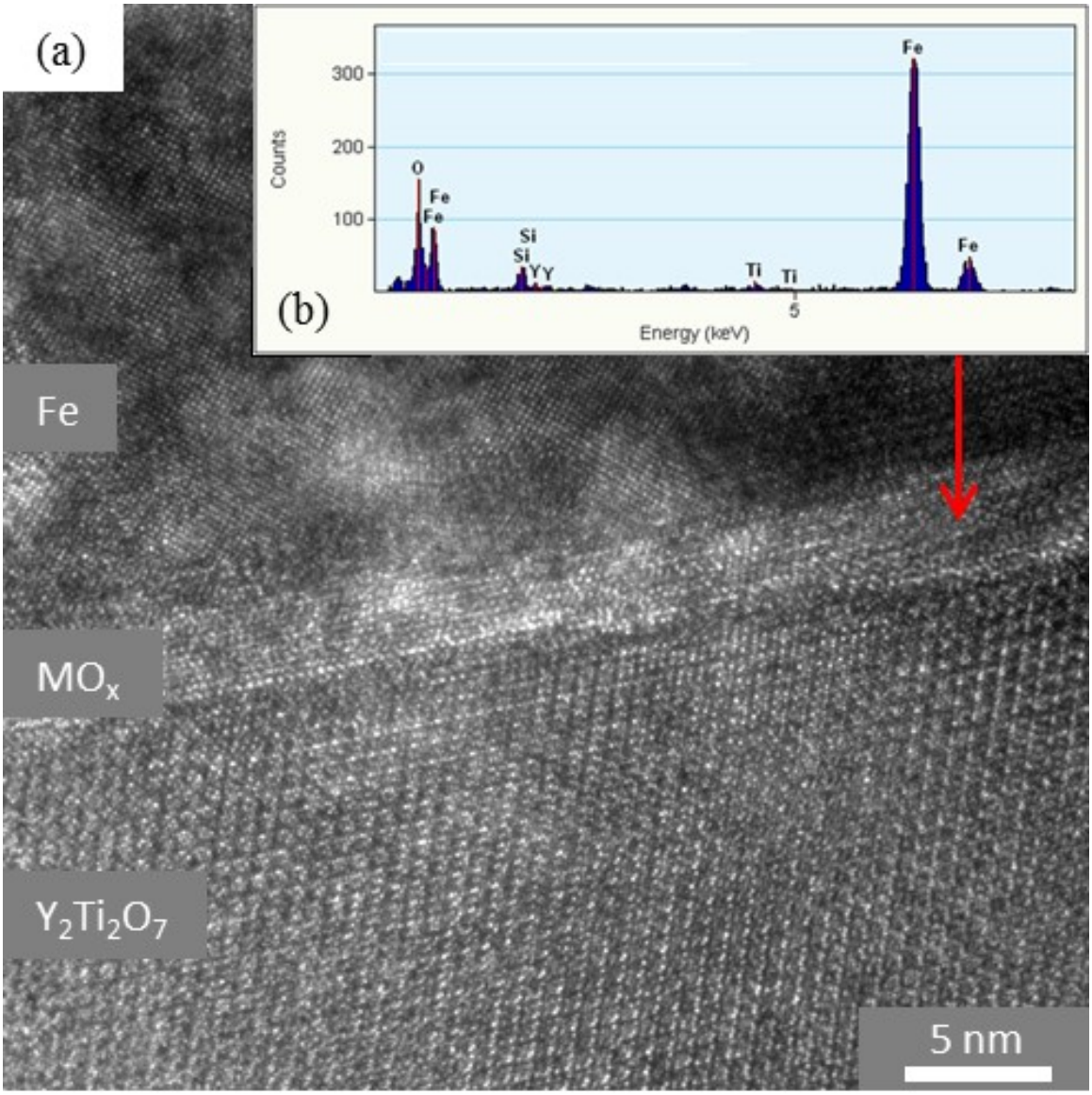

Figure 5.6 – (a) HRTEM images showing the interfacial transitional layer found between a Fe grain and the YTO substrate with the OR2 {100}Fe//{111}YTO (off ≈ 1°) and <100>Fe//<110>YTO. (b) An EDX spectrum taken from the transition layer in (a).

Figure 5.7 shows the interface of a Fe grain with no clear OR with the YTO substrate. The interface is atomically rough and incoherent. The YTO surface does not

have the clean ledges which were seen at grains with NW OR1. The ≈ 5 nm thick uneven dark area at the interface is probably also a MO_x transition layer. Grains with no OR generally have thicker MO_x transition layers than grains with OR2.

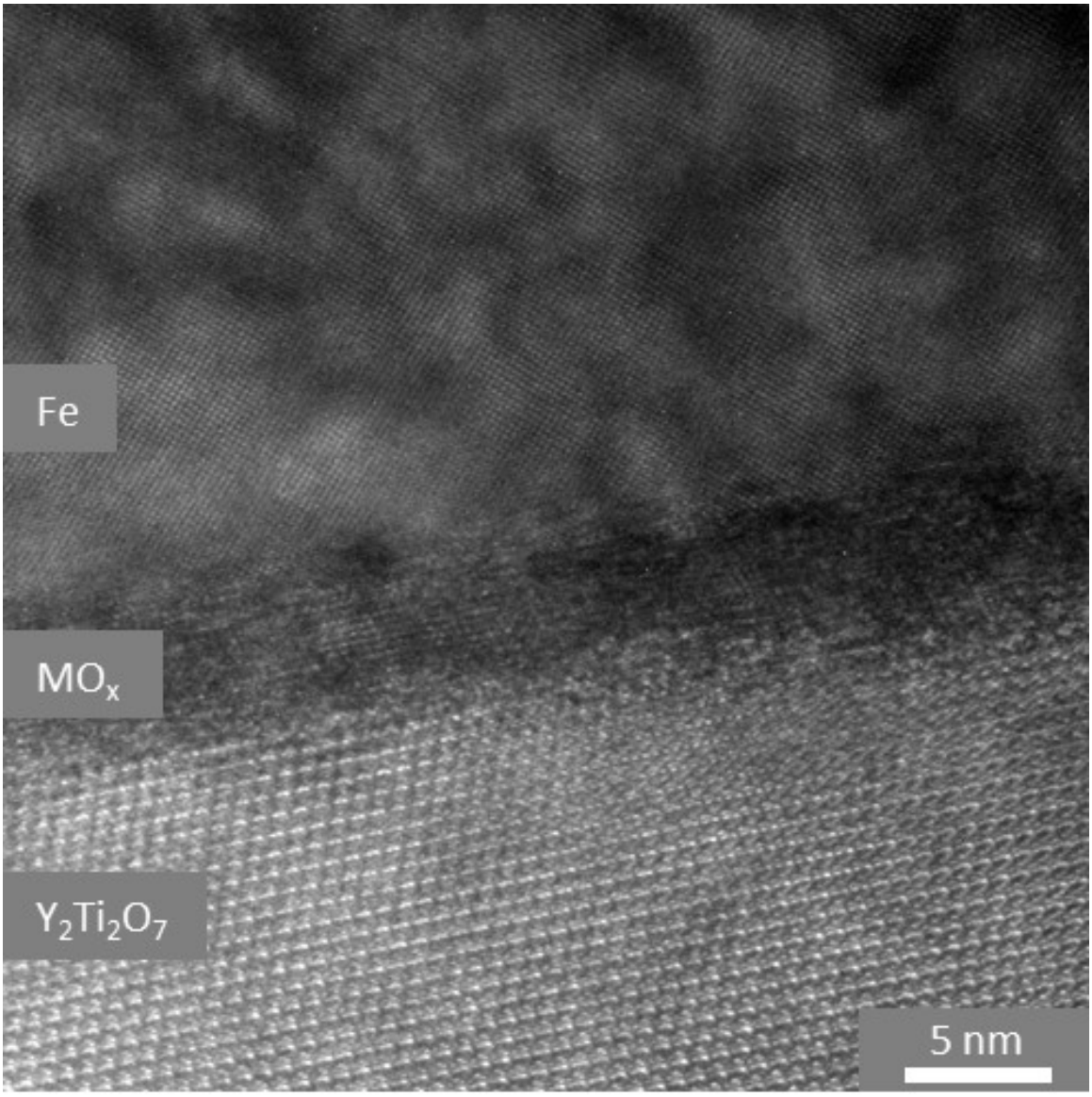

Figure 5.7 – The interface of Fe grains with no OR to the substrate. A thick transition layer is seen at the Fe-YTO interface.

5.6 Discussion

The objective of this work was to complement characterization studies of the interfaces between Y-Ti-O NOs and the bcc Fe-Cr ferrite matrix in NFA alloys. Here, mesoscopic, grain sized, interfaces were created by electron beam deposition of a thin Fe layer on a {111}YTO bulk single crystal surface. AFM and SEM scans show that the Fe grains had an average size of ≈ 0.5 μm. XRD, EBSD, and HRTEM scans show two main OR: (a) OR1: {110}Fe//{111}YTO and <100>Fe//<110>YTO and (b) OR2: {100}Fe//{111}YTO and <100>Fe//<110>YTO. Further, EBSD scans show that both {110} and {100} Fe grains had <100>Fe directions which matched one of the three <110> directions of the {111} substrate plane.

The atomic structures of the interfaces were further characterized using HRTEM. The NW OR1 interface is sharp and clean with dark and light strain areas spaced ≈ 8 nm apart. These strained regions are associated with ledges in the YTO that accommodate a 5° surface miscut from the {111}YTO planes. The ledges accommodate three {110} Fe layers with 2% misfit strain.

In contrast, the OR2 grains form along with a 2-3 nm thick transition layer between the Fe and YTO. This is apparently due to oxidation caused by the low deposition rate. Fe grains with no OR to the substrate had thicker MO_x transition layers. Thus the {100}Fe grains and interfaces lacking an OR can be considered artifacts.

The presence and thickness of the transition layer seem to dictate the OR between the grains and the substrate. Grains with NW OR1 were observed when there is no

significant transition layer. Grains with thick transition layers have no OR. The OR2 grains still maintain OR2 with the substrate, despite the lack of direct contact. This is somewhat surprising and gives rise to three hypothesis:

1. The MO_x layer has independent preferred ORs with both Fe and YTO that results in an apparent OR between the latter phases that are not in contact.

2. The MO_x layer provides a bridging phase for interaction between the Fe and YTO that minimizes the total interface and strain energy by selecting OR2 in the Fe grains.

3. The combination of 1 and 2, where the transition layer has better lattice matching with both the oxide substrate and Fe, while also relaxing the misfit and ledge strains in the OR2 selected versus NW OR1 grains.

Hypothesis 3 seems most plausible on energetic grounds, and is supported by the observations that: a) the periodic strain regions, seen with NW OR1 grains, are not present in the OR2 grains; and, b) OR2 occurs in the case of thin, but not thick, layers. Unfortunately, the detailed composition, structure and character of MO_x-YTO and MO_x-Fe interfaces have not yet been measured. Indeed, since the exact structures and compositions are not known, very thin non-stoichiometric interface zones, that are difficult to observe, may exist in even in the case of the NW OR1 grains. Notably such thin transition layers that relax strains in the Cu-Ta system have been reported [7]. These observations may be pertinent to core-shell structures that have been reported for embedded NOs, where the shells are rich in O, Ti, and Cr [8,9].

Additional Fe depositions on {111}YTO will be carried to study the effect of misorientation on the interface structure (both less than and greater than 5°). This work is also being extended to other $Y_2Ti_2O_7$ surfaces, including {110}YTO and {100}YTO. XRD and EBSD scans on an initial Fe deposit on a {100}YTO surface yielded only {110}Fe grains with no preferred in-plane OR with the oxide, as seen in the case of the amorphous substrate. The absence of a OR may be due to a non-stoichiometric termination of the {100}YTO surfaces. We also plan to study the interaction of implanted He with the NW OR1 interfaces with various misorientations.

While beyond the scope of this report, it will also be critical to link these and other experiments with detailed modeling studies. They should ultimately include both first principles calculations of interfaces and interface termination including the effect of stoichiometry, as well as atomistic calculations based on advanced interatomic potentials used in molecular dynamics-statics and Monte Carlo simulations.

5.7 Conclusions

In summary, mesoscopic interfaces were created by electron beam deposition of a Fe layer on a {111} YTO surface. SEM, EBSD, XRD, and TEM techniques were used to study the structures. The following observations were made:

- Grains deposited on amorphous pyrex are {110} textured and have no in-plane OR with the substrate.

- The interface for grains with NW OR1 {110}Fe//{111}YTO and <100>Fe//<110>YTO are atomically clean with no significant transition layer, and have strained regions at ledges due to the miscut substrate.
- Grains with OR2 {100}Fe//{111}YTO and <100>Fe//<110>YTO have a 2-3 nm transition layer at the interface.
- Grains with no OR have a thick transition layer.
- NW OR1 and OR2 grains have <100>Fe directions that match one of the three <110> directions of the {111} substrate plane.
- Grains with OR2 and with no OR are believed to be an artifact of the low deposition rate. Additional Fe depositions will be done to study the effects of misorientation.

5.8 Acknowledgements

I would like to thank K. Sickafus (UT) for help with experiment design, H. Dabkowska (MU) for providing the single crystal, Y. Li (UCSB) for XRD training, G. Steward (UCSB) for SEM and EBSD scans, Y. Wu (UCSB) for TEM imaging, and G.R. Odette (UCSB) for guidance and support.

5.9 References

[1] T. Stan, Y. Wu, G.R. Odette, K.E. Sickafus, H.A. Dabkowska, B.D. Gaulin, Metall. Mater. Trans. A Phys. Metall. Mater. Sci. 44 (2013) 4505–4512.

[2] G.R. Odette, D.T. Hoelzer, JOM 62 (2010) 84–92.

[3] G.R. Odette, JOM 66 (2014) 2427.

[4] J.S. Gardner, B.D. Gaulin, D.M. Paul, J. Cryst. Growth 191 (1998) 740–745.

[5] M.B. Johnson, D.D. James, A. Bourque, H.A. Dabkowska, B.D. Gaulin, M.A. White, J. Solid State Chem. 182 (2009) 725–729.

[6] N.I. Kato, J. Electron Microsc. (Tokyo). 53 (2004) 451–458.

[7] A. Hashibon, A.Y. Lozovoi, Y. Mishin, C. Elsässer, P. Gumbsch, Phys. Rev. B - Condens. Matter Mater. Phys. 77 (2008) 1–9.

[8] E.A. Marquis, Appl. Phys. Lett. 93 (2008) 10–13.

[9] C.A. Williams, P. Unifantowicz, N. Baluc, G.D.W. Smith, E.A. Marquis, Acta Mater. 61 (2013) 2219–2235.

Chapter 6 Fe – {100}YTO Bilayers

6.1 Introduction

The following chapter has been submitted as a stand-alone publication to Metallurgical and Materials Transactions A. Research to characterize nano-oxide (NO) compositions, structures, misfit strains, core shell structures, and NO-matrix orientation relationships (ORs) is ongoing [1–5]. Most of the smallest NOs are $Y_2Ti_2O_7$ (YTO) fcc pyrochlore [3–12]. The cuboidal NOs have multiple interfacial orientation relationships (ORs), usually with low index {100}, {110}, and {111} YTO planes bonded to the surrounding matrix. Here we focus on the Fe-{100}YTO type interfaces such as the cube on cube {100}Fe//{100}YTO and <100>Fe//<100>YTO observed in [6,8], the cube on 45° rotated cube {100}Fe//{100}YTO and <100>Fe//<110>YTO observed in [8,13], and the edge on cube {110}Fe//{100}YTO and <100>Fe//<100>YTO observed in [8].

Detailed characterization and analysis of the NO-matrix interfaces is needed to develop first principles and atomic-scale interface models that are part of multi-scale efforts to predict the behavior of nanostructured ferritic alloys (NFAs) and NOs during processing and in irradiation service environments. YTO-matrix ORs are of particular interest because they impact selection of compositions and processing paths, service stability, mechanical properties and irradiation tolerance of NFAs. Interface characteristics

include structures, local chemistries, defects, misfit strains, energies and NO interactions with He. The embedded NOs are challenging to characterize, partly due to their small size.

6.2 Experimental

The feed rods for the YTO single crystal Czochralski-type growth were prepared by solid state reactions at the University of Tennessee. Appropriate mixtures of Y_2O_3 and TiO_2 were ground together, and pressed into 6 mm diameter, 60 mm long rods under 400 atm hydrostatic pressure, followed by calcinations in air at 1673K (1400 °C) for 24 hrs. The growth was carried out in 5 atm oxygen in an IR-heated image furnace at a rate of 3 mm/hr. The YTO single crystals were {100} surface oriented and 2 mm thick wafers were cut from the rod using a wire saw.

An Allied Multiprep was used to polish the wafers using a sequence of diamond lapping films, followed by a final 15 minute polishing step using a 0.02 μm non-crystallizing colloidal silica suspension. The substrates were then cleaned in an ultrasonic bath with 90% reverse osmosis water and 10% Micro-Organic soap for 10 minutes. This was followed by an acetone ultrasonic bath for 10 minutes, and finally an isopropanol ultrasonic bath for 10 minutes.

The YTO single crystal wafers were loaded into a Varian electron beam deposition system and heated to 1073K (800 °C) at a rate of 0.166 K/s. After allowing the crystal to sit at temperature for 1 h, 2 μm of Fe was deposited at a rate of ~8 nm/s (250 s total) at chamber pressure of 3 x 10^{-6} Torr. After deposition, the Fe-YTO bilayer was annealed in

vacuum at 1073K (800 °C) for 30 min. The {100}YTO substrate was slowly cooled to room temperature prior to unloading.

Electron backscatter diffraction (EBSD) pole figures, orientation maps, and 3D representations were obtained using an FEI Quanta 400F field-emission scanning electron microscope (SEM). An FEI HELIOS Focused Ion Beam (FIB) was used to first deposit ~1 μm of protective platinum over areas of interest. Cross-sectional lift-outs of the Fe-YTO interface were extracted, thinned to less than 50 nm, and cleaned with a low energy 2 keV 5.5 pÅ gallium beam. High resolution transmission electron microscopy (HRTEM) and energy dispersive x-ray (EDX) measurements were performed on a 300 keV FEI Titan TEM. CrystalMaker software was used to analyze the bulk lattice matching. An atom probe tomography (APT) measurement was conducted in a CAMECA LEAP 3000X HR to characterize the interface chemistry. A FIB machined tip was sharpened to <100 nm diameter and cleaned with a 2 keV gallium beam. The tip was run in laser mode at 31K (-232 °C) with a pulse energy of 0.2 nJ, pulse repetition rate of 200 kHz, and a detection rate of 0.005 ions/pulse.

6.3 SEM and EBSD Characterization

The 2 μm thick Fe film had two dominant morphologies: a larger {110}Fe polycrystalline region covering ~99% of the deposit, and a smaller (100 μm x 100 μm) {100}Fe monocrystalline grain. The monocrystalline grain is of particular interest because it has the OR found in some embedded NOs (as discussed below). The multipart Figure 6.1

and Figure 6.2 show SEM and EBSD data from the {110}Fe and {100}Fe areas, respectively. Note the figures are equally scaled and formatted to facilitate side-by-side comparisons. While we focus on one deposition here, many other Fe-{100}YTO deposits have been fabricated with generally similar characteristics.

Figure 6.1 shows SEM and EBSD data from the {110}Fe polycrystalline side. Figure 6.1a is an SEM image showing that the polycrystalline Fe layer is comprised of 1 – 3 μm grains. Ledges are seen on the surface of some grains. The EBSD inverse pole figure z-direction (IPFZ) map in Figure 6.1b shows a strong {110} out-of-plane orientation. The dark areas are locations where the EBSD pattern could not be indexed, often at grain boundaries. Figure 6.1c shows the same EBSD data as Figure 6.1b, but represented as an Euler pole figure (PF) map where crystallographic orientations are assigned a unique color. The grains all have a {110} out-of-plane orientation, but there are four in-plane variants represented by four colors. Comparing the SEM image in Figure 6.1a and the Euler map in Figure 6.1c, shows that the green and orange variants coalesce, as do the purple and blue grains.

Figure 6.1d shows three PFs (<100>, <110> and <111> reflections) for the same data as Figure 6.1b, colored according to the out-of-plane grain orientation (IPFZ). For clarity, only reflections from the grain centers are shown in the PFs. Spots are only seen in the center of the <110> PF, confirming the strong {110} Fe texturing. Figure 6.1e again shows three PFs, but colored according to the Euler orientations. There are four grain orientation variants (purple, blue, green and orange). Figure 6.1f shows the PFs for the

YTO substrate with a <100> spot close to the center reflecting the {100} YTO surface orientation.

The Fe-YTO orientation relationship (OR) was obtained by matching spots in the Fe PFs in Figure 6.1e with the accompanying YTO PFs in Figure 6.1f. The overlapping center spots from the <110>Fe PF and the <100>YTO PF indicate parallel surfaces. Similarly, the overlapping spots at the PF rims indicate parallel in-plane directions. Thus, the OR for the polycrystalline film is:

{110}Fe//{100}YTO and <111>Fe//<110>YTO

This particular edge-on-cube orientation has not been observed for embedded NOs in NFAs. The 3-dimensional renderings in Figure 6.1g show that the four Fe grain variants have a <111> Fe direction matched with one of the two <110> YTO in-plane directions. The purple and blue grains share a common <111> Fe direction, as do the green and orange grains. The purple/blue and green/orange grain pairs have the exact same OR with the substrate, but are 90° rotated from one another, matching the 2-fold symmetry of the underlying {100} YTO.

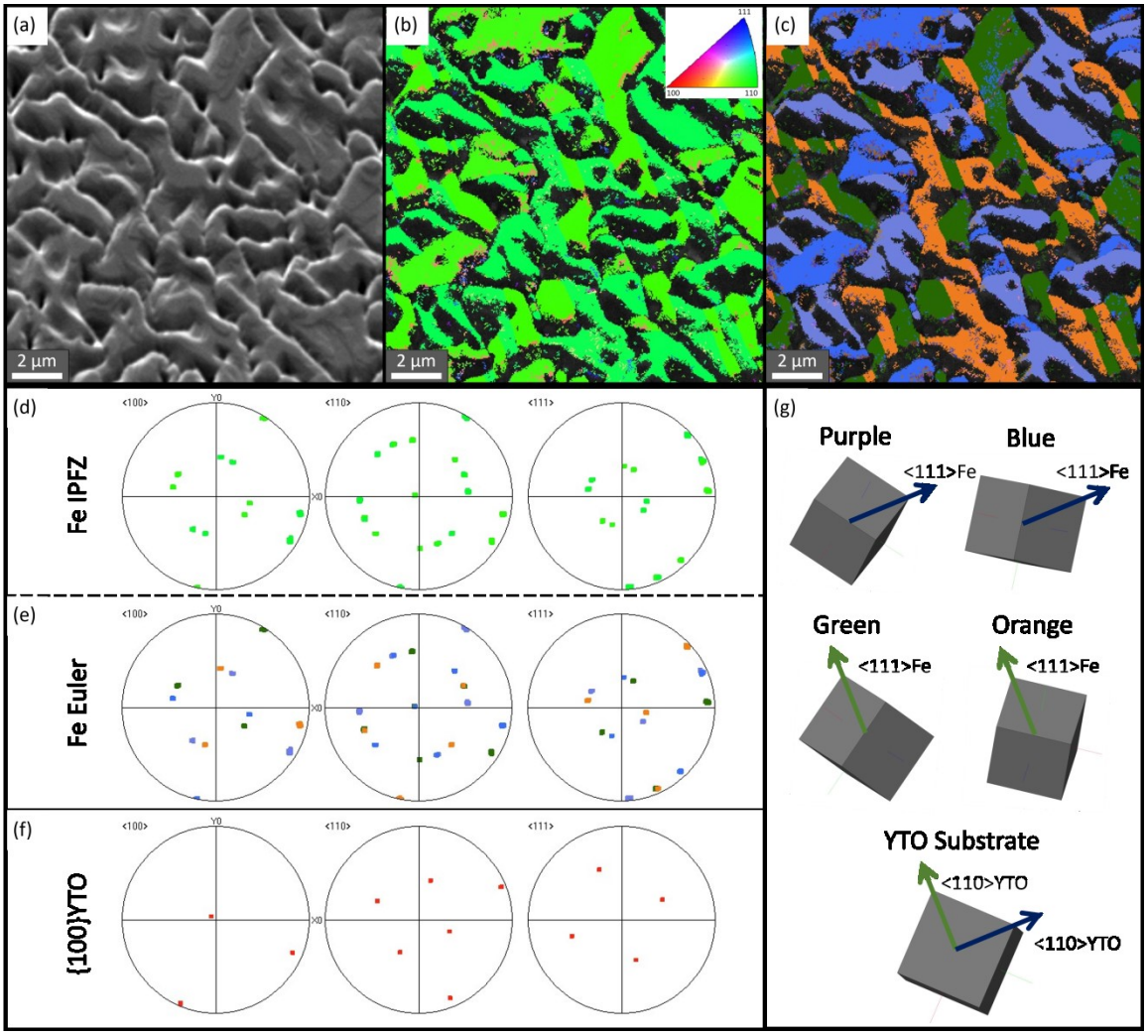

Figure 6.1 – SEM/EBSD data from polycrystalline side showing (a) SEM image of 1 – 3 micron elongated grains, (b) IPFZ map with out-of-plane {110} Fe texturing, (c) Euler map indicating four in-plane variants, (d) IPFZ pole figures, (e) Euler pole figures, (f) YTO pole figures, (g) 3D representation of {110} Fe grains and {100} YTO substrate.

Figure 6.2 shows SEM and EBSD data from the 100 µm x 100 µm monocrystalline grain. Figure 6.2a is an SEM image showing one continuous flat area with no grain boundaries. Ledges are seen on the film surface. Figure 6.2b shows an EBSD inverse pole

figure (IPF) map of the same area as Figure 6.2a, depicting the out-of-plane {100} Fe crystallographic texturing. The black streaks coincide with ledges where the EBSD signal could not be indexed. Figure 6.2c represents the same EBSD data as Figure 6.2b but as an Euler map confirming only one in-plane orientation.

Figure 6.2d shows three PFs (<100>, <110> and <111> reflections) for the same data in Figure 6.2b, with a strong, uniformly red out-of-plane {100} grain texturing. Figure 6.2e shows three PFs, all having same color associated with one in-plane orientation. Figure 6.2f repeats the illustration in Figure 6.1f for easy comparison. The Fe-YTO OR for the monocrystalline patch was obtained by matching spots in the Fe PFs in Figure 6.2e with the YTO PFs in Figure 6.2f. The observed OR for the monocrystalline film is close to:

{100}Fe//{100}YTO and <100>Fe//<110>YTO.

This rotated cube-on-cube OR, also known as the Baker and Nutting OR, has been observed for NOs in NFAs [4,8]. The 3D renderings in Figure 6.2g confirm that there is only one epitaxial orientation relationship between the Fe film and the underlying YTO substrate.

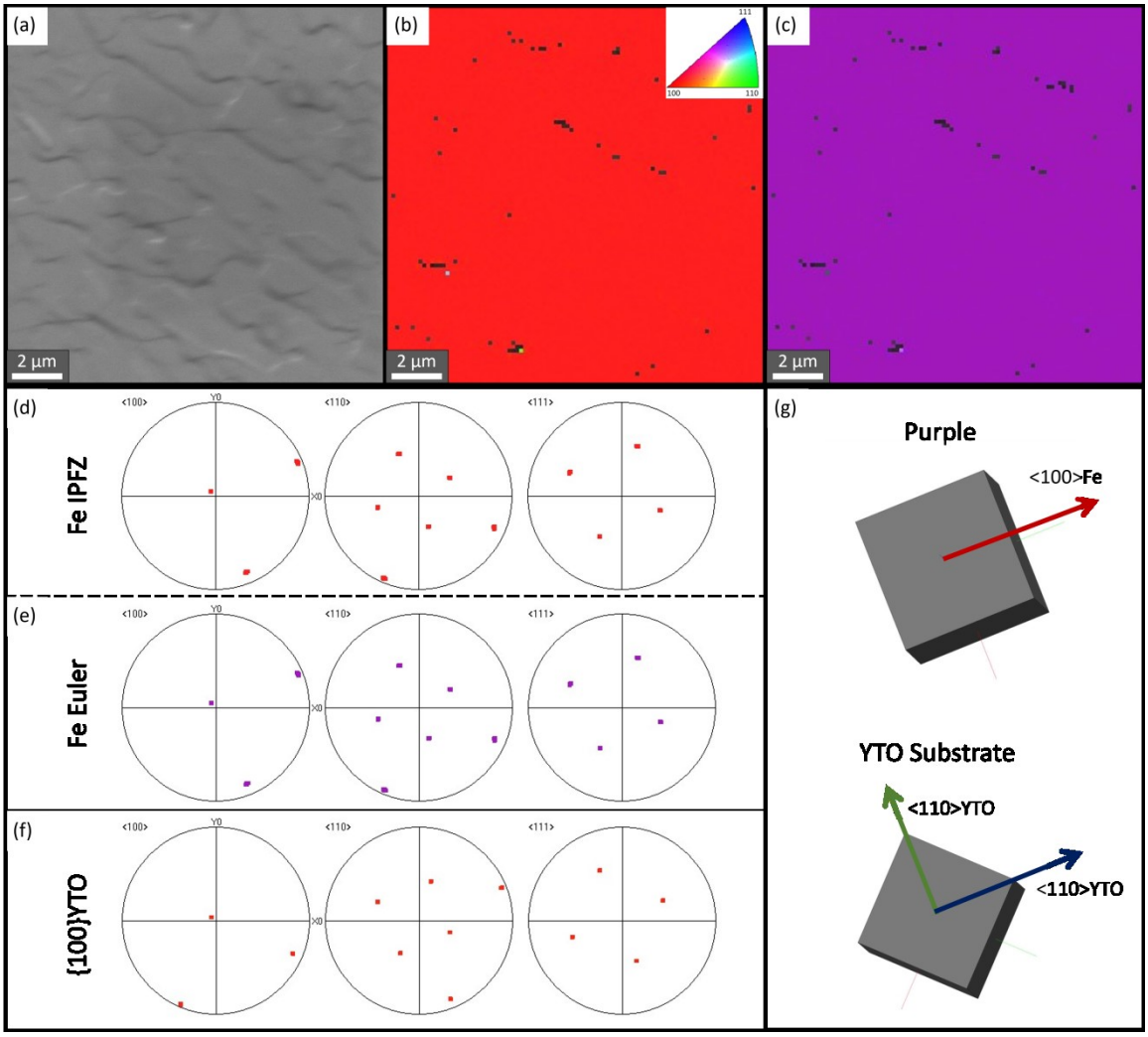

Figure 6.2 – SEM/EBSD data from monocrystalline side showing (a) SEM scan showing a large flat area, (b) IPFZ map showing out-of-plane {100} Fe texturing, (c) Euler map indicating one in-plane variant, (d) IPFZ pole figures, (e) Euler pole figures, (f) YTO pole figures, (g) 3D representation of {100} Fe film and {100} YTO substrate.

6.4 HRTEM and APT Characterization

High Resolution Transmission Electron Microscopy (HRTEM) was used to investigate the structure of the Fe-YTO interfaces. Figure 6.3 shows HRTEM images from: (a) one of the {110}Fe polycrystalline grains; and, (c) the large {100}Fe monocrystalline grain. In both cases, the images are aligned close to the <110> YTO in-plane zone axis, with the {100} YTO surface pointing up. The figures are equally scaled and formatted to facilitate side-by-side comparisons.

Figure 6.3a shows that the <111> Fe and <110> YTO in-plane zone axis directions are aligned and the atomic planes are well resolved. The white arrows indicate the location of periodic interfacial misfit dislocations which are ~ 0.7 nm apart. The dislocations are more easily seen in the Fast Fourier Transform (FFT) image in Figure 6.3b where the diagonal stripes in the Fe side represent {110} planes and the diagonal stripes in the YTO side represent {222} planes. EDX point measurements on the interface did not indicate the presence of contaminants or impurities above background levels.

Figure 6.3c shows the HRTEM cross-section image of the monocrystalline {100} Fe interface. There is a slight (~5°) misalignment between the <100> Fe and <110> YTO zone axis thus the YTO lattice is not resolved in the image. The white arrows indicate the location of periodic misfit dislocations that are ~1.4 nm apart. This misfit dislocation spacing was also observed for embedded NOs [14]. Notably, 1.4 nm is twice the spacing found for the polycrystalline portion in Figure 6.3a. The 5° misalignment in this OR does not allow a clear FFT analysis. Similar to the polycrystalline grains, EDX point

measurements on the interface did not indicate the presence of contaminants above background levels.

The {100}Fe patch is of particular interest as it has an OR observed in embedded NOs, thus APT was used to further study the interfacial chemistry. Figure 6.3d shows the APT reconstruction of the Fe-YTO tip with Fe in blue and YTO in green. Figure 6.3e shows a compositional line scan across the interface. To minimize artifacts inherent to APT, the compositional profile was created using a 20 nm diameter cylinder from the core of the tip and smoothed using a moving average of 3 sequential bins, each with a fixed width of 0.2 nm. The Figure 6.3f insert is a re-scaled version of Figure 6.3e to more clearly show the low levels of impurity at the interface (orange line) which had a peak of 0.83 at% and was composed of C (45%), N (35%), Cr (16%), and Al (4%). These low impurity levels are expected for depositions where in-situ surface cleaning just prior to deposition was not possible.

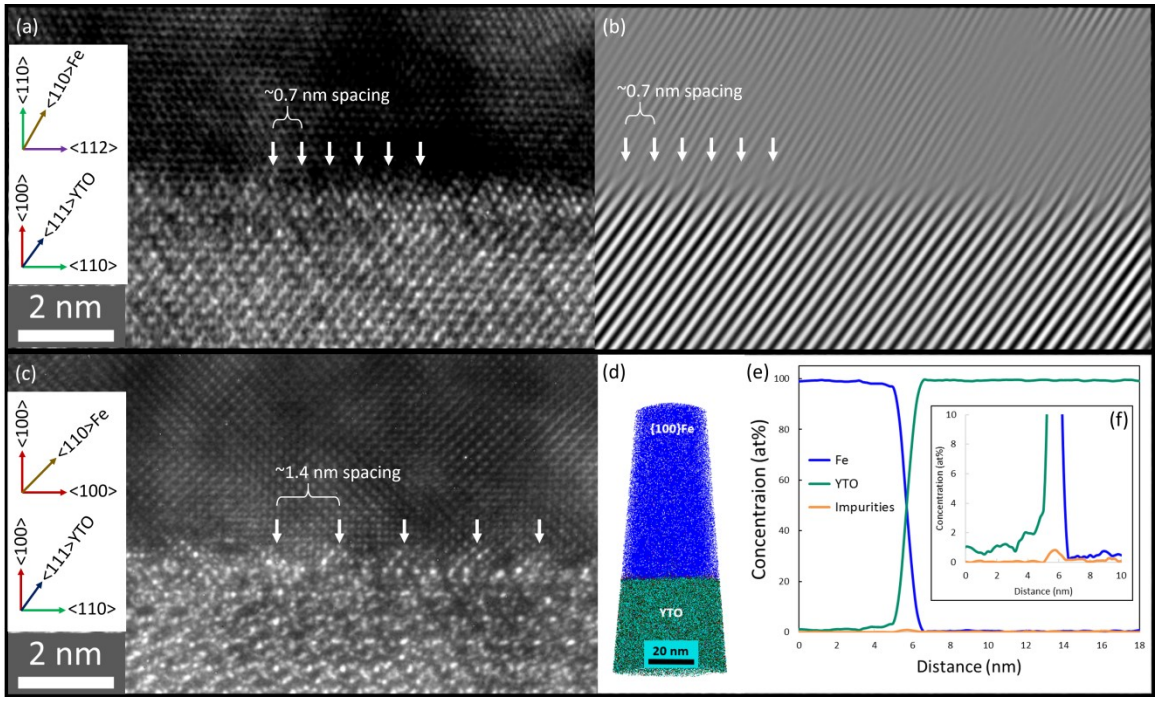

Figure 6.3 – HRTEM image from (a) the {110}Fe polycrystalline side, (b) the Fast Fourier Transform, and (c) the {100}Fe monocrystalline side. Misfit dislocations are shown with white arrows. (d) APT reconstruction of the {100}Fe-YTO interface. (e) Concentration profile of the interface and a rescaled version (f) indicating low impurity levels.

6.5 CrystalMaker Analysis

*C*rystalMaker was used to analyze and gain insight into the atomic matching of the two interfaces observed in this study. The following calculations are for bulk, un-strained, Fe and YTO. Figure 6.4a is a side-view of the polycrystalline {110}Fe-YTO interface, with the same orientation as in the HRTEM image in Figure 6.3a. Similarly, Figure 6.4b represents the monocrystalline {100}Fe-YTO interface. Fe atoms are orange, Y green, and Ti blue. Oxygen atoms were omitted from the CrystalMaker images for clarity. The

diagonal yellow lines in the Fe side indicate {110} planes, while the diagonal blue lines in the YTO side indicate {222} planes.

The mismatch between two lattices is calculated as $\varepsilon = (d_2-d_1)/(d_1)$ where d_1 and d_2 are plane spacings and $d_1 > d_2$. For values of ε over a few percent, the lattice with smaller spacing will have interfacial misfit dislocations that accommodate strain. These dislocations are marked with black in Figure 6.4a and Figure 6.4b and their Burger's vectors $\vec{b}$ were obtained using a Burger's circuit analysis [15,16] indicated by black arrows surrounding a dislocation.

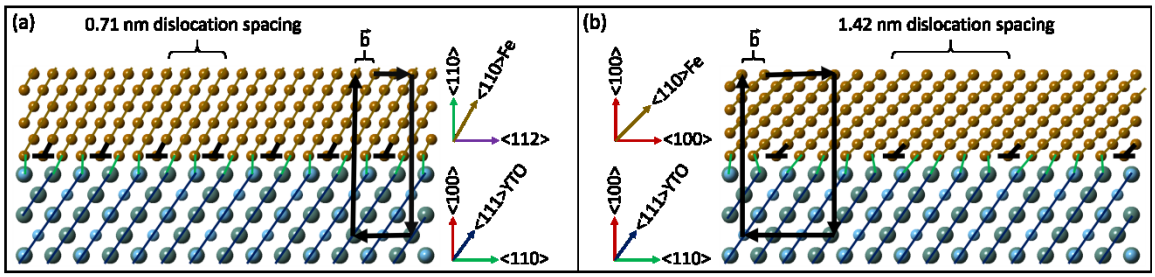

Figure 6.4 – CrystalMaker renderings of the Fe-YTO interfaces from the (a) {110} polycrystalline side and (b) {100} monocrystalline side. Fe is shown in orange, Y in green, and Ti in blue. The calculated dislocation spacings match the experimental observations in Figure 6.3.

The expected misfit dislocation spacing D_{mis} is calculated using conventional dislocation theory [15,17]. For any two lattices where the planes are perpendicular to the interface, there will be a near-coincident atomic match when $(n)d_1 = (n+1)d_2$. Thus the number of required d_1 planes for the larger lattice is $n = d_2/(d_1–d_2)$. The resulting lattice match, and misfit dislocation spacing, is $D_{mis} = (n)d_1$. However, as seen in Figure 6.4a,

neither the {110}Fe planes nor the {222}YTO planes are perpendicular to the interface, thus their horizontal spacing must be used. The horizontal planar separation is $S = d/\sin(\theta)$, where θ is the angle between the plane and the interface. Thus, the number of required planes is $n = S_2/(S_1-S_2)$, and the expected misfit dislocation spacing $D_{mis} = (n)S_1$. Because the misfit dislocations create a network along the two-dimensional interface, the dislocation number density is calculated as $\rho = 2/D_{mis}^2$.

For the YTO substrate, the {222} planar separation along the interface is $S_{YTO} = d_{222}/\sin(54.7°) = 3.57$ Å. This value is used for analyzing both {110}Fe and {100}Fe interfaces since they share the same substrate {100}YTO orientation.

For the polycrystalline OR in Figure 6.4a, the Fe planar separation along the interface is $S_{Fe} = d_{110}/\sin(60°) = 2.36$ Å. Thus, the lattice mismatch is $\varepsilon = 34\%$. The Burger's circuit analysis indicates misfit dislocations with $\vec{b}$ = <112>{110}Fe and $|\vec{b}|$ = 2.04 Å. Since $n \approx 2$, every second YTO plane is well matched with every third Fe plane. Further, $D_{mis} = (n)S_{YTO} = 7.14$ Å which matches the observed misfit dislocation spacing in the HRTEM image in Figure 6.3a. The interface misfit dislocation density is very high at $\rho = 3.97\text{x}10^{18}$ dislocations/m^2.

Figure 6.4b shows the CrystalMaker rendering of the monocrystalline {100}Fe interface. The diagonal yellow lines in the Fe side again indicate {110} planes, but now with $S_{Fe} = d_{110}/\sin(45°) = 2.89$ and the lattice mismatch is $\varepsilon = 19\%$. The resulting misfit dislocations have $\vec{b}$ = <110>{100}Fe with $|\vec{b}|$ = 2.36 Å. Since $n \approx 4$, every fourth {222}YTO plane matches with every fifth {110}Fe plane. The resulting misfit dislocation

spacing D_{mis} = 14.2 Å matches the HRTEM observations in Figure 6.3c. The misfit dislocation density is $\rho = 9.92 \times 10^{17}$ dislocations/m^2. The results for both interfaces are summarized in Table 6.1.

Table 6.1 – Properties of the two observed interfaces.

Property	Polycrystalline Grains	Monocrystalline Patch
Interface Type	Edge on Cube	Cube on Cube
Parallel Surfaces	{110}Fe//{100}YTO	{100}Fe//{100}YTO
Parallel Directions	<111>Fe//<110>YTO	<100>Fe//<110>YTO
Lattice Mismatch (%)	34	19
Burger's Vector $\vec{b}$	<112>{110}	<110>{100}
Burger's Vector Magnitude (Å)	2.04	2.36
Dislocation Spacing (nm)	0.71	1.42
Dislocation Density (#/m^2)	3.97×10^{18}	9.92×10^{17}

6.6 Discussion

Two epitaxial ORs were observed in this study. The majority of the film had 1 – 3 μm grains with the OR: {110}Fe//{100}YTO and <111>Fe//<110>YTO. However, a large 100 μm x 100 μm grain had an OR that is also found in the embedded NOs: {100}Fe//{100}YTO and <100>Fe//<100>YTO. Neither of these two ORs were observed for Fe-Y_2O_3 [18,19] or Fe-TiO_2 [20] bilayers.

It is not yet clear why two Fe orientations are observed on the {100}YTO substrate. As shown in Table 6.1, the lattice mismatch for the dominant polycrystalline {110}Fe is ε = 34% and the dislocation density $\rho = 3.97 \times 10^{18}$ dislocations/m^2, while the {100}Fe patch has ε = 19% and $\rho = 9.92 \times 10^{17}$ dislocations/m^2. The {110}Fe grains may have a higher

interface energy than the {100}Fe patch due to the higher mismatch and dislocation density. However, as is common for high angle grain boundaries, the strain fields of very closely-spaced misfit dislocations can overlap and cancel [17]. It is possible that although the {110}Fe grains may have a higher interface energy compared to the {100}Fe, the overall energy of the system might be lower if the strain is relieved.

The relief of strain using a very high density of misfit dislocations in Fe may only happen in depositions on unconstrained YTO mesoscale interfaces. In contrast, the smallest embedded NOs in NFAs are likely coherent, with misfit strains that increase with decreasing size, partitioned between the Fe and YTO precipitate, eventually becoming semicoherent. For example, a study by Wu et al. showed a 2 nm x 3 nm $Y_2Ti_2O_7$ NO had ~5% coherency strain with a 5 x 7 near coincident site lattice [4].

The substrate chemistry and termination may also affect the orientation for the deposited Fe film. In studies of Fe depositions on {111} YTO [21], a dominant {110} Fe texturing was observed for grains with clean Fe-YTO interfaces. However, Fe grains had a {100} orientation when a 2 – 3 nm thick contaminant interlayer was present at the Fe-YTO interface, and grains had no OR with the substrate when the interlayer was >5 nm thick. In the present study, neither the polycrystalline grains nor the monocrystalline patch had an HRTEM observable interlayer. EDX point measurements on both interfaces were similar, and the APT investigation of the {100} Fe patch did not indicate the presence of an interlayer or unexpected impurities. It is possible that grain island nucleation events take place at locally contaminated or otherwise defected sites which would be very difficult to

detect by HRTEM, EDX and APT. Note that rapid, highly driven, self-selection of interfaces may not always follow the minimum energy path. The two interface variants observed in this study actually present an opportunity to examine the similarities and differences in future He injection experiments.

The simplified bilayer model system of Fe on YTO provides the opportunities to use bulk mass spectroscopy measurements to observe the He partitioning. The corresponding He bubble size distributions, number densities, volume fractions, and spatial distribution will be observed using TEM. These experimental observations are critical to calibrating models that predict the behavior of NFAs and NOs in irradiation environments.

6.7 Conclusions

In conclusion, mesoscopic epitaxial Fe-YTO bilayers were successfully fabricated by electron beam Fe on {100} YTO single crystal surfaces. We report for the first time, the dominant fine grained polycrystalline OR is {110}Fe//{100}YTO and <111>Fe//<110>YTO with four variants that match the underlying substrate symmetry. HRTEM showed a semicoherent interface with misfit dislocation spacing of ~ 0.7 nm, consistent with CrystalMaker analysis. In contrast, a larger monocrystalline Fe grain had the {100}Fe//{100}YTO and <100>Fe//<110>YTO OR that is also found in embedded NOs. HRTEM showed a semicoherent monocrystalline bilayer interface with misfit dislocation spacing of ~ 1.4 nm, and APT results indicate a clean interface. Unlike the

monocrystalline patch, which was only observed on one bilayer sample, the polycrystalline OR is highly reproducible in electron beam deposition of Fe on {100} YTO.

Finally, we note that the bilayers were prepared for future He implantations and charged particle irradiations, with one objective being to experimentally observe the partitioning of He between the Fe, YTO, and associated interface. These studies will be used to inform multiscale models to predict NFA performance in fusion and fission reactor environments.

6.8 Acknowledgements

I would like to thank H. Zhou (UT) for supplying the YTO single crystal, D. Stave (UCSB) for helping with electron beam deposition, G. Steward (USCB) for help with SEM and EBSD scans, Y. Wu (USCB) for TEM imaging, P. Wells (UCSB) for APT, Y. Jiang (CSU), B. Uberuaga (LANL) and S. Valone (LANL) for discussions and insight, and G.R. Odette (UCSB) for guidance and support.

6.9 References

[1] E.A. Marquis, Appl. Phys. Lett. 93 (2008) 10–13.

[2] S. Liu, G.R. Odette, C.U. Segre, J. Nucl. Mater. 445 (2014) 50–56.

[3] V. Badjeck, M.G. Walls, L. Chaffron, J. Malaplate, K. March, J. Nucl. Mater. 456 (2015) 292–301.

[4] Y. Wu, J. Ciston, S. Kräemer, N. Bailey, G.R. Odette, P. Hosemann, Acta Mater.

111 (2016) 108–115.

[5] Y. Miao, K. Mo, B. Cui, W. Chen, M.K. Miller, K.A. Powers, V. Mccreary, D. Gross, J. Almer, I.M. Robertson, J.F. Stubbins, Mater. Charact. 101 (2015) 136–143.

[6] J. Ribis, Y. De Carlan, Acta Mater. 60 (2012) 238–252.

[7] J. Ribis, S. Lozano-Perez, J. Nucl. Mater. 444 (2014) 314–322.

[8] K. Dawson, G.J. Tatlock, J. Nucl. Mater. 444 (2014) 252–260.

[9] M. Tamura, H. Sakasegawa, K. Shiba, H. Tanigawa, K. Shinozuka, H. Esaka, Metall. Mater. Trans. A 42 (2011) 2176–2188.

[10] Y. Wu, E.M. Haney, N.J. Cunningham, G.R. Odette, Acta Mater. 60 (2012) 3456–3468.

[11] A.J. London, B.K. Panigrahi, C.C. Tang, C. Murray, C.R.M. Grovenor, Scr. Mater. 110 (2016) 24–27.

[12] R. Kasada, N. Toda, K. Yutani, H.S. Cho, H. Kishimoto, A. Kimura, J. Nucl. Mater. 367–370 A (2007) 222–228.

[13] Y. Wu, J. Ciston, S. Kräemer, N. Bailey, G.R. Odette, P. Hosemann, Acta Mater. 111 (2016) 108–115.

[14] X. Mao, K.H. Oh, S.H. Kang, T.K. Kim, J. Jang, Acta Mater. 89 (2015) 141–152.

[15] N.W. Ashcroft, N.D. Mermin, Solid State Physics, 1st ed., Harcourt College, Orlando, 1976.

[16] H. Ibach, Physics of Surfaces and Interfaces (Google eBook), 2006.

[17] D.A. Porter, K.E. Easterling, M.Y. Sherif, Phase Transformations in Metals and Alloys, 3rd ed., CRC Press, Boca Raton, 2009.

[18] S. Choudhury, D. Morgan, B.P. Uberuaga, Sci. Rep. 4 (2014) 6533.

[19] J. Brodrick, D.J. Hepburn, G.J. Ackland, J. Nucl. Mater. 445 (2014) 291–297.

[20] J.A. Aguiar, O. Anderoglu, S. Choudhury, J.K. Baldwin, A. Misra, B.P. Uberuaga, J. Mater. Sci. (2014) 0–23.

[21] T. Stan, Y. Wu, G.R. Odette, K.E. Sickafus, H.A. Dabkowska, B.D. Gaulin, Metall. Mater. Trans. A Phys. Metall. Mater. Sci. 44 (2013) 4505–4512.

Chapter 7 Fe – {110}YTO Bilayers

7.1 Introduction

As previously mentioned, some of the embedded nano-oxides (NOs) in nanostructured ferritic alloys (NFAs) have {110} $Y_2Ti_2O_7$ (YTO) planes matched with the surrounding matrix. Two of the orientation relationships (ORs) have {100}Fe//{110}YTO (face-on-edge) interfaces [1–3], but a {110}Fe//{110}TYO (edge-on-edge) OR has also been reported [4]. Thus, the two favorable Fe orientations for depositions on {110}YTO substrates are {100}Fe and {110}Fe. Also, first principles modeling indicates that NOs may have a Y/Ti cation-rich YTO termination with the matrix due to low oxygen partial pressure (PO_2) levels in the NFAs [5,6]. However, experimental alloying studies indicate that PO_2 levels may in fact be higher, in which case O-rich YTO terminations would be expected [7]. It is difficult to experimentally measure and adjust the internal PO_2 in the NFAs themselves, but the bilayer system provides experimental advantages. The YTO surface can be treated with etchants and in-situ cleaning techniques prior to Fe deposition.

The questions addressed in this chapter are: can embedded ORs, such as {100}Fe and {110}Fe, be obtained by Fe deposition on {110}YTO substrates? Do {100}Fe patches appear on {110}YTO as well? Are these patches associated with interlayers? What is a

good YTO surface treatment procedure to obtaining clean and contaminant-free interfaces? Do in-situ cleaning steps prior to deposition affect the Fe film orientation?

The experimental approach is to deposit Fe on oriented {110}YTO single crystal substrates to create surrogate mesoscopic-scale interfaces. The following sections show results from a systematic study of three cleaning procedures prior to loading the YTO substrates into the deposition systems. A second related study was done using the Palmstrom interconnected molecular beam epitaxy (MBE) system where further in-situ cleaning and surface treatments were possible while the YTO substrate was loaded in ultra-high vacuum.

7.2 Experimental

YTO single crystals were {110} oriented, wire saw cut into 2 mm thick wafers, and polished using a sequence of diamond lapping films, followed by a final 15-minute polish using 0.02 μm non-crystallizing silica suspension.

As mentioned in previous chapters, the substrate cleaning procedure may affect the Fe film orientation. Many different surface treatments steps were attempted in this study, and a select few are reported in this chapter. The substrate cleaning procedures for three of the films are summarized in Table 7.1. The “No Etch” procedure includes substrate polishing and rinsing but no chemical treatment. The “Etch + Anneal” procedure includes a 5 min etch using Aqua Regia, a mixture of nitric acid (HNO_3) and hydrochloric acid (HCl) with a molar ratio of 1:3. Following the etching and methanol cleaning, the YTO

substrate was vacuum sealed in a glass tube and annealed for 3 hrs at 800 °C. Finally, the "DI Water" procedure includes the use of cleaner de-ionized (DI) water and an Aqua Regia etch without annealing in vacuum.

Table 7.1 – Cleaning procedures for three {110}YTO substrates.

Step No.	**"No Etch"**	**"Etch + Anneal"**	**"DI Water"**
1	Colloidal Silica	Colloidal Silica	Colloidal Silica
2	Water rinse	Water rinse	DI water rinse
3	Water + 10% soap	Water + 10% soap	DI water + 10% soap
4	Water rinse	Water rinse	DI water rinse
5	Acetone rinse	AR etch for 5 min	AR etch for 5 min
6	Water rinse	Methanol for 5 min	DI water for 5 min
7	Ozone plasma clean	800 °C anneal for 1 hr	

After cleaning, each of the three substrates were loaded into an electron beam deposition system, pumped to ~$6x10^{-6}$ torr, and annealed for 1 hr at 800 °C. The Fe deposition rate was 8 nm/s for 250 s, producing layer thicknesses of ≈ 2 μm. After deposition, all of the bilayers were annealed for 1 hr at 800 °C prior to being cooled to room temperature and unloaded.

In a related study, one {110}YTO substrate was chosen for a series of in-situ surface treatment experiments in attempts to further control the YTO termination. The substrate was cleaned using the "No Etch" procedure, but the Fe films were deposited in the UCSB Palmstrom interconnected molecular beam epitaxy (MBE) system. The substrate was loaded and pumped down to ultra-high vacuum (~10^{-11} Torr) and outgassed by annealing at 700 ºC for 1 hour.

The four different in-situ surface treatment procedures are summarized in Table 7.2. The "Control" procedure did not include any surface treatments. After sample loading and outgassing, 20 nm of Fe was MBE grown at room temperature. The first 5 nm were grown slowly with a deposition rate of 0.5 Å/min, and the remaining 15 nm were grown with a faster rate of 1.35 Å/min. The sample was then annealed at 300 ºC for 1 hour to allow the film to equilibrate. An extra 200 nm of Fe was then deposited on top of the MBE-grown layer using an electron beam (E-beam) system with a rate of 2 Å/s at 300 ºC. The Fe layer (a total of 220 nm) was capped with 5 nm of E-beam grown alumina (AlO_x) to prevent Fe oxidation.

In an attempt to obtain an oxygen-rich surface termination, Ozone (O_3) gas was used to clean the substrate prior to deposition. The "Ozone" procedure involved a 20 min room temperature clean prior to 200 nm, 2 Å/s E-beam deposition at 700 ºC. Note that there may have been a Ga contamination. The film was capped with 5 nm of AlO_x.

The final two procedures were used in an attempt to get a cation termination (Y/Ti-rich) by chemically reducing the surface. The "Hydrogen" procedure involved a 30 min elemental hydrogen clean prior to 200 nm E-beam deposition at 700 ºC. The film was capped with 5 nm of Ni in an attempt to prevent charging during SEM/EBSD scanning. Finally, the "H + 2Ti" system involves the previously mentioned elemental hydrogen clean, followed by deposition of 2 monolayers of Ti to force a cation-rich surface termination. The MBE-grown Ti was deposited at 300 ºC with a deposition time of 149 s.

Similar to the previous procedures, 200 nm of E-beam Fe was deposited followed by a 5 nm AlO_x capping layer.

Table 7.2 – Summary of in-situ surface treatment steps after loading the YTO substrate.

"Control"	**"Ozone"**	**"Hydrogen"**	**"H + 2Ti"**
1 hr 700 °C anneal	1 hr 700 °C anneal	1 hr 700 °C anneal	1 hr 700 °C anneal
20 nm MBE Fe	20 min OZONE	30 min Hydrogen	30 min Hydrogen
1 hr 300 °C anneal	Ga contamination?	200 nm E-beam Fe	2 monolayers Ti
200 nm E-beam Fe	200 nm E-beam Fe	5 nm E-beam Ni	200 nm E-beam Fe
5 nm E-beam AlO_x	5 nm E-beam AlO_x		5 nm E-beam AlO_x

SEM and EBSD was performed after all seven of the procedures to obtain grain sizes and Fe orientations. TEM was performed on some of the bilayers to observe interlayers and interfacial structures. Notably, one substrate was inspected using the TEAM1 aberration-corrected TEM at LBNL. Finally, CrystalMaker was used to visualize the atomic matching of the Fe-YTO interfaces.

7.3 "No Etch" Procedure

Figure 7.1a shows a scanning electron microscope (SEM) image taken from the Fe film on a "No Etch" cleaned {110}YTO substrate. There are three types of surface topologies (marked 1, 2 and 3). Area 1 is flat and has ripples and ridges across the surface. This area covered most of the substrate surface, and coalesced as one continuous film without clearly observable grain boundaries. ~2 μm pointed grains were also observed and are marked with 2 in Figure 7.1. Some of these grains were isolated within cracks in the

large flat areas, while others were found in groups. These grains occupied a small fraction of the total area of the sample. The final topology is marked with 3 in Figure 7.1a. This ≈ 10 x 10 μm grain is smooth and flat, and is the only one found on the entire sample. It is surrounded by both type 1 and type 2 Fe film morphologies.

Figure 7.1b shows electron backscatter diffraction (EBSD) IPFZ maps taken from the area marked by a green rectangle in Figure 7.1a. Each out-of-plane crystallographic orientation is assigned a color based on the legend in the top right of Figure 7.1b. Grains with {100} surface orientations are marked with red, grains with {110} orientations are green, grains with {111} orientations are blue, and grains with {112} orientations are purple. White areas in Figure 7.1b represent locations where the EBSD patterns could not be indexed. This is often due to interference from grain boundaries, rough surface topology, or surface contamination.

Area 1 in Figure 7.1b is speckled with both green and blue. However, further analysis indicates that the blue parts were miss-indexed by the EBSD software and should be green. Thus, the large areas marked with 1 have out-of-plane orientations close to {110}. The pointed grains marked with 2 are all purple and have an orientation close to {112}. The large ~ 10 μm red grain marked with 3 is {100} oriented.

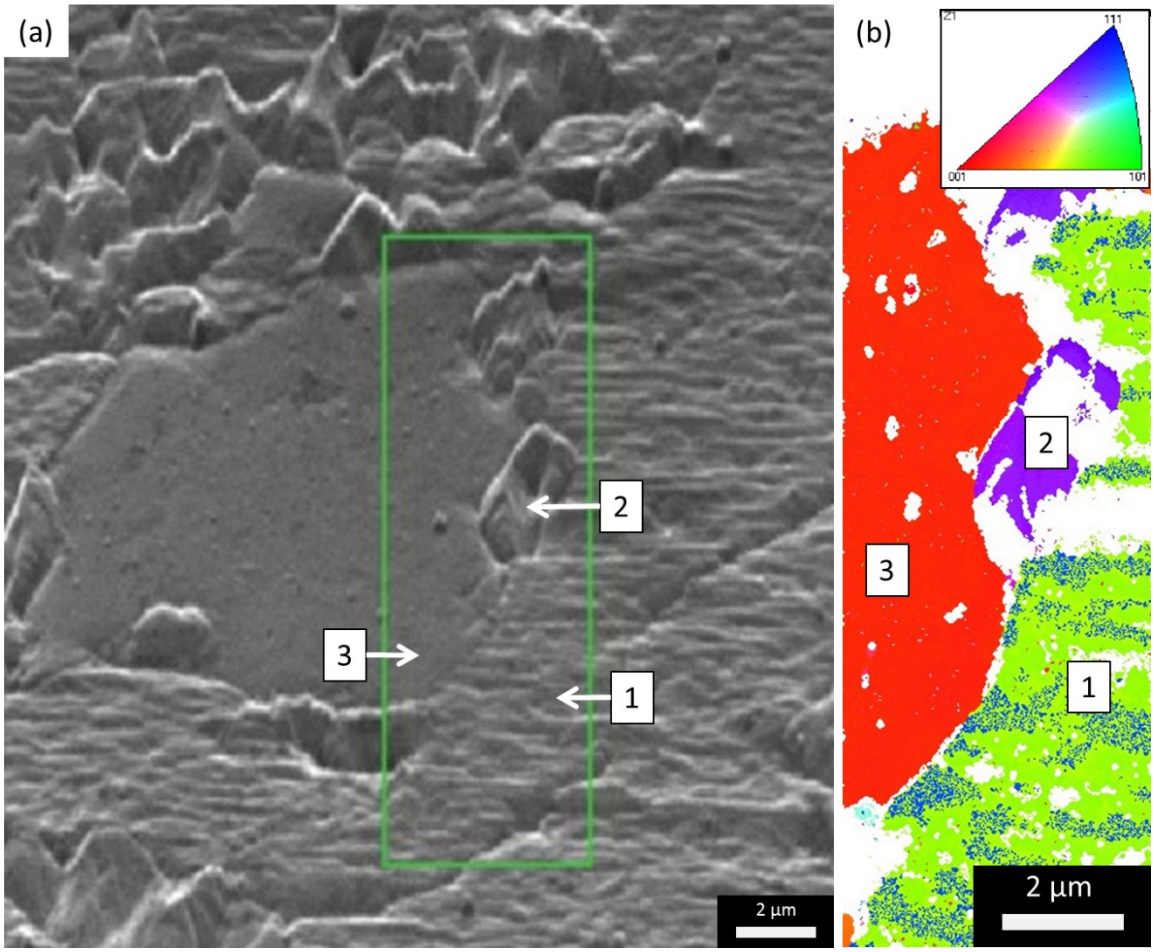

Figure 7.1 – (a) SEM image from the Fe film on the "No Etch" cleaned {110}YTO substrate. (b) EBSD image from the green square indicating out-of-plane crystallographic orientations of the Fe grains. Three surface topologies are marked with 1, 2, and 3 in both (a) and (b).

The EBSD data from Figure 7.1b is also represented as pole figures in Figure 7.2. Each part of Figure 7.2(a-d) indicates the name of the material, four pole figures representing the 111, 110, 100, and 112 reflections, and a 3D cube showing the full crystallographic orientation. The green diamonds on the pole figures indicate parallel

surface orientations, while blue hexagons show parallel in-plane orientations. Figure 7.2a shows the crystallographic orientation of the YTO substrate. The green diamond in the center of the {110} pole figure and the accompanying 3D cube indicate that the substrate was {110} oriented.

Figure 7.2b shows EBSD data from the flat part of the Fe film, referred to as area 1 in Figure 7.1. This area does not have a clear out-of-plane OR with the substrate, but is close to {110}. By observing the overlap between the hexagons in the 100 Fe pole figure and the 110 YTO pole figure, the following in-plane OR is obtained: <100>Fe//<110>YTO.

Figure 7.2c shows EBSD data from the pointed grains marked with 2 in Figure 7.1. These grains are {112} surface oriented. By overlapping the diamonds and hexagons from the YTO substrate and those from the Fe grains, the following OR is obtained: {112}Fe//{110}YTO and <111>Fe//<110>YTO. This OR has not been observed in any previous study on embedded NOs, nor on Fe depositions.

Figure 7.2c shows EBSD data from the large flat grain marked with 3 in Figure 7.1. The OR between this grain and the substrate is: {100}Fe//{110}YTO and <100>Fe//<100>YTO. Notably, this is one of the embedded ORs found by Wu et al. [1]. This result is significant since it shows that some surrogate interfaces can be created to have the same ORs as those found in embedded NOs.

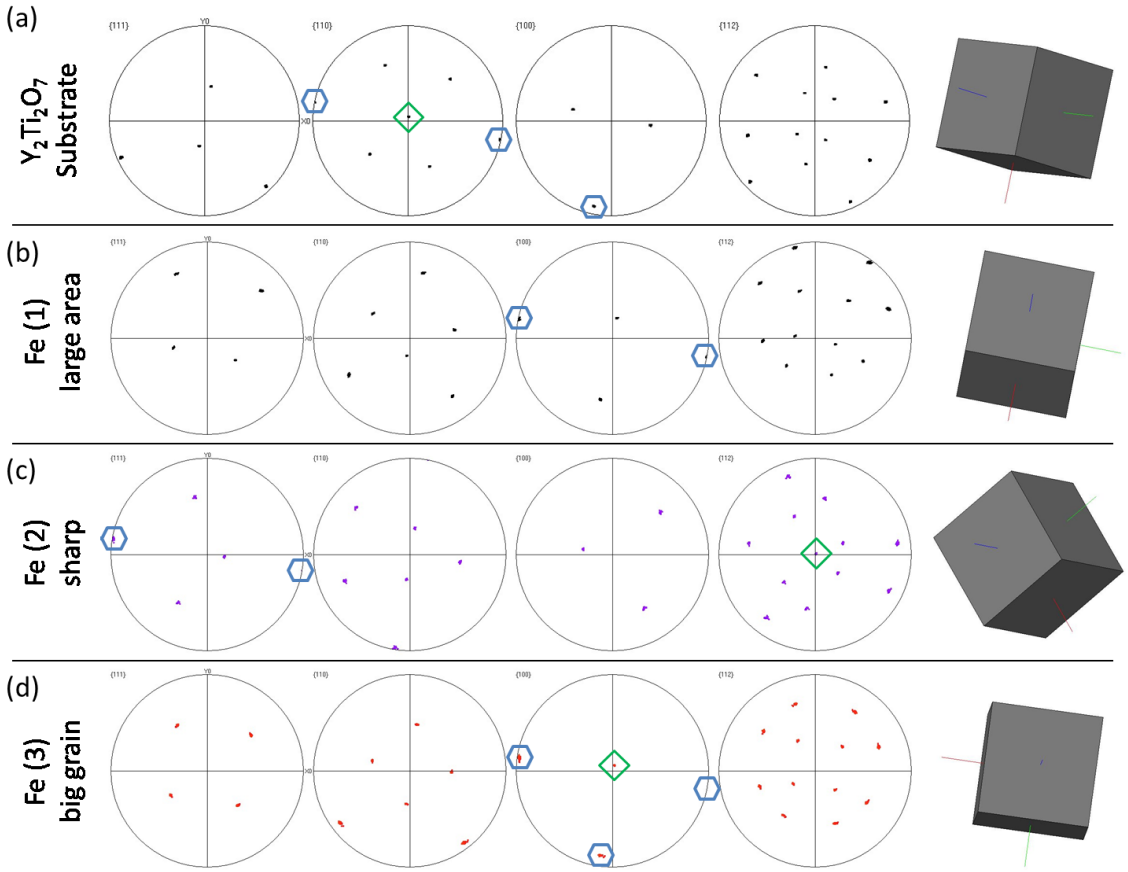

Figure 7.2 – EBSD pole figures from (a) the {110}YTO substrate, and (b – d) the three types of Fe grains. Green diamonds indicate parallel surface orientations while blue hexagons show parallel in-plane orientations. The cubes next to the pole figures represent the full 3D orientation.

Scanning Transmission Electron Microscopy (STEM) was carried out on a Focused Ion Beam (FIB) lift-out cross section of the 10 μm grain to observe the interface. The scan is shown in the center of Figure 7.3. A sketch of the Fe and YTO unit cells is shown on the left of Figure 7.3. The STEM image shows the Fe layer in light gray at the top, and the YTO substrate at the bottom. Fe strain in the first deposited layers and/or a thin metallic

oxide interlayer is visible in the dark area at the interface. Note that a visible interlayer was not present in the {100}Fe grain.

CrystalMaker was used to visualize the interface by matching the oriented Fe and YTO lattices. The results are shown in the right side of Figure 7.3. Fe, Ti, Y, and O are represented as orange, blue, green and red spheres, respectively. The light blue and dark green circles indicate Ti and Y atomic columns which run through the page, respectively. The purple circles indicate columns of mixed Y and Ti. The contrast in the STEM image allows for column identification, where the brighter substrate spots are indicative of Y columns, the darker spots are Ti columns, and the medium intensity spots are columns of mixed Y and Ti. Note that STEM cannot detect O and thus the YTO chemistry at the interface is not clear.

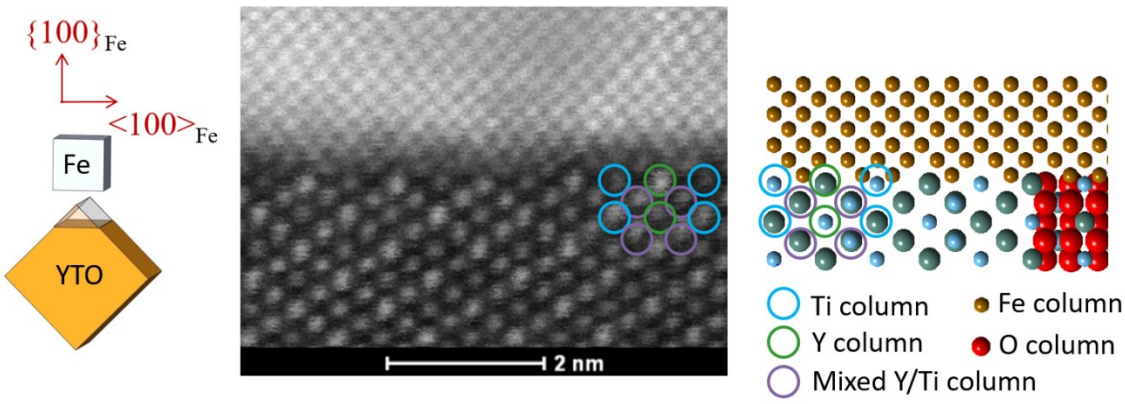

Figure 7.3 – STEM image from the 10 µm {100}Fe grain. A sketch of the Fe and YTO unit cells is shown on the left. A CrystalMaker rendering of the interface is shown on the right.

7.4 "Etch + Anneal" Procedure

A second {110}YTO substrate was etched with Aqua Regia for five minutes, then annealed for one hour in air at 800 ºC prior to Fe deposition. The EBSD map and associated legend are shown in Figure 7.4a. The Fe film has two surface morphologies. The left side has ~1 μm coalesced grains, while the right side has >3 μm grains. As shown with pole figures in Figure 7.3b, the grains on the left have strong epitaxial {100}Fe texturing. This is the same OR that was found for the 10 μm grain in Figure 7.1 and for embedded NOs [1]. The right side shows a polycrystalline film with many grain orientations such as {111}Fe shown in blue and {112}Fe shown in purple (Figure 7.4c). The streaks in the pole figures indicate an axiotaxial OR with the substrate. The {100}YTO substrate planes (which are not normal to the sample surface) are nearly parallel to the {110}Fe planes (also not normal to the interface plane). The pole figures have two-fold symmetry, as expected for depositions on well-oriented {110}YTO substrates.

There are four types of thin film texture: random, fiber, axiotaxial and epitaxial. Random texture indicates that grains have no ORs with the substrate, and all possible orientations are present. Fiber texture means that grains have a preferred out-of-plane texturing perpendicular to the substrate, but no favored in-plane orientations. Axiotaxy is a form of fiber texture where grain planes align with substrate planes that are not surface normal, while other families of planes are randomly distributed. Axiotaxy requires that grain and substrate planes have similar spacings along the interface. In some systems, this

periodic interface possibility has a lower energy bond configuration, despite the grains having different interface structures and out-of-plane texturing. Finally, the strongest OR is epitaxial where grains are fully in-plane and out-of-plane aligned with the substrate. Axiotaxy is revisited in later sections.

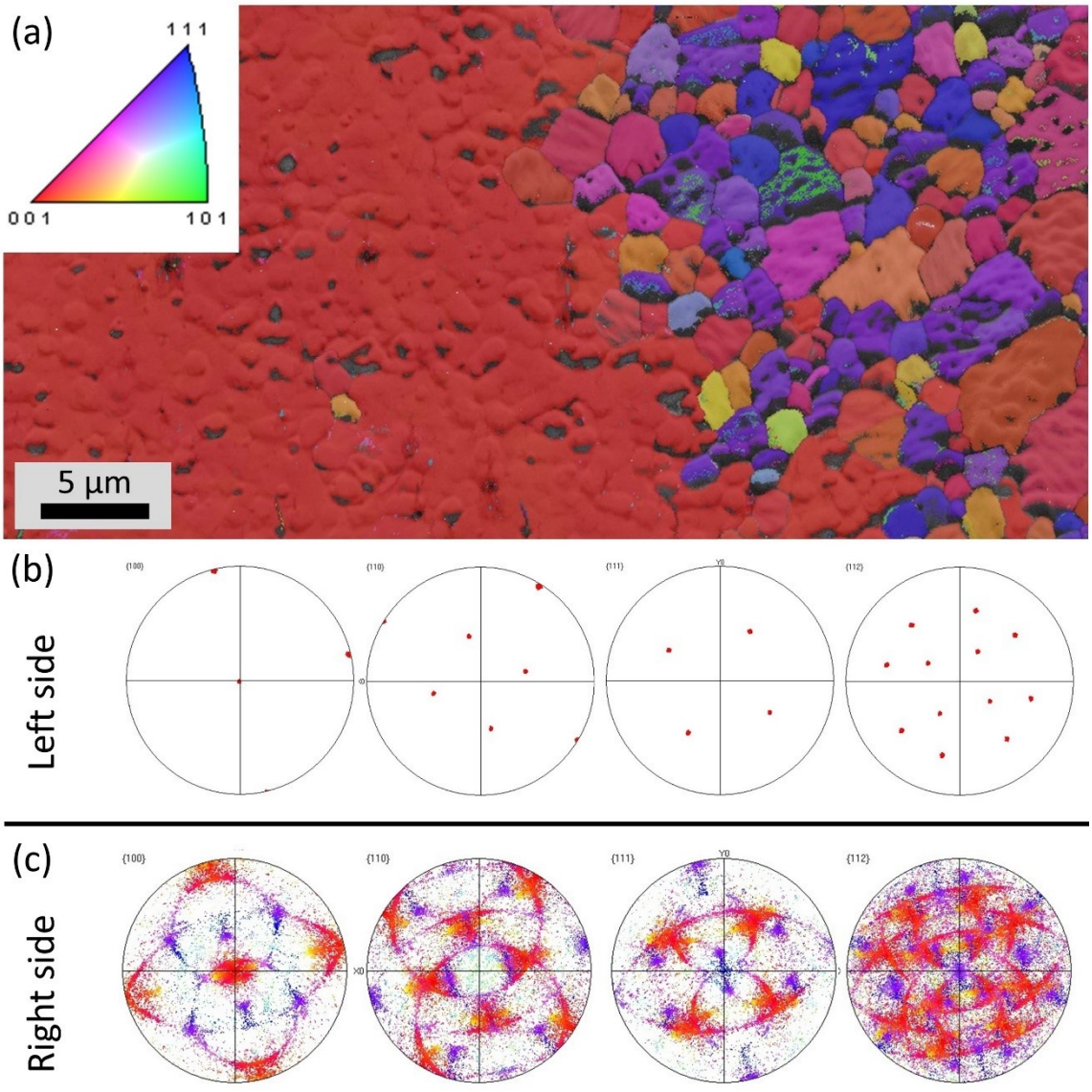

Figure 7.4 – (a) EBSD map of Fe film on the "Etch + Anneal" {110}YTO substrate. The left side is a continuous film while the right side is polycrystalline. (b) Pole figures from the left side indicating {100}Fe epitaxial texturing. (c) Pole figures from the grains on the right side indicating axiotaxial texturing.

As previously mentioned, the epitaxial {100}Fe oriented side is of special interest as it has an OR found for embedded NOs. A cross-section TEM image is shown in Figure 7.5a where Fe is the lighter area with the {100} direction pointing upwards. The Fe-YTO interface has a very dark interlayer that varies in thickness, up to ~ 10 nm. EDX line profiles were used to measure chemistry differences in the sample. The line scan location is marked with a green line in Figure 7.5a, and the resulting profile is shown in Figure 7.5b. In this section of the bilayer, the interlayer measures 2.67 nm thick. There is a gradual decrease in Fe content, through the interlayer, which stops at the YTO surface. O levels gradually increase with proximity to the substrate. Notably, there is a spike in Ca at the interlayer. Contaminant Si and Ca may be due to residual colloidal silica polishing and water rinsing, respectively. Thus, the {100}Fe orientation of interest is likely due to the presence of a contaminant interlayer.

TEM was also done on grains from the axiotaxially textured right side of the sample. The interfaces were clean and did not have an observable interlayer. The results are not included here for brevity, and because Section 7.5 on "DI Water" cleaning contains similar and higher quality results.

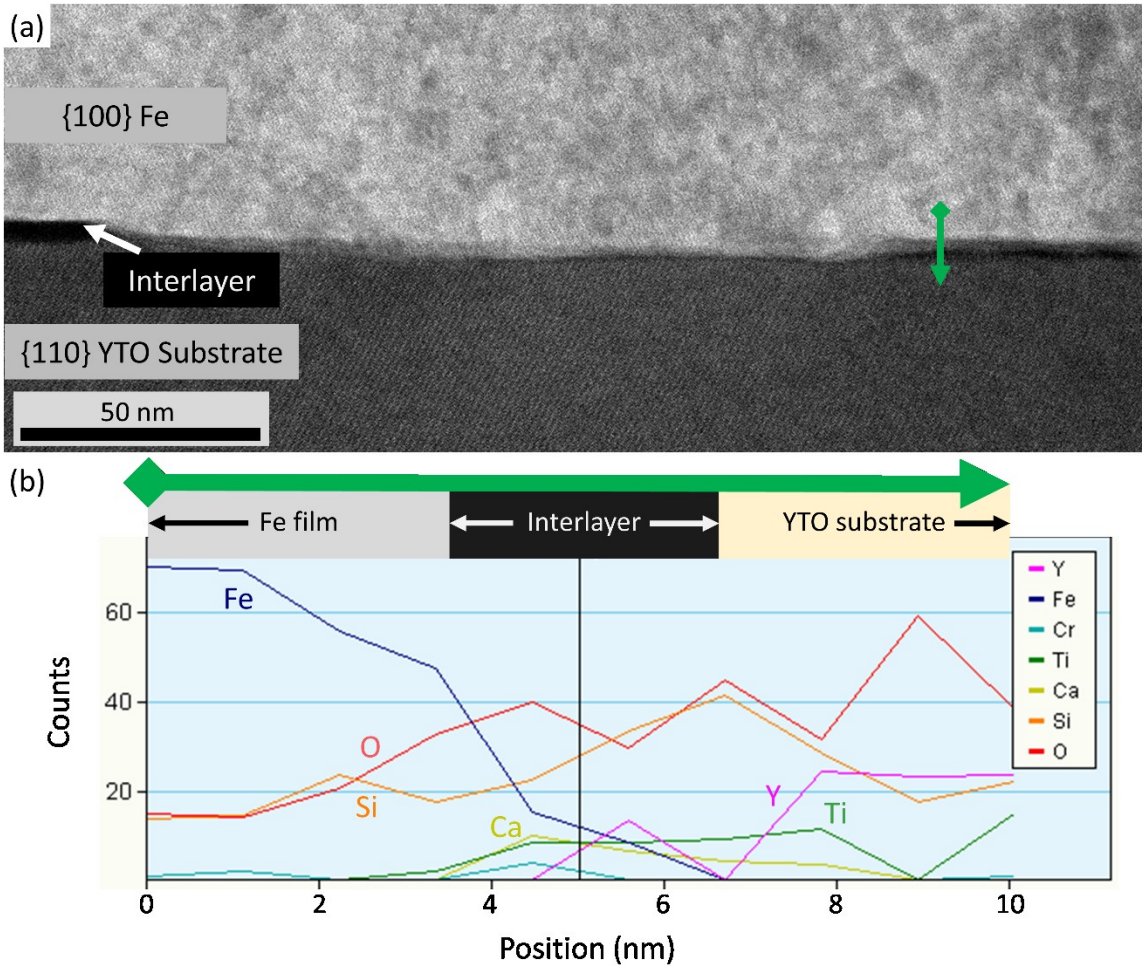

Figure 7.5 – (a) TEM image of the {100} Fe section from the "Etch + Anneal" bilayer. The location of the EDX scan across the dark interlayer is shown in green. (b) EDX line profile showing a 2.5 nm thick Ca-enriched interlayer at the Fe-YTO interface.

7.5 "DI Water" Procedure

The "DI Water" procedure proved to be the best way to prepare substrates for Fe deposition. Figure 7.6a shows an EBSD band contrast image, indicating the location of ~ 2 nm grains. The IPFZ map in Figure 7.6b is colored different shades of red indicating

texturing close to {105}Fe. The Euler map in Figure 7.6c shows multiple colors, better revealing presence of grains. The pole figures and representative 3D renderings for the Fe film and YTO substrate are shown in Figure 7.6d and Figure 7.6e, respectively. Note that the bottom right rims of the <100> Fe and <100> YTO pole figures have spots at the same location, indicating an in-plane OR of: <100>Fe//<100>YTO.

The Fe pole figures in Figure 7.6d indicate a more restricted version of the axiotaxial OR observed in the polycrystalline side of the "Etch + Anneal" bilayer (Figure 7.4). The streaks are not as widespread, and the two-fold symmetry is no longer seen. This is likely due to the substrate being slightly miscut which suppressed the growth of some Fe orientations. Further, the <110> Fe pole figure has a non-streaked spot in the top-right quadrant. This is the off-normal rotation axis for the axiotaxially oriented Fe grains.

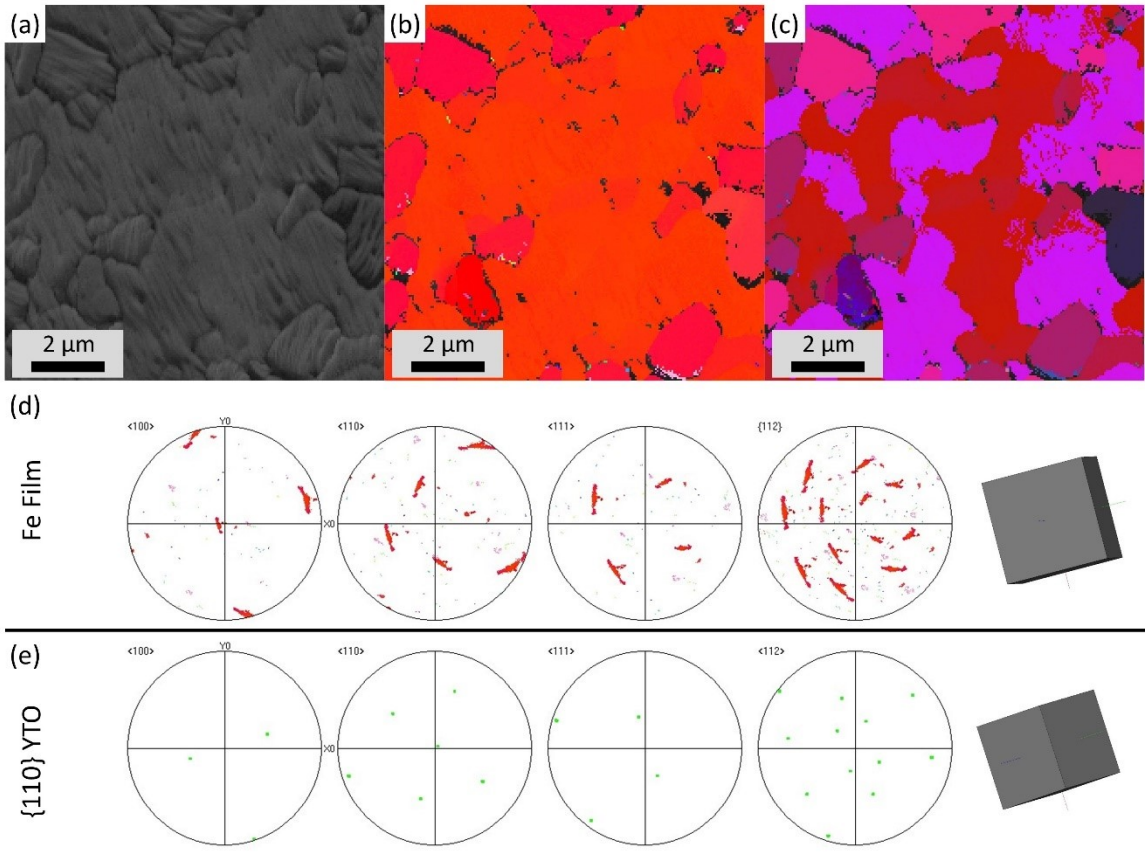

Figure 7.6 – EBSD (a) band contrast, (b) IPFZ map and (c) Euler map of the Fe grains on "DI Water" cleaned substrates. Pole figures and 3D renderings from the Fe film and the YTO substrate are shown in (d) and (e), respectively.

To better illustrate the axiotaxial OR, the Euler map from Figure 7.6c is reproduced in Figure 7.7 along with 3D renderings of the Fe grains. The five orientations are nearly identical, and rotations about the <110>Fe off-normal axis (green dots) lead to streaks in the pole figures. The grains all have a different out-of-plane orientation, close to {105}Fe, but share the exact same off-normal <110>Fe axis.

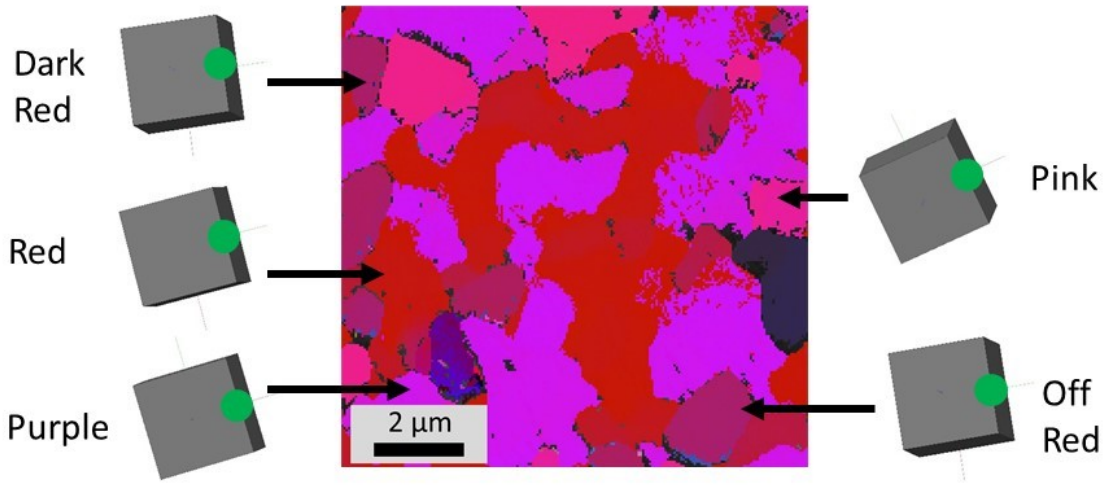

Figure 7.7 – Euler map of the Fe film on the "DI Water" cleaned substrate showing five of the axiotaxially textured Fe grains. Green dots indicate the <110>Fe off-normal rotation axis.

High resolution STEM images were obtained from the Fe-{110}YTO "DI Water" cleaned bilayer using the aberration corrected TEAM1 instrument at LBNL. Figure 7.8a shows a section of the interface as viewed through the <100>Fe//<100>YTO zone axis. Both the Fe and YTO lattices are resolved. The interface is clean without a contaminant interlayer. In Figure 7.8a, {110} Fe and {100} YTO planes are shown in green and purple, respectively. The interface is characterized as coherent because the Fe and YTO lattices are perfectly matched. Figure 7.8b shows a CrystalMaker rendering of the bilayer better showcasing the coherent matching. The axiotaxial rotation axis is shown with a blue arrow. All of the grains in this bilayer maintain the coherent lattice matching, but are slightly rotated about the non-surface normal <110> Fe axis.

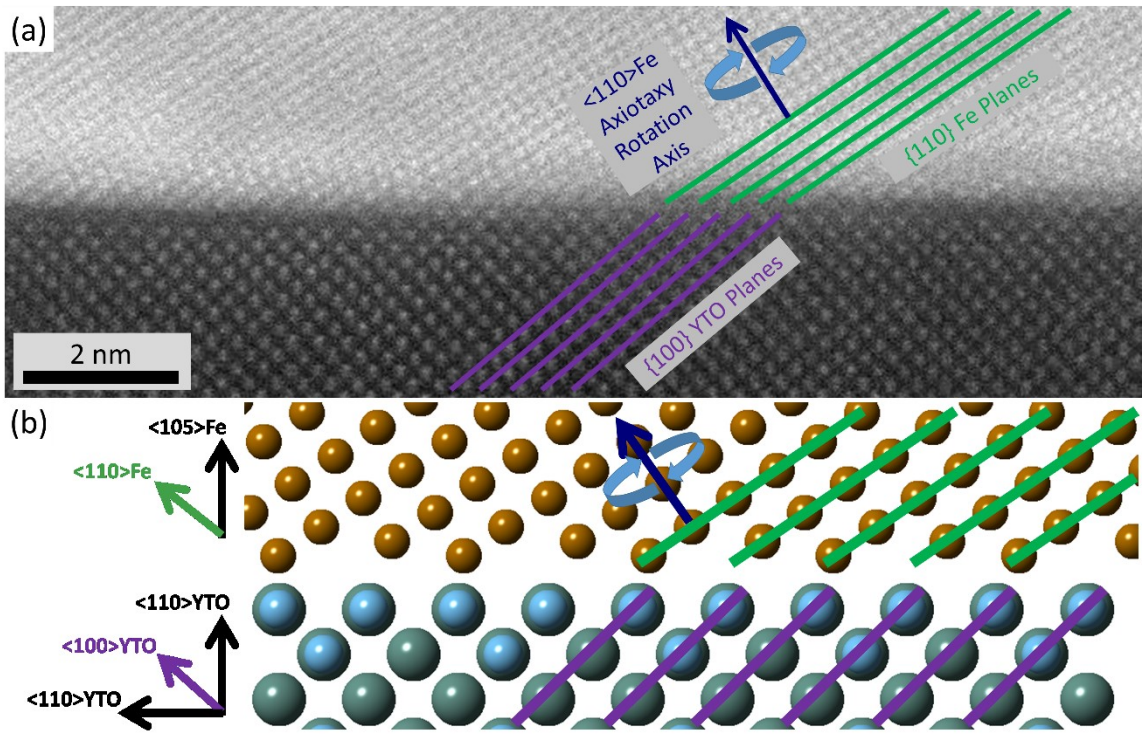

Figure 7.8 – (a) High resolution STEM image of the Fe film on "DI Water" cleaned YTO showing {110}Fe planes in green, {100}YTO planes in purple, and the axiotaxy rotation axis in blue. (b) CrystalMaker rendering of the interface showing a coherent interface.

7.6 In-Situ Cleaning

The following results are from a {110}YTO substrate that was cleaned using the "No Etch" procedure prior to loading into the Palmstrom interconnected MBE system. Figure 7.9 shows IPFZ maps and PFs from the four in-situ procedures mentioned in Table 7.2. The four depositions were on the exact same substrate. After each deposition and SEM/EBSD scan, the Fe film was removed and the YTO was re-polished prior to re-loading.

Figure 7.9a shows IPFZ maps and PFs from the Fe film on the "Control" sample. The ~200 nm wide Fe grains are mostly colored different shades of red. The {105}Fe texturing, streaks in the PFs and two-fold symmetries are indicative of the same axiotaxial OR seen in the "Etch + Anneal" deposition. The lower temperature and slower deposition rate led to smaller Fe grains, but the crystallographic orientations did not differ compared to the E-beam deposited bilayers.

Figure 7.9b shows IPFZ maps and PFs from the "Ozone" cleaned sample. The grains are mostly colored blue, indicative of {111} Fe texturing. These orientations, although more localized here, were also observed in the "Etch + Anneal" deposition. The OR is close to {111}Fe//{110}YTO and <110>Fe//<100>YTO. A few grains with the desired {100}Fe orientation were also observed. This bilayer was not studied further as a Ga contamination was detected which likely affected the Fe orientations. Although outside the scope of this experiment, the results are included here as they may be useful for other studies of the Fe-Ga-YTO system.

IPFZ maps and PFs from the in-situ "Hydrogen" cleaning and the "H + 2Ti" procedure are shown in Figure 7.9c and Figure 7.9d, respectively. Note that despite slight differences in EBSD scan conditions, the PFs look nearly identical to each other, and similar to the "Control" PFs in Figure 7.9a. Thus, the hydrogen cleaning and 2 monolayers of Ti did not have a significant effect on the Fe orientation.

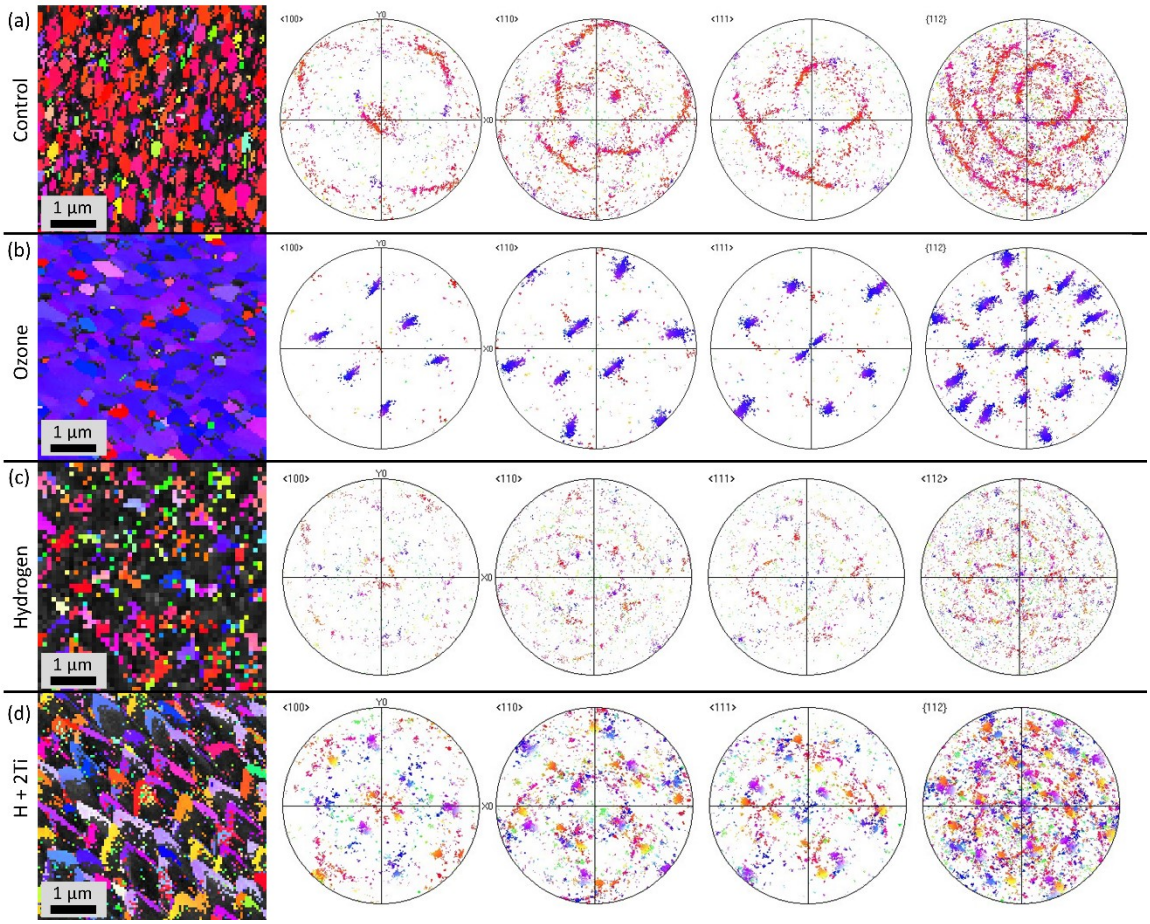

Figure 7.9 – IPFZ maps and pole figures for depositions using (a) “No Etch”, (b) OZONE, (c) Hydrogen and (d) H + 2Ti substrate treatments.

7.7 Discussion

Fe deposition on un-etched {110}YTO substrates yielded flat areas with out-of-plane ORs close to {110}Fe, and pointed {112}Fe grains. There was a single ~10 micron {100}Fe grain with an OR reported for embedded NOs. Fe deposition on Aqua Regia etched and annealed {110}YTO led to two types of film morphologies. The continuous

film on the left side of the sample was {100}Fe textured and had the same OR as the 10 micron grain in the un-etched sample. The polycrystalline side had many Fe orientations including {111}Fe and {112}Fe. The streaks in the PFs indicate axiotaxial texturing. The "DI Water" cleaning procedure yielded interlayer-free Fe-YTO interfaces with few streaks in the PFs, and without any {100}Fe grains.

Based on the previously mentioned three cleaning procedures, it is clear that {100}Fe grains are usually accompanied by an interlayer. For the bilayer fabricated with the "Etch + Anneal" procedure, the large {100}Fe area had a Ca-rich film at the interface that varied in size, up to ~ 10 nm. The interlayer is believed to be caused by left-over Si particles from the colloidal silica polish, or from Ca particles that were in the water rinse. Parts of the {100}Fe layer did not have an observable interlayer, but it is possible that the film nucleated at the contaminated sites and then grew over the substrate, or restructured during the high temperature annealing. The "DI Water" procedure proved to be the most efficient in removing contaminants and yielding clean Fe-YTO interfaces.

An in-situ study was performed to change the YTO surface chemistry prior to deposition. The slower E-beam growths at ultra-high vacuum in the MBE interconnected system led to much finer grain sizes (~200 nm) compared to the conventional E-beam growths (~2 μm). Neither the Ozone cleaning, nor the Hydrogen and 2 Ti monolayer procedure led to orientations that were different from what was observed in the E-beam. The in-situ cleaning procedures did not lead to {100}Fe grains.

The absence of {100}Fe in the in-situ study indicates that for bilayers, the orientation is likely due to contaminants. However, {100}Fe//{110}YTO interfaces are observed for embedded NOs. This study suggests that the face-on-edge OR is seen in NFAs is primarily due to strain in the very small ~ 2.5 nm embedded NOs, not necessarily interfacial chemistry. A study by Wu et al. [1] reported that NOs have compressive strains up to 9.1%. As expected, the strains decrease with increasing particle size. The compressed YTO lattices allow for coherent matching at {100}Fe//{110}YTO interfaces.

For Fe-{110}YTO bilayers, the substrates are very large (~2 mm) and unstrained prior to deposition. Therefore, lattice misfit dislocations and strains would be expected in the growing Fe layer. However, for the Fe-{110}YTO bilayer system, the Fe film does not compensate for lattice mismatch through the inclusion of misfit dislocations, but through a lattice rotation away from {100}Fe to {105}Fe. The 11.3° inclination allows for a near-perfect lattice matching between off-normal {110}Fe planes and off-normal {100}YTO planes. This coherent interface matching is favored over all other orientations, including conventional epitaxy. Grain rotations about the off-normal <110>Fe direction leads to axiotaxial texturing, and the streaks observed in pole figures. If the {110}YTO substrate lattice were compressed as it is for small embedded NOs, it is possible that the Fe film orientation would also approach {100}.

7.8 Conclusions

In conclusion, a systematic study was done to investigate the structures, ORs, and chemistries of Fe films on {110}YTO substrates. In some depositions, {100}Fe films with a favorable OR as seen in embedded NOs was obtained. However, this orientation was usually accompanied by a contaminant interfacial layer. The use of DI water and careful rinsing steps proved to be the beast procedure for obtaining clean Fe-YTO interfaces.

The effects of YTO substrate chemical termination were studied using in-situ cleaning methods. Ozone was used to oxidize the YTO surface, while hydrogen cleaning was used to reduce the surface. Further, 2 monolayers of Ti were deposited prior to Fe deposition to force a cation-rich termination. None of the in-situ treatments yielded the {100}Fe texturing observed in embedded NOs. This implies that the cube-on-edge {100}Fe//{110}YTO embedded interface is largely due to lattice matching effects, not chemical effects.

In all cases, the dominant Fe film orientation was axiotaxial with off-normal {110}Fe planes parallel to off-normal {100}YTO planes. The 11.3° inclination away from {100}Fe texturing allowed for a fully coherent interface between the Fe and YTO. Rotations about the <110> direction lead to streaks observed in pole figures. If the {110}YTO substrate could be strained, it is possible that the Fe orientations would also approach {100}Fe, as seen in embedded NOs.

7.9 Acknowledgements

I would like to thank D. Stave (UCSB) for helping with electron beam deposition, T. Brown (UCSB), N. Wilson (UCSB) and C. Palmstrom (UCSB) for depositions using the interconnected MBE system, G. Steward (UCSB) for help with SEM and EBSD scans, Y. Wu (UCSB) and J. Ciston (LBNL) for help with TEM imaging, R. Kurtz (PNNL) for discussions regarding axiotaxy, and T. Yamamoto (UCSB) and G.R. Odette (UCSB) for guidance and support.

7.10 References

[1] Y. Wu, J. Ciston, S. Kräemer, N. Bailey, G.R. Odette, P. Hosemann, Acta Mater. 111 (2016) 108–115.

[2] Y. Miao, K. Mo, B. Cui, W. Chen, M.K. Miller, K.A. Powers, V. Mccreary, D. Gross, J. Almer, I.M. Robertson, J.F. Stubbins, Mater. Charact. 101 (2015) 136–143.

[3] V. Badjeck, M.G. Walls, L. Chaffron, J. Malaplate, K. March, J. Nucl. Mater. 456 (2015) 292–301.

[4] K. Dawson, G.J. Tatlock, J. Nucl. Mater. 444 (2014) 252–260.

[5] L. Yang, Y. Jiang, Y. Wu, G.R. Odette, Z. Zhou, Z. Lu, Acta Mater. 103 (2016) 474–482.

[6] Y. Jiang, L. Yang, Y. Jin, G.R. Odette, (2014) 163.

[7] G.R. Odette, JOM 66 (2014) 2427.

Chapter 8 Room Temperature He Implantations

8.1 Introduction

Neutron irradiation along with other synergistic effects can lead to void swelling, embrittlement and irradiation creep [1–3]. Managing transmutation-produced helium is a grand challenge for turning the promise of C-free fusion power into a reality. Nanostructured ferritic alloys (NFAs) are promising candidate structural materials, which are dispersion strengthened by an ultrahigh density of Y-Ti-O nano-oxides (NOs) averaging ≈ 2.5 nm in diameter, with volume fractions of order 0.5% [1–3]. NOs, significantly, trap otherwise highly damaging helium in harmless nm-scale interface bubbles [1–3], thereby preventing the formation of larger voids. Understanding the characteristics of the NO-bubble association is important to developing, qualifying and optimizing NFAs. Further, first principles models indicate that He enters the $Y_2Ti_2O_7$ (YTO) NOs prior to nucleating bubbles [4,5]. This phenomenon has not been experimentally observed.

The questions addressed in this chapter are: What are the activation energies of different He trapping sites in Fe and YTO? Will He diffuse into the YTO substrate if it is room-temperature implanted only into the Fe layer of a bilayer? Given the implantation

conditions, what are the resulting He bubble sizes and number densities in Fe, YTO, and associated interface? Are bubbles at the Fe-YTO interface periodically spaced?

There are two experimental approaches in this study. The first is a thermal desorption spectroscopy (TDS) study to extract room-temperature implanted He from Fe and YTO and obtain the activation energies for the two materials. The second approach is to characterize the bubble formation in a room temperature He implanted Fe-{110}YTO bilayer. The mesoscopic-scale Fe-YTO interface may not have the exact same interfacial characteristics as those found for embedded NOs, but characterization and analysis of Fe-YTO bilayers will help develop and improve current first principles and atomic interface models, and help predict NFA performance in fusion reactor conditions.

8.2 Experimental – TDS

Three single crystals were prepared for the TDS study (two YTO and one Fe). The first YTO crystal was 5° miscut from {111} to mitigate the effects of channeling, and termed "{111}YTO_miscut". The second YTO crystal was well oriented to have a {111} surface and termed "{111}YTO_new". Both crystals were polished using a sequence of diamond lapping films, followed by a final 15-minute polish using 0.02 μm non-crystallizing silica suspension. After the silica polish, the substrate was rinsed with running deionized (DI) water, followed by a sequential series of 5 min sonic bath treatments in: 10 vol% Micro-Organic soap and 90 vol% DI water, acetone, isopropanol, and finally a DI water rinse. The Fe single crystal was cut and polished at ORNL.

All three single crystals were subsequently loaded, implanted, and TDS measured at ORNL. He was implanted using a 10 keV beam to a fluence of $7x10^{14}$ He/cm^2, flux of $9x10^{12}$ He/cm^2/s, and total implantation time of ~6 min. The TDS measurements were done by heating the samples to ~1400 °C at a rate of 0.5 °C/s, for a total of ~45 min.

8.3 Experimental – Bilayer

To fabricate the bilayer, a YTO single crystal was {110} oriented and a 2 mm thick wafer was cut using a wire saw. The substrate was polished using a sequence of diamond lapping films, followed by a final 15-minute polish using 0.02 μm non-crystallizing silica suspension. The "No Etch" substrate cleaning procedure was used includes substrate polishing but no chemical treatment. After the silica polish, the substrate was rinsed with running deionized (DI) water, followed by a sequential series of 5 min sonic bath treatments in: 10 vol% Micro-Organic soap and 90 vol% DI water, acetone, isopropanol, and finally a DI water rinse.

The Fe film was deposited in the UCSB Palmstrom laboratory interconnected molecular beam epitaxy (MBE) system. The {110}YTO substrate was first inserted into the system and pumped to ultra-high vacuum (~10^{-11} Torr). The sample was then outgassed by annealing at 700 ^{o}C for 1 hour. The first 20 nm of Fe were MBE grown at room temperature. Of that 20 nm, the first 5 nm was grown slowly with a deposition rate of 0.5 Å/min, while the remaining 15 nm was grown with a faster rate of 1.35 Å/min. The bilayer was then annealed at 300 ^{o}C for 1 hour to allow the film to equilibrate. In a different

section of the Palmstrom interconnected system, an extra 180 nm of Fe was then deposited on top of the MBE-grown layer with a rate of 2 Å/s at 300 ºC. The 200 nm Fe layer was capped with 5 nm of electron beam grown AlO_x to prevent Fe oxidation. To prevent He from escaping the bilayer, the sample was coated with 9 nm of Pt on all sides using an Oxford FlexAL atomic layer deposition (ALD) system. In summary, the sample is composed of ~2 mm thick {110}YTO, 200 nm Fe, 5 nm AlO_x capping, and 9 nm Pt encapsulation.

The sample was He implanted at room temperature using a 25 keV ion beam using a Zeiss ORION NanoFab microscope at UC Berkeley. A 10 pÅ He beam was rastered over a 10 x 10 μm area, with the sample tilted at 7º to prevent channeling, for a total dose of $4x10^{15}$ He/cm^2, dose rate of $6.25x10^{13}$ He/(cm^{2}s), and an implantation time of 64 seconds. Stopping and Range of Ions in Matter (SRIM) simulations indicate a peak He concentration of ~4000 appm at a depth of 110 nm into the Fe film (halfway through the Fe), and a total implantation range of ~200 nm, roughly the same as the total Fe film thickness (blue curve in Figure 8.1). If all of the implanted He were uniformly distributed throughout the Fe film, the average concentration would be 2100 appm He. The damage profile (purple curve in Figure 8.1) has a peak of ~0.14 dpa at a depth of ~80 nm. On average, the He implantation produced ~35 vacancies for each He atom.

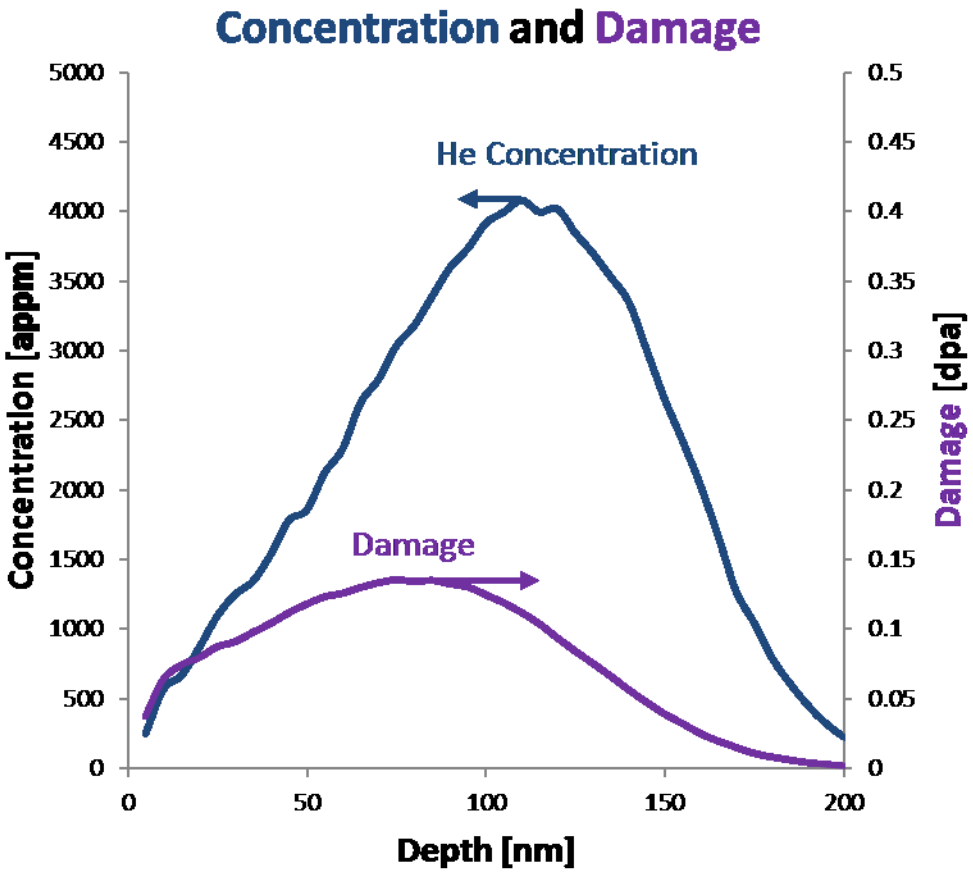

Figure 8.1 – SRIM simulated He implantation profile (blue) and damage profile (purple) for 25 keV He into Fe.

8.4 Thermal Desorption Spectroscopy

Thermal desorption spectroscopy was used to characterize the energetics of He trapping in single crystal Fe and YTO. A dose of $7x10^{14}$ He/cm^2 He was implanted into the single crystals at room temperature. The samples were then heated at a rate of 0.5 °C/s to

release the He. The spectra shown below are plotted on a He desorption rate versus temperature scale. The activation energy is related to the temperature though [6–8]:

$$\ln\left(\frac{\beta}{T^2}\right) = -\frac{E}{k_b T} + \ln\left(\frac{f k_B}{E}\right)$$

β is the linear temperature ramping (0.5 °C/s), T is temperature, E is the activation energy of a trapping site, k_B is the Boltzmann constant, and f is the jump frequency ($1x10^{13}$/s). In the spectra, the different peaks correspond to activation energies for different sites. Taller peaks indicate that more He was released from the site.

Figure 8.2 shows the TDS results for He in single crystal Fe. Cluster dynamics models are available for He in Fe [7,8], thus the activation energies can be related to different He-vacancy clusters in Fe. The spectrum shows five peaks. The small peak at ~ 75 °C is due to surface contaminations and was not analyzed. The 445 °C peak corresponds to an activation energy of 2.08 eV, and signifies He released from clusters composed of 3 He atoms and 1 vacancy (He_3V_1) type clusters. These also include clusters of He_6V_2, He_9V_3, etc. The 745 °C peak corresponds to an activation energy of 2.98 eV, and signifies HeV, HeV_2 and He_3V_2 type clusters. Overlapped with the 745 °C peak, there is a smaller peak present at 806 °C (3.17 eV). This peak is associated primarily with HeV type clusters. Finally, there is a spike at 910 °C due to the Fe phase transformation from bcc α to fcc γ. This peak was also used to calibrate the TDS measurements.

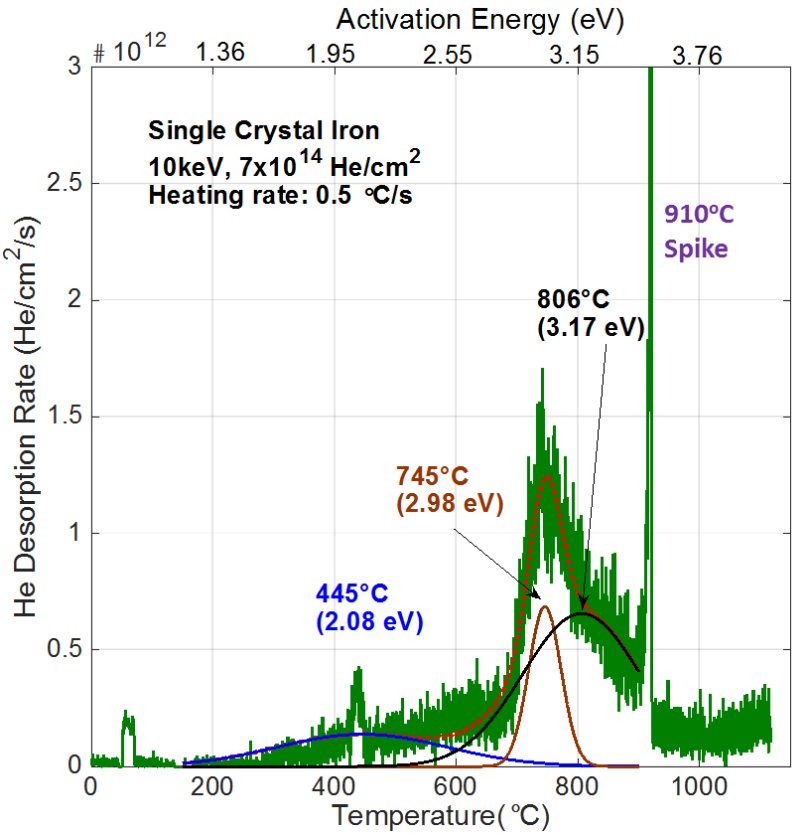

Figure 8.2 – TDS spectrum of He in single crystal Fe. Plot courtesy of X. Hu.

The TDS spectrum for He in single crystal YTO_miscut is shown in Figure 8.3. Cluster dynamics models are not yet available for He in YTO, thus only the activation energies could be obtained. The small peak at 350 °C in Figure 8.3 is likely due to surface contaminations and was not analyzed. There are two overlapping peaks at 424 °C and 521 °C which correspond to activation energies of 2.02 eV and 2.31 eV, respectively. Finally, there is a peak at 850 °C (3.3 eV) which is not expected in oxides, and may be an artifact.

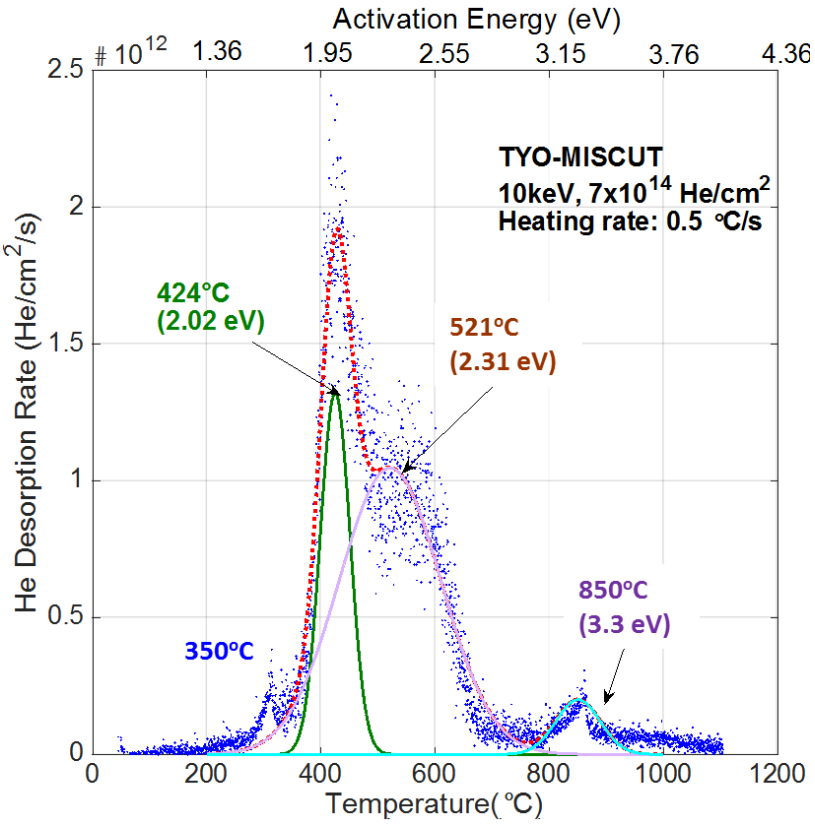

Figure 8.3 – TDS spectrum of He in single crystal YTO. Plot courtesy of X. Hu.

The spectra for the two YTO single crystals (red and blue), and the Fe single crystal (green) are overlapped and plotted together in Figure 8.4. Clearly, the peaks from the YTO are at lower temperatures than those in Fe. Thus, He is more weakly bound to the YTO structure, diffuses faster, and is more easily desorbed from YTO than from Fe. Overall, the largest peak in YTO (2.02 eV) is ~ 1 eV smaller than the largest peak in Fe (3.17 eV).

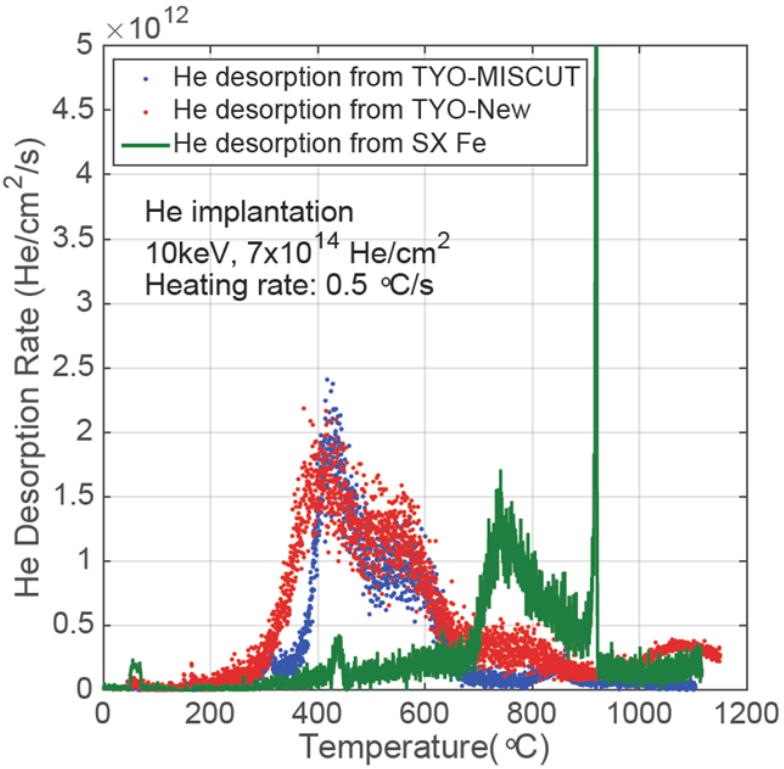

Figure 8.4 – Overlapped TDS spectra for He in single crystal Fe and two single crystals of YTO. Plot courtesy of X. Hu.

8.5 EBSD Characterization

Figure 8.5 shows EBSD data from the Fe film on {110}YTO. Figure 8.5a is an EBSD band contrast (BC) image showing the Fe grain shapes. The sub-micron grains range in size from ~20 nm to ~200 nm. Figure 8.5b shows an EBSD inverse pole figure (IPF) map depicting the out-of-plane crystallographic orientation of the Fe grains. Most of the grains are colored with different shades of red, indicating textures close to {100}Fe. Figure 8.5c shows the same data as Figure 8.5b but represented as Euler maps indicating

the full orientation of the Fe grains. The large variation in coloring indicates no preferred in-plane orientation.

Figure 8.5d shows four pole figures (<100>, <110>, <111> and <112> reflections) of the data from the IPF map in Figure 8.5b, colored according to the out-of-plane grain orientation (IPFZ). The streaks in the pole figures (PFs) indicate the axiotaxial texturing that is commonly seen for Fe depositions on {110}YTO, and are further seen in the contour PFs in Figure 8.5e. This texturing is characterized by the alignment of planes in the Fe grain and in the YTO substrate that lie off-normal to the sample surface. The red spot in the <110>Fe PF in Figure 8.5e indicates a high concentration of aligned planes. PFs from the {110}YTO substrate are shown in Figure 8.5f. The off-centered green spot in the <100>YTO PF overlaps with that seen for <110>Fe, but not at the same distance away from the center. Last, Figure 8.5g shows 3D renderings of some selected Fe grains, and the {110}YTO substrate.

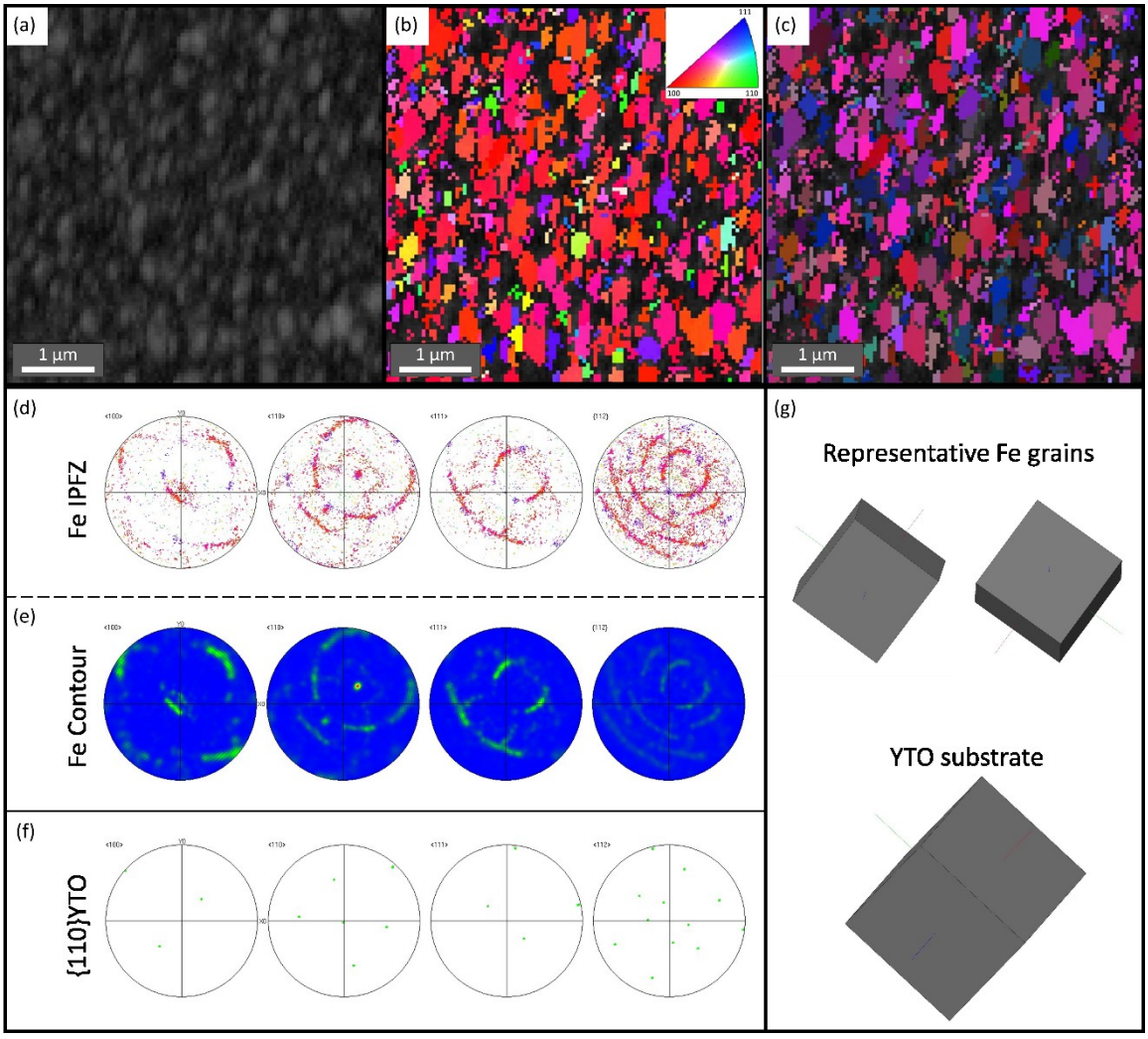

Figure 8.5 – (a) Band contrast, (b) inverse pole figure map and (c) Euler map of the Fe film. (d) Fe pole figures colored according to the out-of-plane orientation, and (e) contour mapping. (f) YTO substrate pole figures. (g) 3D renderings of two Fe grains (top) and YTO substrate (bottom).

8.6 TEM Characterization

Transmission electron microscopy was used to characterize the He-implanted Fe film. Figure 8.6a is a schematic showing the Pt + AlO_x coating, four Fe grains, and {110}YTO substrate for the TEM micrographs in over-focused (Figure 8.5b) and under-focused (Figure 8.5c) conditions. He bubbles are seen as dark dots in the over-focus condition, and as white dots in the under-focus condition. Bubbles are found within the Fe grains and at all boundaries including AlO_x-Fe, Fe-Fe grain boundaries, and Fe-YTO interface. No bubbles were observed in the YTO substrate.

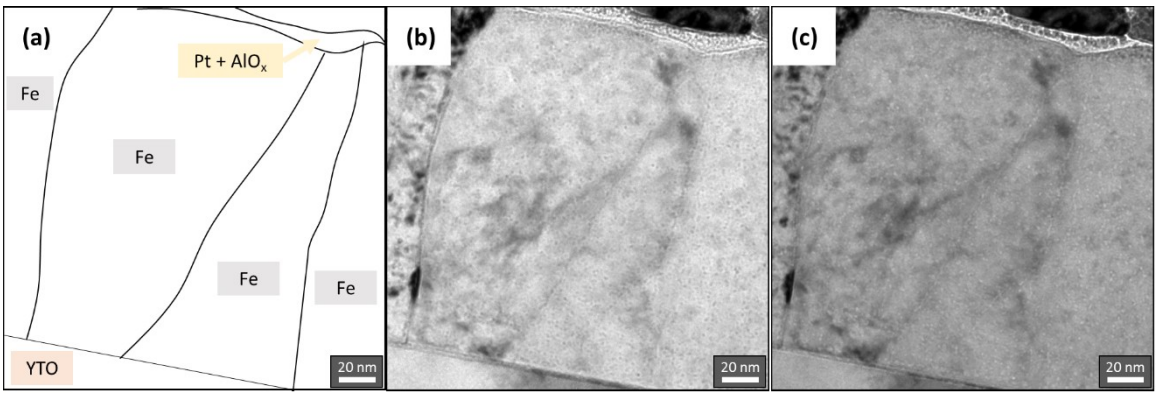

Figure 8.6 – (a) Schematic showing the coating, four Fe grains, and YTO substrate for the (b) over-focus and (c) under-focus TEM images.

Three grains were analyzed in this study. Figure 8.7a is a TEM image taken from one of the Fe grains. The red circles indicate the size and location of He bubbles. The bubble number density and volume fraction was calculated as a function of depth by first splitting the image into 10 nm tall and 90 nm wide sections, indicated by the white boxes in Figure 8.7a. The top 10 nm of the Fe grain has a high number density of small He

bubbles. However, not all grains had this bubble-rich area. The area between 10 nm and 20 nm has fewer but slightly larger bubbles. Below the 20 nm depth, the average bubble size and number density generally increases.

At the Fe-YTO interface, a total of 26 bubbles were observed in the ~125 nm wide section. The bubbles range in size from 1.2 nm to 4 nm, with an average diameter of <d> = 1.8 nm. There does not appear to be a periodic spacing between the bubbles. However, interphase boundaries are difficult to image using conventional TEM due to spherical aberrations and defocus effects. It is possible that under-focusing the beam caused some He bubbles to appear grouped as one large bubble (such as the horizontally elongated red bubble in the center of Figure 8.7a). No bubbles were observed in the YTO substrate.

The average He bubble diameters <d>, number densities <N>, and concentration profiles are shown in Figure 8.7b, c, and d, respectively. Note that the plots are averaged for the three analyzed Fe grains, including the grain in Figure 8.7a. A depth of 0 nm indicates the top surface under the capping layer. In each of the three plots, the data point in red indicates the value at the interface.

The plot in Figure 8.7b shows that the bubble diameters are nearly constant throughout the film, with <d> ≈ 1.5 nm. The bubbles are slightly smaller near the capping layer, and larger at the interface $\langle d \rangle_{if} \approx 2$ nm. No bubbles were observed in the {110}YTO substrate. The number density plot in Figure 8.7c has a u-shape with a sharp drop-off at the interface. <N> is large at shallow depths into the Fe, is minimum at ~ 50 nm, and steadily

increases towards the Fe-YTO interface. The interface itself has a very small number density of bubbles with $\langle N \rangle_{if} = 7.3 \times 10^{23}$ bubbles/m^3.

A hard sphere model was used to estimate the number of He atoms in the bubbles [9]. Experimental calibrations were obtained from a study by Wu et al. which used electron energy loss spectroscopy (EELS) measurements on helium bubbles [10,11]. The model takes into account implantation temperatures (25 °C in this study) and cavity-matrix surface energies (1.8 J/m^2). Figure 8.7d shows the initial implanted He profile in blue, and the experimentally measured profile in black. Overall, the He content increases with proximity to the Fe-YTO interface. The peak concentration is ~3800 appm He at a depth of 150 nm into the Fe. The average measured concentration is ~2800 appm He. This is 33% more than the implanted average concentration (2100 appm He).

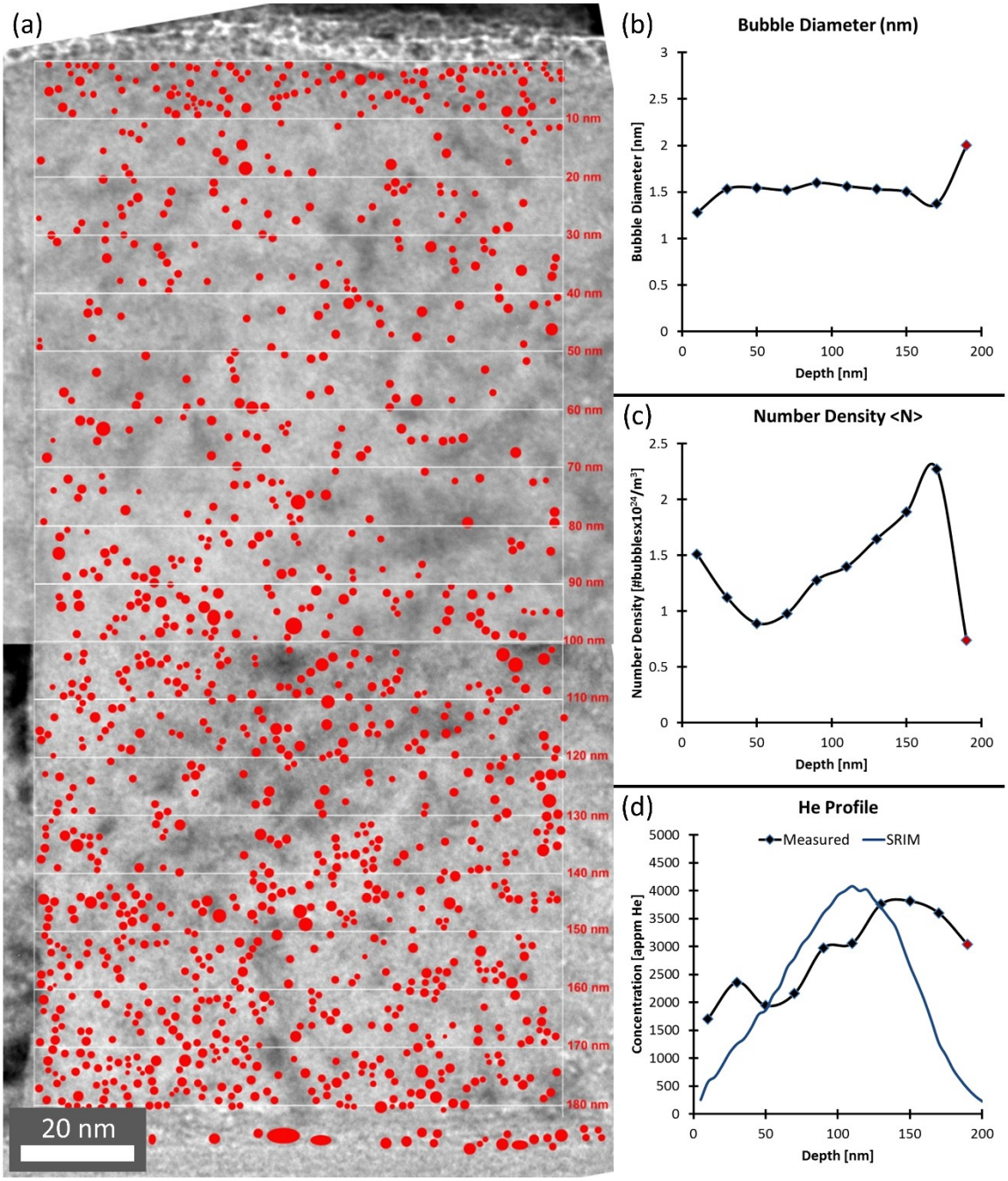

Figure 8.7 – (a) TEM image from an Fe grain. Red circles indicate He bubble size and location. (b) Bubble diameter, (c) number density, and (d) He concentration as a function of depth into the Fe layer. Red data point indicates value at the Fe-YTO interface.

8.7 Discussion

A total of 200 nm of Fe was deposited on {110}YTO. The first 20 nm was slowly deposited using MBE, while the remaining 180 nm was deposited using an electron beam. There was no observable interlayer between the two types of Fe films. The small grains were axiotaxially textured, as expected for Fe-{110}YTO bilayers. He was then implanted at room temperature using a He-ion microscope.

The average bubble diameter was nearly constant throughout the film $\langle d \rangle \approx 1.5$ nm. The bubbles are slightly smaller near the capping layer, and larger at the interface $\langle d \rangle_{if} \approx 2$ nm. Given the high dose rate of 6.25×10^{13} He/(cm^{2}s), and an implantation time of 64 seconds, the He quickly formed bubbles in the Fe layer. Bubbles were not observed in the YTO substrate. It is likely that no He entered the YTO through the interface. However, any He in the YTO may be dissolved throughout the structure, or the bubbles in YTO are too small to see in TEM. More quantitative measurements of the He depth profile are required. Secondary ion mass spectroscopy (SIMS) was used to measure the He concentration in the YTO substrate, but the results were inconclusive and thus not reported here.

The overall He content in the Fe film increases with proximity to the Fe-YTO interface. The average measured concentration in the Fe film is ~2800 appm He, which is 33% more than the implanted average concentration (2100 appm He). This over-estimation is primarily due to errors in identifying the He bubble sizes from TEM images. Red marks were manually placed over bubble locations in the over- and under-focused images. The

accumulation of slightly over-estimated bubble diameters likely led to discrepancies between the measured concentrations and the implanted profile. Regardless, most of the He was accounted for and was trapped in the Fe layer. At room temperature, the He did not have enough energy to diffuse into the YTO substrate. The experiment provides a fundamental basis to model the kinetics of He diffusion and bubble formation for rapid implantation along with a much higher concentration of defects.

8.8 Conclusions

In summary, TDS measurements were performed on room-temperature implanted YTO and Fe single crystals. The peaks from the YTO are present at lower temperatures than those in Fe. Thus, He is more weakly bound to the YTO structure, diffuses faster, and is more easily desorbed from YTO than from Fe.

Regarding the bilayer, a YTO single crystal was first cut, polished, and cleaned in preparation for deposition. 20 nm of Fe was deposited using MBE, followed by 200 nm of electron beam deposited Fe. The sample was then capped with 5 nm of AlO_x and coated with 9 nm of Pt. EBSD analysis showed sub-micron Fe grains with an axiotaxial orientation relationship with the underlying {110}YTO substrate. The bilayer was then implanted with 25 keV He with a dose of $4x10^{15}$ He/cm^2. TEM images show a range of He bubble sizes, number densities, and volume fractions. The bubbles are slightly smaller near the capping layer, and larger at the interface $\langle d \rangle_{if} \approx 2$ nm. No bubbles were seen in the YTO substrate. The results will help inform first principle models of metallic oxide

interfaces, as well as reaction-rate theory models for predicting NFA behavior. The experiment provides a fundamental basis to model the kinetics of He diffusion and bubble formation for rapid implantation along with a much higher concentration of defects.

8.9 Acknowledgements

I would like to thank X. Hu (ORNL) for preparing the Fe single crystal and for all of the TDS measurements, T. Brown (UCSB) and C. Palmstrom (UCSB) for depositions using the interconnected MBE system, Y. Wu (UCSB) for TEM imaging and bubble analysis, and T. Yamamoto (UCSB) and G.R. Odette (UCSB) for guidance and support.

8.10 References

[1] G.R. Odette, M.J. Alinger, B.D. Wirth, Annu. Rev. Mater. Res. 38 (2008) 471–503.

[2] G.R. Odette, JOM 66 (2014) 2427.

[3] Y. Dai, G.R. Odette, T. Yamamoto, The Effects of Helium in Irradiated Structural Alloys, 1st ed., Elsevier Inc., 2012.

[4] L. Yang, Y. Jiang, Y. Wu, G.R. Odette, Z. Zhou, Z. Lu, Acta Mater. 103 (2016) 474–482.

[5] L. Yang, Y. Jiang, G. Robert Odette, T. Yamamoto, Z. Liu, Y. Liu, J. Appl. Phys. 115 (2014) 143508.

[6] R. Kirchheim, Metall. Mater. Trans. A Phys. Metall. Mater. Sci. (2016).

[7] X. Hu, D. Xu, B.D. Wirth, J. Nucl. Mater. (2013).

[8] D. Xu, T. Bus, S.C. Glade, B.D. Wirth, J. Nucl. Mater. (2007).

[9] R.E. Stoller, G.R. Odette, J. Nucl. Mater. 131 (1985) 118–125.

[10] Y. Wu, G.R. Odette, T. Yamamoto, J. Ciston, P. Hosemann, Fusion Semiannu. Rep. 54 (2013).

[11] S. Fréchard, M. Walls, M. Kociak, J.P. Chevalier, J. Henry, D. Gorse, J. Nucl. Mater. 393 (2009) 102–107.

Chapter 9 High Temperature He Implantations

9.1 Introduction

To study the He transport and fate in a controlled fashion, our approach was to deposit Fe on oriented $Y_2Ti_2O_7$ (YTO) single crystal substrates to create bilayers with mesoscopic-scale interfaces that facilitate detailed characterization studies. Ideally, the bilayer interfaces are the same, or similar to, those found in the embedded nano-oxides (NOs). As well as facilitating He and point defect transport and fate studies, characterization of the Fe-YTO interfaces will provide input to first principles interface modeling.

The questions addressed in this chapter are: if He is implanted into a Fe layer, will it diffuse past a Fe-YTO interface, and into the YTO structure itself? What is the distribution and how large are He bubbles in Fe, YTO, and the interface? How much of the implanted He is retained in the bilayers, and how is the rest portioned? Does the Fe-YTO bilayer OR affect the He behavior? The experimental approach is to high-temperature He implant Fe-YTO bilayers.

9.2 Experimental

The details of sample fabrication and characterization techniques are covered in previous chapters. In summary, YTO single crystals were oriented to have {100}, {110} and {111} surfaces and corresponding 2 mm thick wafers were cut from the rod using a wire saw. An Allied Multiprep was used to mechanically polish the wafers using a sequence of diamond lapping films and colloidal silica. The substrates were then Aqua Regia etched and cleaned with acetone, isopropanol, and reverse osmosis water. However, one {110} substrate was Aqua Regia etched and rinsed with only water.

The YTO single crystal wafers were loaded into an electron beam deposition system and heated to 1073 K (800°C) at a rate of 0.166 K/s. After outgassing for 1 h, ~2 μm of Fe was deposited at a rate of ~8 nm/s (250 s total) and chamber pressure of 3 x 10^{-6} torr. After deposition the Fe-YTO bilayers were allowed to sit in vacuum at 1073 K (800°C) for a minimum of 30 min. The bilayers were then slowly cooled to room temperature prior to unloading. The resulting films were characterized using an FEI Quanta 400F field-emission scanning electron microscope (SEM) equipped with an electron backscatter diffraction (EBSD) detector. The bilayers were then cut into ~3 mm x 3 mm cubes, and were coated on all six sides with 1 μm Ni using a sputtering deposition system at Argonne National Laboratory. The Ni coating was added to prevent the escape of He during high temperature implantation.

He implantations were performed at the Ion Beam Implantation Laboratory at Los Alamos National Laboratory. A polished but uncoated single crystal of YTO was high

temperature implanted as a control. Four bilayers were mounted on a 7° tilted wedge to prevent He channeling through low-index Fe crystallographic directions. The assembly was loaded into a TANDEM implanter, pumped down to ~$4x10^{-7}$ Torr, and the temperature was slowly raised to 700° C. The temperature was continuously monitored in three locations: inside the heater, inside the assembly, and <1 mm away from the sample surface. A 1.6 MeV He^{+} ion beam was defocused to cover a 7 mm x 7 mm area. The bilayers were implanted to a fluence of $2.26x10^{16}$ He/cm^2, flux of $1.4x10^{11}$ He/cm^2/s, and implantation time of ~162000 s (~45 hrs).

SRIM/TRIM was used to calculate the He implantation profile (black curve and left vertical axis) and damage profile (red curve and right vertical axis) shown in Figure 9.1. The maximum He concentration is 10797 appm He at a depth of 2.55 μm into the bilayer, or 0.65 μm from the Fe-YTO interface. As is clearly seen in Figure 9.1, the He concentration profile is fully within the Fe layer as we did not want to implant He directly into the interface or YTO substrate. The red curve shows the damage profile, which has a maximum of 0.47 dpa at a depth of 2.52 μm into the bilayer, or 0.68 μm from the Fe-YTO interface. On average, 87 displacements are produced for each implanted He ion. If all of the He would evenly distribute throughout the Fe+Ni layers (3.2 μm thick together) and none would enter the YTO, the average He concentration would be 837 appm.

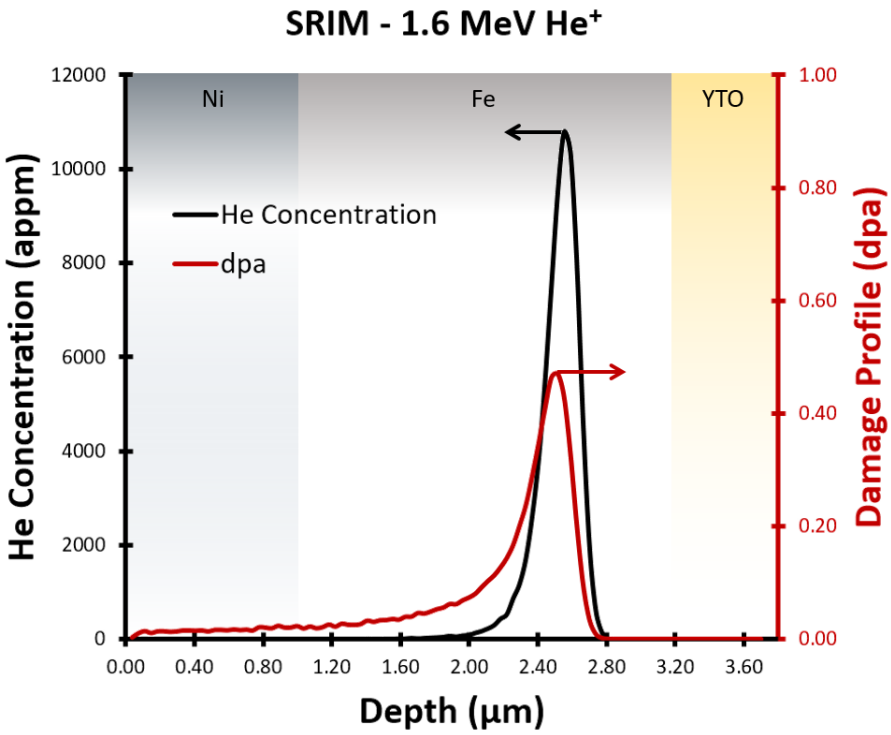

Figure 9.1 – SRIM/TRIM calculated He concentration profile (black curve and left vertical axis) and displacement damage profile (red curve and right vertical axis) for the 1.6 MeV He^+, 2.26x10^6 He/cm^2, implantation into a 1 μm thick Ni coating, 2.2 μm thick Fe film, and arbitrarily thick YTO substrate.

An FEI HELIOS Focus Ion Beam (FIB) tool was used to first deposit ~1 μm of protective platinum over areas of interest. Cross sectional lift-outs of the Fe-YTO bilayers were extracted, thinned to <40 nm, and a low energy 2 keV 5.5 pÅ gallium beam was used for the final cleaning. High-resolution transmission electron microscopy (HRTEM), scanning TEM (STEM), and energy dispersive x-ray (EDX) observations were carried out on a 300 keV FEI Titan TEM at UCSB.

Finally, three of the bilayers were prepared for He spectroscopy measurements at the Pacific Northwest National Laboratory. The samples were sawed in half to create two nearly-identically sized pieces, as shown schematically in Figure 9.2. The red dots and dark semicircles indicate bubbles and pores, respectively (discussed in later sections). Isotope dilution mass spectroscopy was used on one half of each bilayer to measure the total amount of He in the Ni + Fe + YTO sample. The other halves were placed in Aqua Regia for 5 min to remove the Fe and Ni layers. These halves were composed of only YTO substrate. Spectroscopy measurements were used to identify the total amount of He that diffused into the substrates. Finally, the amount of He found in the Ni + Fe layers and pores (discussed in detail in later sections) was calculated by subtracting the two measurements from each other.

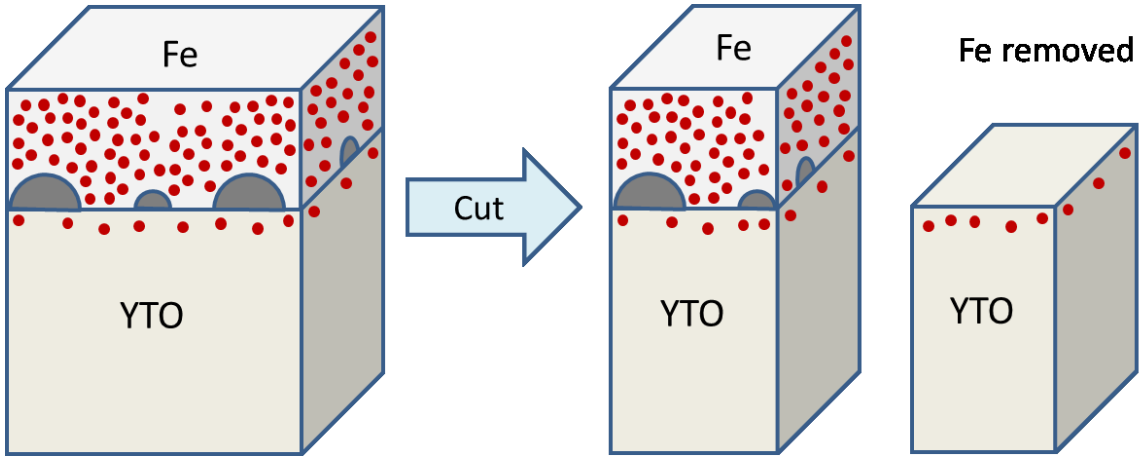

Figure 9.2 – Sample preparation steps for dissolution ion mass spectroscopy.

9.3 SEM and EBSD Characterization

Figure 9.3 contains SEM and EBSD data of the bilayers investigated in this study. The images were taken prior to Ni coating and He implantation, and are named according to the YTO substrate orientation. For example, the Fe-{100}YTO bilayer is a 2 μm Fe film on a {100}YTO oriented substrate. Of the two {110}YTO bilayers, one is termed Fe-{110}YTO etch to identify the unique Aqua Regia etching cleaning step mentioned previously. The scans from the Fe-{100}YTO bilayer are shown in the first column (Figure 9.3a, b, and c), the scans from the Fe-{110}YTO bilayer are shown in the second column (Figure 9.3d, e, and f), etc. The top row in Figure 9.3 contains SEM images of the Fe films. Inverse pole figure Z-direction (IPFZ) maps are shown in the second row, and are colored according to the Fe surface orientation. Green indicates {110} out-of-plane orientations and red indicates {100} orientations. The bottom row contains the same EBSD data as the IPFZ maps, but using an Euler representation where each full crystallographic orientation is assigned a unique color. All nine images show a 20 μm x 20 μm representative surface area and are equally scaled to facilitate side-by-side comparison.

The Fe-{100}YTO bilayer SEM image in Figure 9.3a shows 0.5 μm to 8 μm elongated grains. The EBSD IPFZ map in Figure 9.3b is colored completely green, indicating very strong {110}Fe texturing. Black areas in Figure 9.3b (and in the other EBSD figures) are locations where the Fe orientation could not be indexed, often due to the presence of grain boundaries. The Euler Map in Figure 9.3c is colored pink and orange;

however, there are in fact two shades of pink and two shades of orange, indicating four in-plane variants of the {110}Fe grains (further discussed with Figure 9.4).

Figure 2d shows an SEM image from the Fe-{110}YTO bilayer indicating roughly 2 μm – 4 μm grains. The film surface is not smooth and has visible ledges. The IPFZ map in Figure 9.3e shows orange and pink orientations, although slight coloration variants are also observed. The Euler map in Figure 9.3f shows a red orientation that covers the majority of the Fe film, but patches of the film are colored magenta and purple. These orientations are similar and indicate axiotaxial texturing (further discussed with Figure 9.4).

Figure 9.3g is an SEM image from the Fe-{110}YTO etch bilayer. Grain boundaries are not observed as seen in the Fe-{100}YTO and Fe-{110}YTO bilayers, but 0.5 μm topographical mounds are seen. The IPFZ map in Figure 9.3h is colored completely red, indicating a strong {100}Fe out-of-plane orientation for the entire film. The Euler map in Figure 9.3i shows slight color variations indicating that the film is actually composed of patches of closely oriented grains, roughly the same size as seen in the previous two depositions.

Figure 9.3j is an SEM image of the Fe-{111}YTO bilayer indicating one continuous film. Individual grains are not seen, but the film surface contains ledges similar to those in Figure 9.3d. The EBSD IPFZ map is colored completely red, indicating strong {100}Fe texturing. The Euler map in Figure 9.3l is completely dark red indicating only one continuous orientation without grain boundaries.

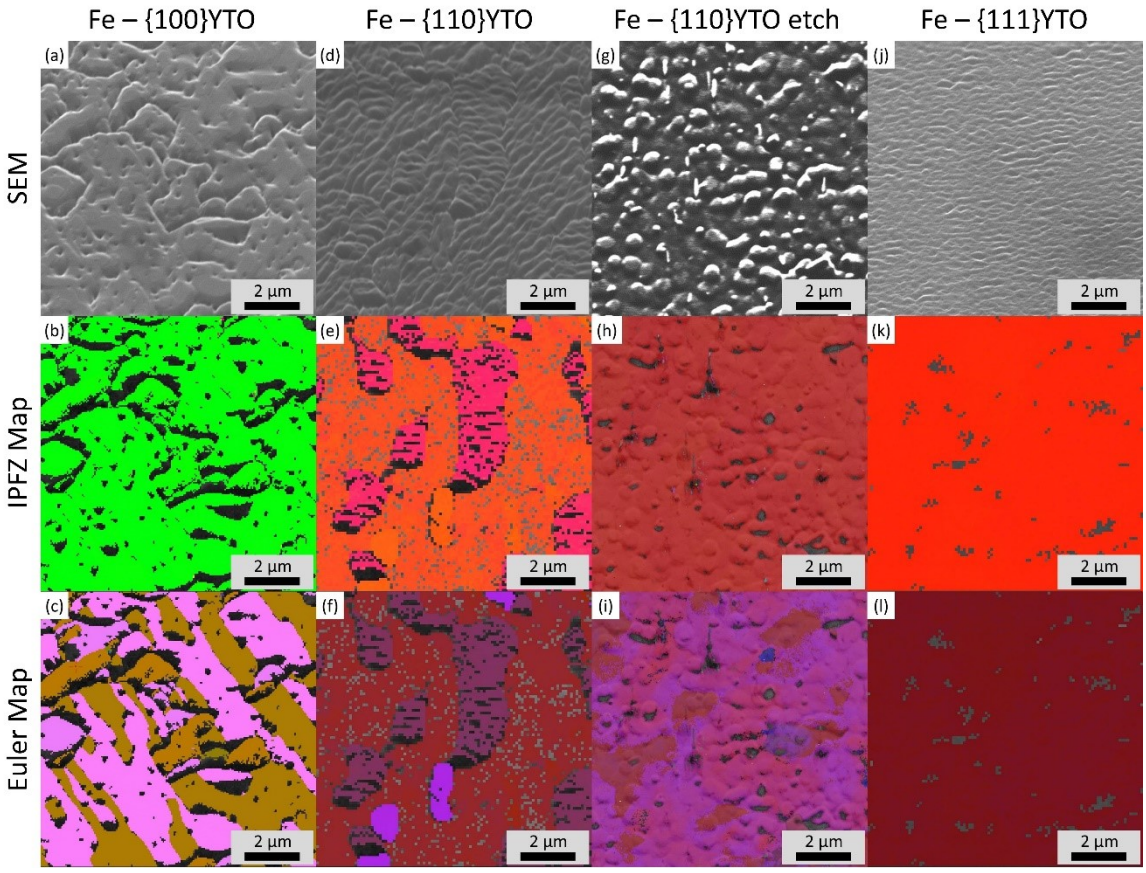

Figure 9.3 – SEM and EBSD data from the bilayers (four columns). SEM images from the Fe surfaces are shown in the top row. EBSD IPFZ maps are shown in the middle row, colored according to the our-of-plane Fe orientation. The bottom row shows Euler maps colored according to the full 3D orientation of each grain.

Figure 9.4 has four columns, one for each bilayer, showing Fe and YTO pole figures (PFs) and the associated 3D representations. The top row in Figure 9.4 contains <100> and <110> PFs from the Fe film. The spots are colored according to the out of plane orientations. The second row contains the same PFs from the top row, but colored according to the Euler representation, better showing differences in in-plane orientations.

The third row contains PFs from the YTO substrates, colored according to the surface orientation. The fourth row in Figure 9.4 shows 3D representations of the Fe variants and the YTO substrate orientation.

The first column in Figure 9.4 contains EBSD data from the Fe-{100}YTO bilayer, and is complimentary to the first column in Figure 9.3. The two PFs in Figure 9.4a show strong {110}Fe texturing, as indicated by the spot in the center of the <110> PF. The Euler PFs in Figure 9.4b contain four colors (pink1, pink2, orange1 and orange2) indicating four in-plane variants of the {110} grains. The <100> PF in Figure 9.4c has a spot at the center, confirming the {100}YTO substrate orientation. Figure 9.4d shows 3D representations of the four {110}Fe variants and the {100}YTO. The film to substrate crystallographic OR is obtained by overlapping the spots from the Fe PFs with those from the YTO PFs. The OR is: {110}Fe//{100}YTO and <111>Fe//<110>YTO, and was observed in previous depositions on {100}YTO. However, this OR has not been observed for embedded NOs.

The second column in Figure 9.4 contains EBSD data from the Fe-{110}YTO bilayer. The streaks in the IPFZ (Figure 9.4e) and Euler (Figure 9.4f) PFs indicate axiotaxial texturing. The spots near the pole figure center are off from {100}Fe by ~ 7°. The presence of a spot in the bottom right quadrant of the <110> Fe PFs indicate that the Fe grains have off-axis rotations about the <110> Fe direction. The YTO PFs in Figure 9.4g indicate a good {110}YTO orientation. The 3D representations in Figure 9.4h show three examples of the Fe orientations along with the YTO substrate. The OR for this film is roughly {104}Fe//{110}YTO, with multiple in-plane variants, some of which have

<100>Fe//<110>YTO. This axiotaxial OR was observed in previous depositions on {110}YTO, but not observed for embedded NOs.

EBSD data from the Fe-{110}YTO etch bilayer are shown in the third column of Figure 9.4. The bilayer has the same substrate orientation as the Fe-{110}YTO sample, but a strong {100}Fe texture as indicated by the center spot in the <100> Fe PFs in Figure 9.4i and Figure 9.4j. The purple, pink, and red spots in Figure 9.4j overlap significantly and do not show the same streaking as in Figure 9.4f. The 3D representations are shown in Figure 3l, and are almost identical to each other. The YTO PFs in Figure 9.4k indicate a well oriented {110}YTO substrate. The Fe-YTO OR for this bilayer is: {100}Fe//{110}YTO and <100>Fe//<110>YTO. This OR was observed in previous depositions and for embedded NOs. However, previous studies show that this Fe orientation is accompanied by a ~2 nm Ca-rich layer at the Fe-YTO interface.

Last, the EBSD data from the Fe-{111}YTO bilayer is shown in the fourth column of Figure 9.4. The PFs indicate a strong {100}Fe texturing, and the YTO PFs in Figure 9.4o confirm the {111}YTO substrate orientation. The Fe and YTO 3D representations are shown in Figure 9.4p. The OR is {100}Fe//{111}YTO and <100>Fe//<110>YTO. This OR was observed in previous depositions but not in embedded NOs.

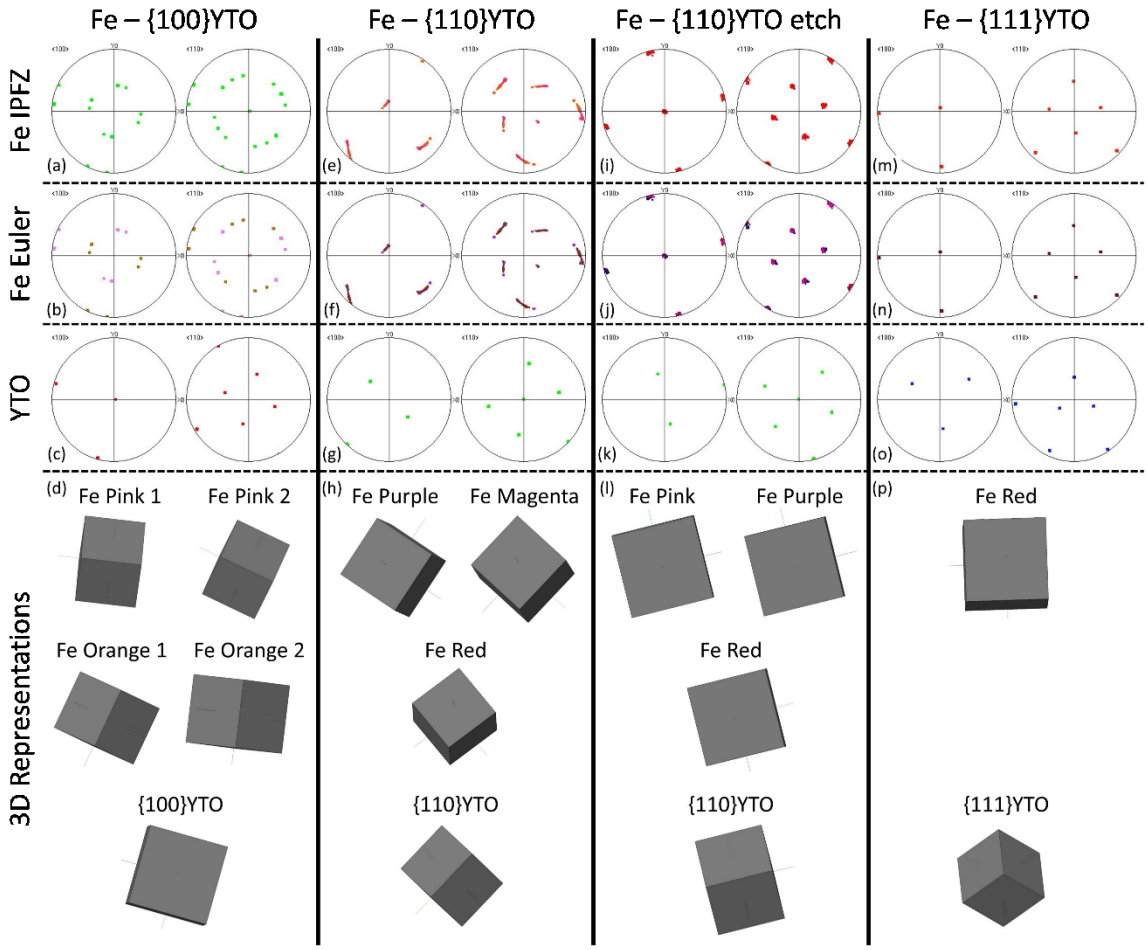

Figure 9.4 – EBSD pole figures (PFs) and 3D representations of the four bilayers observed in this study. The top row indicates Fe PFs colored according to the IPFZ out-of-plane orientation. The second row shows Fe PFs colored according to the Euler orientations. The third row shows IPFZ PFs from the YTO substrate. The bottom row contains 3D reconstructions of the orientations seen in the Euler PFs, showing both Fe and YTO orientations.

9.4 TEM Characterization

Low magnification STEM imaging was used to characterize the bilayer microstructures after the Ni coating and subsequent high temperature He implantation. The multipart Figure 9.5 contains cross-sectional micrographs of the four bilayers. The average film thickness, Fe orientation, YTO orientation and Ni content is indicated in each image. The figures are equally scaled to facilitate side-by-side comparisons.

Figure 9.5a shows the microstructure of the Fe-{100}YTO bilayer. There is no observable interface between the Ni coating and the initial Fe deposition. The Ni and Fe formed one continuous metallic film with an average thickness of ~3.12 μm and with ~0.5 μm wide recrystallized grains. EDX point scans were used to measure the Ni content at four locations along the metallic film as indicated in Figure 9.5a. The Ni content is ~33 at% at the top of the film, and ~24 at% close to the metal-oxide interface. An average of 29 at% Ni is present in the film, which is expected given that the Fe film and Ni coating were initially ~ 2.2 μm and ~1 μm thick, respectively. Notably, there is no Ni inside the YTO substrate. Large cavities are present at the Fe-YTO interface, and are shown in black in the STEM images. The seven interfacial cavities in Figure 9.5a range in size from a few nm^2 to ~0.5 μm x ~2 μm. Vertical dark streaks are observed in the {100}YTO substrate, which are an artifact of the FIB machining. Material is preferentially milled in areas below the cavities.

Figure 9.5b shows the microstructure of the Fe-{110}YTO bilayer. The average film thickness is 3.33 μm, slightly more than the Fe-{100}YTO bilayer in Figure 9.5a.

Again, recrystallized grains are observed in the Fe layer. A gradient in the Ni composition is seen with 41 at% Ni present at the surface and 9 at% Ni at the Fe-YTO interface. Unlike the Fe-{100}YTO bilayer, there are very few cavities at the Fe-{110}YTO interface shown in Figure 4b. Only three cavities are observed, with the largest being ~0.25 μm wide. The two dark holes in the YTO substrate are an artifact of the FIB lift-out sample preparation.

Figure 9.5c shows the microstructure of the Fe-{110}YTO etch bilayer. The initial Fe thickness was ~2.0 μm, thus the resulting metallic film thickness is ~2.93 μm, as expected. Similar to the Fe-{100}YTO bilayer, the Ni distribution is roughly uniform. The Fe-{110}YTO etch bilayer in has largest interfacial cavities observed in this study. The left of Figure 9.5c shows two cavities which have coalesced, a small ~0.3 μm wide cavity, and a large ~2 μm wide cavity.

Figure 9.5d shows the microstructure of the Fe-{111}YTO bilayer. The average film thickness is 3.22 μm, and the Ni concentration varies with proximity to the Fe-YTO interface. The interfacial cavity size is ~0.75 μm, similar to the Fe-{100}YTO bilayer. Four large cavities are observed, the largest being ~1 μm wide.

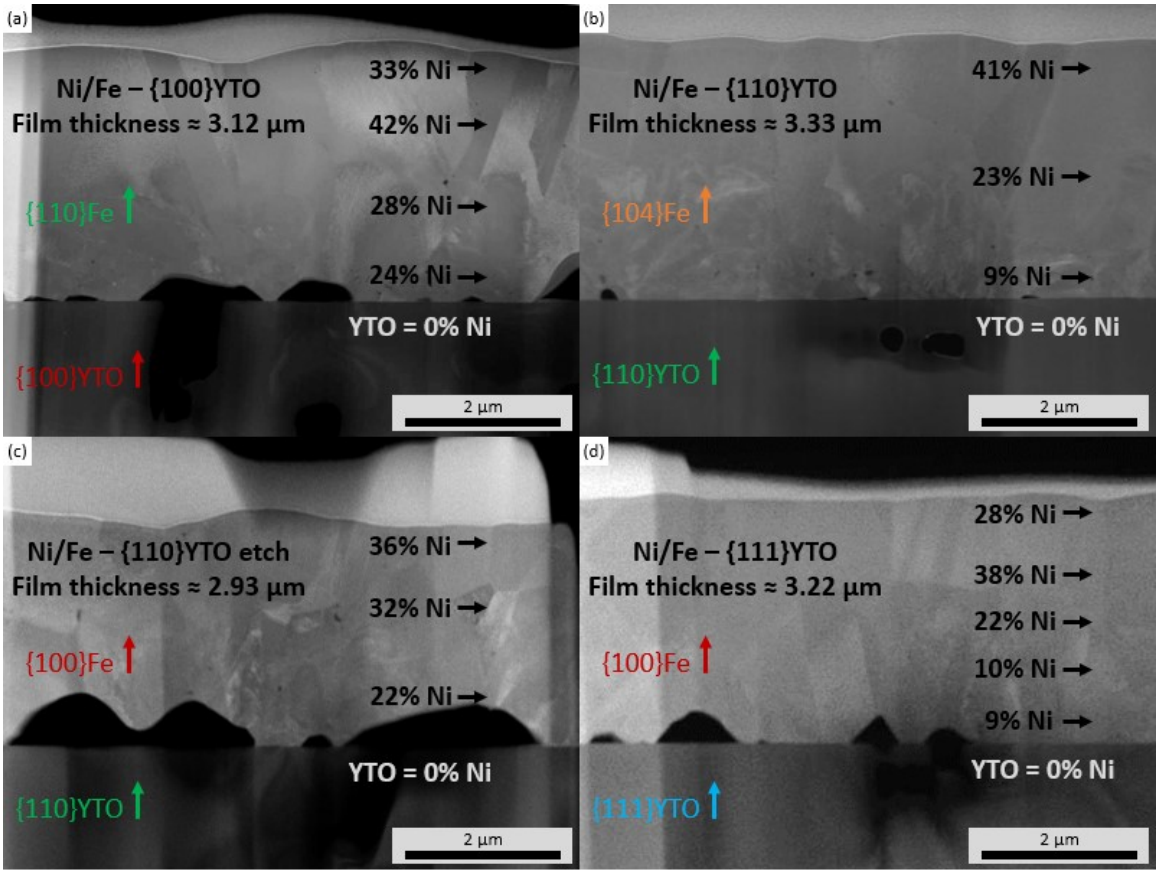

Figure 9.5 – Low magnification cross-section images of the (a) Fe – {100}YTO, (b) Fe – {110}YTO, (c) Fe – {110}YTO etch and (d) Fe – {111}YTO bilayers. The average film thicknesses, Fe orientations, YTO orientations, and at% Ni measurements are indicated in each image.

Figure 9.6a is an underfocused bright field TEM image from the Fe-{100}YTO bilayer. The red marks indicate the size and location of He bubbles. A large d = 31 nm bubble is present at a distance of ~100 nm from the metal-oxide interface; however, the average bubble diameter for the area shown in Figure 9.6a is <d> ≈ 2.4 nm. No bubbles were observed at the Fe-YTO interface. Bubbles are identified by underfocusing or

overfocusing the bright field images. However, this defocusing also enhances contrast of the Fe-YTO interface which convolutes the signal from the bubbles. Possible surface oxide on the TEM lift-out also affects the contrast. Thus a full He inventory cannot be obtained for the Fe-YTO interface. However, we are confident that there are no clearly observable bubbles with d > 2 nm at the metal-oxide interface. Figure 9.6b shows the area below a large cavity in the Fe-{110}YTO etch interface. Small bubbles are clearly seen in the YTO substrate.

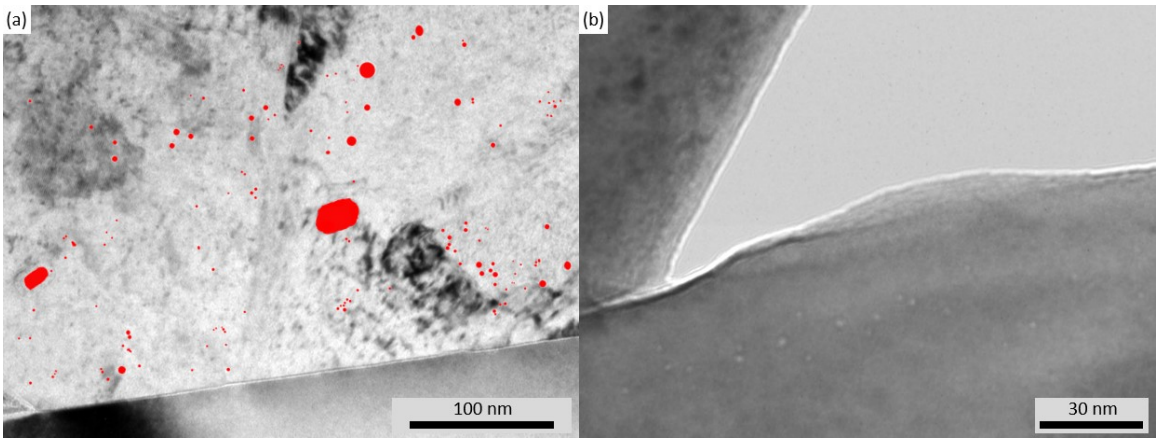

Figure 9.6 – (a) Underfocused bright field TEM image of the Fe-{100}YTO bilayer. Red marks indicate the location and size of He bubbles. (b) TEM image of the area under a large cavity in the Fe-{110}YTO etch bilayer showing the presence of bubbles below the metal oxide interface.

The bubbles in representative sections of all four bilayers were analyzed. The plots in Figure 9.7 indicate the (a) bubble diameters, (b) number densities, and (c) He profiles as a function of distance from the Fe-YTO interfaces. The data for each bilayer was split into two charts for clarity.

Figure 9.7a shows the bubble diameters d in the bilayers. The average <d> for the entire Ni/Fe layers are 3.03 nm, 4.71 nm, 3.18 nm, and 4.30 nm for the 100YTO, 110YTO, 110YTO etch, and 111YTO bilayers, respectively. The bubble size slightly increases with depth or the Fe-110YTO bilayer, while it slightly decreases for the Fe-111YTO bilayer. Overall, there are no clear trends relating bubble sizes and proximity to the Fe-YTO interfaces.

Figure 9.7b shows the bubble number densities N calculated as number of bubbles per volume. The average <N> for the Fe layers are 2.21×10^{-5}, 7.06×10^{-5}, 2.12×10^{-5}, and 1.64×10^{-5} bubbles/nm^3 for the 100YTO, 110YTO, 110YTO etch, and 111YTO bilayers, respectively. Overall, there is a slight increase in bubble density as a function of distance from the metal-oxide interface. However, the trends are more closely associated with variations in microstructure. For example, the Fe-100YTO bilayer has a peak bubble diameter of d = 7.59 nm at a distance of 1.2 μm from the interface. This is due to the presence of a grain boundary that locally contains larger bubbles than the rest of the metallic film.

Figure 9.7c shows the total He count at different depths in the sample. Note that the He profile for the Fe-111YTO bilayer is scaled differently. The number of He atoms per bubble was calculated using a calibrated equation of state model which accounts for the implantation temperature (700 °C). The average He concentrations are 505 appm He, 357 appm He, 414 appm He, and 2202 appm He for the 100YTO, 110YTO, 110YTO etch, and 111YTO bilayers, respectively. Note that the number of He atoms in a bubble increases

exponentially with the bubble radius. The variations in He content are mostly due to the presence of large bubbles at microstructural features such as grain boundaries. There are no clear trends relating the bubble size to the proximity of the Fe-YTO interface.

The Fe-111YTO bilayer has a much higher He content than the other three bilayers. One explanation is that the bubble-rich region observed in this TEM lift-out is not representative of the full metallic film. The surrounding part of the metallic layer may have less He. Another possibility is that some of the spherical microstructural features (especially atypically large ones) may not be bubbles, but precipitates of a second phase. Further analysis is required. An average concentration of 837 appm He was implanted into the bilayers. The amount of He retained in the form of bubbles within the Fe films is 60%, 43%, and 49% for the 100YTO, 110YTO, and 110YTO etch bilayers, respectively.

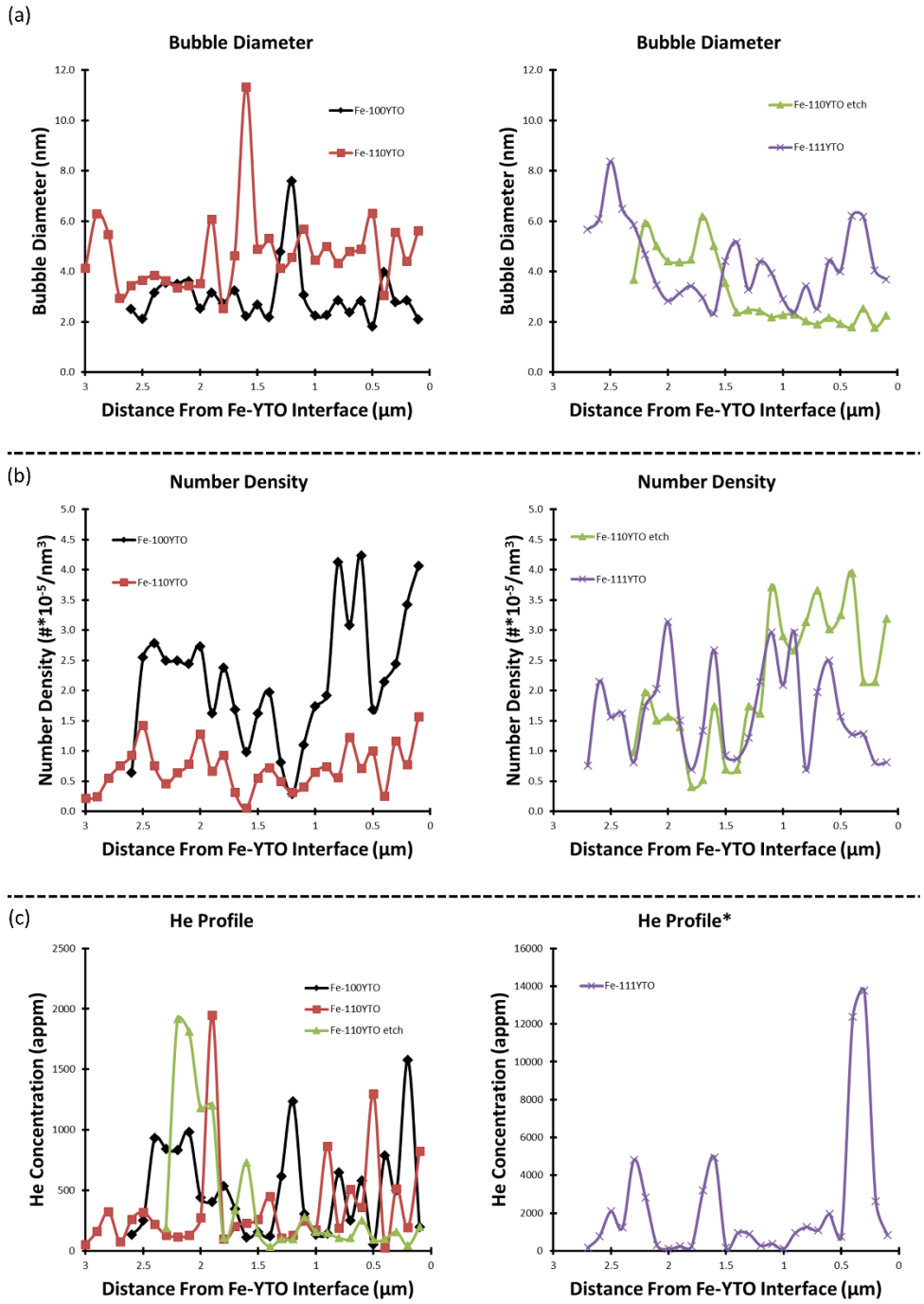

Figure 9.7 – Bubble analysis from the four bilayers. (a) Bubble diameter, (b) number density, and (c) He profile as a function of distance from the Fe -YTO interface. *Note that the He profile for the Fe-111YTO bilayer is on a different scale from the rest.

9.5 Isotope Dilution Mass Spectroscopy

Isotope dilution mass spectroscopy was used to measure He contents in the samples. First, a high temperature He implanted single crystal YTO was measured. Of the ~$1.1x10^{15}$ He atoms implanted into the crystal, ~$1.14x10^{14}$ He atoms remained. Thus, the ~2 mm thick crystal retained 10% of the implanted He. The rest diffused out of the sample.

Three bilayers (Fe-{100}, Fe-{110}, and Fe-{111}YTO) were first cut prior to measurements. The first halves were measured to obtain how much of the implanted He remained in the bilayers. The following values are an average of all three bilayer measurements. Of the 837 appm He implanted, 84% (703 appm He) remained in the bilayer. The remaining 16% might have diffused out of the samples during implantation. The values are within experimental uncertainties. The second bilayer halves were Aqua Regia treated to remove the Ni, Fe, and interfacial pores. This allowed for measurements of the He content present in the YTO substrates alone. The measured amounts are 0.7% (4.9 appm He) of the total present, as averaged for all three bilayers.

Combining the mass spectroscopy measurements with the TEM bubble observations, the He partitioning was obtained. The results are summarized in Figure 9.8 where pores are shown in dark gray, and bubbles are represented in red. 73% (505 appm He) was measured in bubbles, while the remaining 27% (186 appm He) was in the micron-sized pores. In the YTO, 28% (1.5 appm He) was accounted for in YTO bubbles, while the remaining 72% (3.4 appm He) was dissolved throughout the YTO.

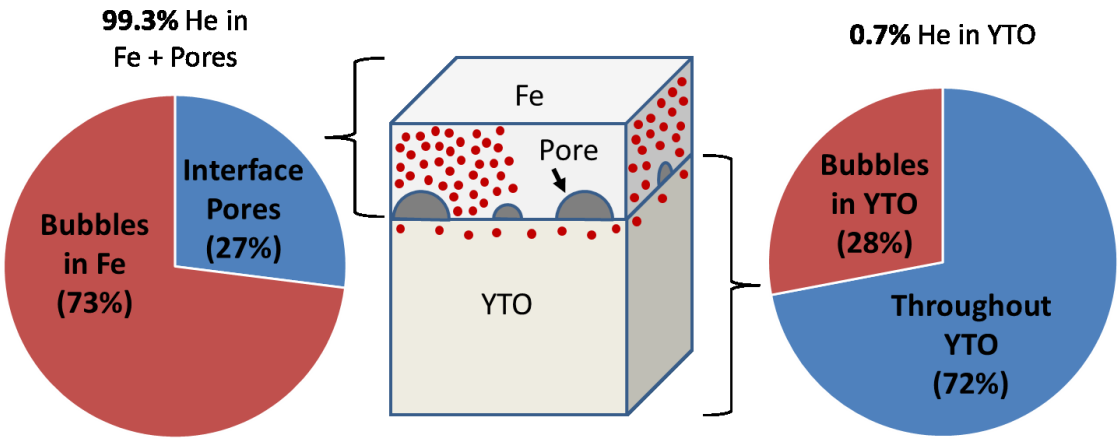

Figure 9.8 – Summary of helium inventory. Of the 837 appm He implanted, 84% (703 appm He) of the total was accounted for in bilayers. Of that, 99.3% remained in Fe - 73% (505 appm He) in bubbles and 27% (186 appm He) in pores. 0.7% of the total He was measured in the YTO substrate - 28% (1.5 appm He) in bubbles and 72% (3.4 appm He) dissolved throughout the structure.

9.6 Discussion

Mesoscopic-scale bilayer interfaces were fabricated by electron beam deposition of Fe films on {100}, {110}, and {111} $Y_2Ti_2O_7$ bulk single crystal substrates. Four Fe-YTO orientation relationships were observed. After encapsulating the bilayers with Ni, the Fe films were high temperature (700 ˚C) ion implanted using 1.6 MeV He^+ to a dose of $2.26x10^{16}$ He/cm^2.

Two observations were made by comparing the low-magnification TEM images of the four bilayers. First, there is an inverse relationship between the film thickness and the interfacial pore size. The Fe-{110}YTO bilayer which has the thickest film (~3.33 μm) has

the fewest and smallest interfacial pores, while the Fe-{110}YTO etch bilayer has the thinnest film (~2.93 μm) and has the largest pores. Note that during FIB fabrication of the TEM lift-outs, the interfacial pores are preferentially milled by the gallium beam. Thus, the actual cavity sizes in the Fe-YTO film are slightly smaller than what is seen in Figure 9.5. Second, there is a correlation between the uniformity in Ni concentration and the pore size. The two bilayers with nearly-uniform Ni distributions have large pores, while the bilayers with a gradient in Ni concentration have smaller pores. Also, the thicker films have a larger concentration gradient than the thin films. Diffraction pattern analysis of the Ni/Fe layer indicates that the film is no longer bcc α-Fe. The known phases in the Ni-Fe binary system are mostly fcc with lattice parameter of ~3.5 Å [3–5]. The metastable Fe_3Ni phase which has the fcc $L1_2$ structure is of particular interest as it has a composition close to that of the Ni/Fe film (33% Ni). However, the diffraction pattern from the Ni/Fe film does not have the symmetry expected in a cubic system, and requires further analysis.

The presence of interfacial pores can be explained by the Kirkendall effect. Diffusion couples may exhibit porosity if the two elements diffuse into each other at different rates. In the case of Fe and Ni, the intrinsic diffusion coefficient for Fe is higher than the coefficient for Ni [6]. Thus, the flux of Fe atoms moving toward the Ni coating is balanced by the fluxes of Ni atoms and vacancies moving toward the Fe-YTO interface. The interface acts as a heterogeneous nucleation site for the large pores. Furthermore, the closer the initial Ni coating is to the interface, the less distance the vacancies travel before nucleating a cavity, and the sooner the pores begin to grow. Thus, as was observed in the

experiment, bilayers with a thinner Fe layer have larger interfacial pores. An estimated intrinsic diffusion coefficient for Ni in Fe at 1500 K is $D'_{Ni} \approx 2.2\text{x}10^{-14}$ m^2/s [6], and the implantation time in this experiment is $t \approx 1.6\text{x}10^5$ s. As a first order approximation, the characteristic diffusion distance for Ni is $x = \sqrt{(D'_{Ni}t)} = 0.06$ μm. The Ni diffused much further into the Fe layer (2 μm), thus the observed microstructure and interfacial cavities are due to radiation enhanced diffusion.

The high magnification TEM images show bubbles in the Fe layers and in the YTO substrate. Bubbles with diameters greater than 2 nm were not observed at the interfaces. Also, the interface orientation relationship did not have a clear effect on the He behavior. The He bubble sizes and distributions were roughly similar between the four samples.

The full He partitioning is obtained by combining the mass spectroscopy measurements with TEM observations. It was observed that 99.3% of the He remained in the metallic layer and Kirkendall pores while 0.7% of the implanted He went into the YTO substrate. Of that, ~72% of the He was in bubbles in Fe, ~27% in pores, and the rest in the YTO. In both the metallic layers and in the YTO, most of the He was present in bubbles.

A summary of the possible scenarios and fates of the implanted He is shown in Figure 9.9. In all cases, He atoms were implanted into the metallic layer and initially diffuse interstitially though the lattice. In scenario (a) the He atoms cluster and nucleate bubbles in the Fe layer. This scenario was the most common, as bubbles in Fe account for ~73% of the total He in the system. In scenario (b) He atoms diffuse through the lattice and encounter an interfacial pore. The He atoms enter the pore as their energy will be much

lower than in the metallic lattice. Also, that the largest pores grew to sizes > 1 μm which overlaps with the He peak implantation region. Thus some amount of He was implanted directly into the pores. In scenarios (c), (d), and (e), He atoms enter the YTO substrate and are unable to diffuse back into the Fe layer. It is known that the energy of He in YTO (0.94 eV/atom) is much lower than in Fe (2.28 eV/atom) [1,2]. In scenario (c) He atoms diffuse into the YTO substrate, and then into the interfacial pores where they are permanently trapped. In scenario (d) He atoms diffuse into the YTO substrate and remain dissolved throughout the pyrochlore structure. In scenario (e) He atoms diffuse into the YTO substrate and form small bubbles below the metal-oxide interface.

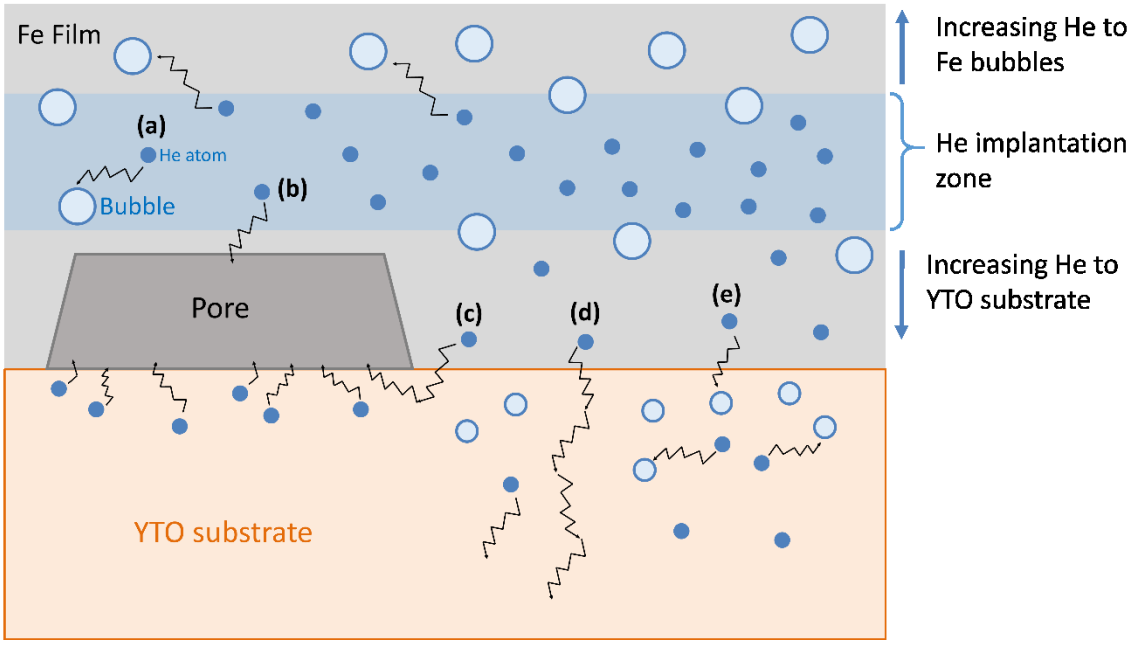

Figure 9.9 – Summary of possible fates for the implanted He. (a) He is trapped in bubbles in the Fe layer. (b) He diffuses to interfacial pores. (c) He diffuses into the YTO substrate, and then into the interfacial pores. (d) He diffuses into the YTO substrate and remains in

the structure. (e) He diffuses into the YTO substrate and is trapped in sub-interface bubbles.

The presence of the Kirkendall pores confounded the simple setup of the experiment. Although most of the He trapped in the interfacial pores likely diffused from the YTO substrate (process (c) in Figure 9.9), some He might have entered the pores directly from the Fe layer (process (b) in Figure 9.9). The partitioning of He could not be reported with the desired accuracy. However, the experiment clearly indicates that at high temperatures, He diffuses past the metal-oxide interface and into the YTO substrate. Future experiments will use a Cu coating instead of Ni to avoid the formation of Kirkendall pores.

9.7 Conclusions

In summary, mesoscopic-scale bilayer interfaces were fabricated by electron beam deposition of Fe films on {100}, {110}, and {111} $Y_2Ti_2O_7$ (YTO) bulk single crystal substrates. Four Fe-YTO orientation relationships were observed. After encapsulating the bilayers with Ni, the Fe side was high temperature (700 ˚C) ion implanted using 1.6 MeV He^+ to a dose of $2.26x10^{16}$ He/cm^2. Radiation enhanced diffusion led to the intermixing of Ni and Fe, and to the formation of 1 μm Kirkendall pores at the Fe-YTO interfaces. Further, He bubbles were seen in all of the films, as well as in the YTO substrates up to a depth of 80 nm. No bubbles were observed at the metal-oxide interfaces. Most of the He remained in the Fe layer, but ~ 27% was found in interfacial Kirkendall pores. Importantly

it is shown that at high temperatures, He diffuses past the metal-oxide interface and into the YTO substrate.

9.8 Acknowledgements

I would like to thank H. Zhou (UT) for supplying the YTO single crystals, D. Stave (UCSB) for helping with electron beam deposition, Y. Wang (LANL) for He implantations, Y. Wu (UCSB) for TEM imaging, R. Cox (PNNL) and I. Burgeson (PNNL) for spectroscopy measurements, and R. Kurtz (PNNL) and G.R. Odette for guidance and support.

9.9 References

[1] L. Yang, Y. Jiang, Y. Wu, G.R. Odette, Z. Zhou, Z. Lu, Acta Mater. 103 (2016) 474–482.

[2] L. Yang, Y. Jiang, G. Robert Odette, T. Yamamoto, Z. Liu, Y. Liu, J. Appl. Phys. 115 (2014) 143508.

[3] G. Cacciamani, A. Dinsdale, M. Palumbo, A. Pasturel, Intermetallics 18 (2010) 1148–1162.

[4] T. Mohri, Y. Chen, Y. Jufuku, Calphad 33 (2009) 244–249.

[5] R.A. Howald, Metall. Mater. Trans. A 34 (2003) 1759–1769.

[6] H. Strandlund, H. Larsson, Acta Mater. 52 (2004) 4695–4703.

Chapter 10 Conclusions

10.1 Embedded Nano-Oxides

The chemistries and structures of nano-oxides (NOs) in nanostructured ferritic alloy (NFA) MA957 were characterized by x-ray absorption spectroscopy (XAS) for both embedded and extracted precipitates. Measurements on embedded NOs in bulk MA957 are most consistent with $Y_2Ti_2O_7$ (YTO), while the slightly larger extracted oxides are primarily consistent with Y_2TiO_5. Analysis of the as-received MA957 was difficult due to the multiple Ti environments including $Y_2Ti_2O_7$, Y_2TiO_5, TiO, and dissolved metallic Ti. The bulk extraction and selective filtration technique successfully removed the matrix, trapped the larger Y_2TiO_5 particles, and yielded samples well suited for XAS measurements. The smaller $Y_2Ti_2O_7$ oxides passed through the filters but were the predominant embedded phase. To better study the interactions of He with embedded YTO precipitates, a 14YWT alloy was annealed to coarsen the NOs, and He implanted to produce bubbles. High resolution transmission electron microscopy shows two dominant orientation relationships (ORs): cube-on-edge and cube-on-cube. The smaller NOs are associated with smaller bubbles, while some of the largest NOs (>6 nm) often have two bubbles. Most bubbles nucleate at {111} NO facets. Importantly, the interfacial edge-on-corner OR: {110}Fe//{111}NO with <100>Fe//<110>NO where bubbles are found is the is

also the dominant OR for thin film Fe deposition on {111} $Y_2Ti_2O_7$ single crystal substrates [1].

10.2 Fabrication of Fe-YTO Bilayers

The embedded cuboidal NOs have multiple interfacial ORs, usually with low index {100}, {110}, and {111} YTO planes bonded to the surrounding matrix. Detailed characterization and analysis of the NO-matrix interfaces is needed to develop first principles and atomic-scale models that are part of multi-scale efforts to predict the behavior of NFAs during processing and in irradiation service environments. Thus, Fe was deposited on bulk single crystal YTO to create mesoscopic-scale interfaces that in principle are easier to study than those found in embedded NOs.

Most Fe grains on {111}YTO have the Nishiyama-Wasserman OR: {110}Fe//{111}YTO and <100>Fe//<110>YTO and are atomically clean with no significant transition layer, and have strained regions at ledges due to the miscut substrates. Grains with the {100}Fe//{111}YTO and <100>Fe//<110>YTO OR have a 2-3 nm transition layer at the interface. Grains with no OR have a thick transition layer. Finally, both types of ORs have <100>Fe directions that match one of the three <110> directions of the {111}YTO substrate plane.

Mesoscopic epitaxial Fe-YTO bilayers were successfully fabricated by electron beam Fe on {100} YTO single crystal surfaces. We report for the first time, the dominant fine grained polycrystalline OR is {110}Fe\\{100}YTO and <111>Fe\\<110>YTO with

four variants that match the underlying substrate symmetry. High resolution transmission electron microscopy (HRTEM) showed a semicoherent interface with misfit dislocation spacing of ~ 0.7 nm, consistent with CrystalMaker analysis. In contrast, a larger monocrystalline Fe grain had the {100}Fe\\{100}YTO and <100>Fe\\<110>YTO OR that is also found in embedded NOs. HRTEM showed a semicoherent monocrystalline bilayer interface with misfit dislocation spacing of ~ 1.4 nm, and APT results indicate a clean interface. Unlike the monocrystalline patch, which was only observed on one bilayer sample, the polycrystalline OR is highly reproducible in electron beam deposition of Fe on {100} YTO.

A systematic study was done to investigate the structures, ORs, and chemistries of Fe films on {110}YTO substrates. In some depositions, {100}Fe films with a favorable OR as seen in embedded NOs was obtained. However, this orientation was usually accompanied by a contaminant interfacial layer. The use of de-ionized (DI) water and careful rinsing steps proved to be the beast procedure for obtaining clean Fe-YTO interfaces. The effects of YTO substrate chemical termination were studied using in-situ cleaning methods. Ozone was used to oxidize the YTO surface, while hydrogen cleaning was used to reduce the surface. Further, 2 monolayers of Ti were deposited prior to Fe deposition to force a cation-rich termination. None of the in-situ treatments yielded the {100}Fe texturing observed in embedded NOs. This implies that the cube-on-edge {100}Fe//{110}YTO embedded interface is largely due to lattice matching effects, not chemical effects. In all cases, the dominant Fe film orientation was axiotaxial with off-

normal {110}Fe planes parallel to off-normal {100}YTO planes. The 11.3° inclination away from {100}Fe texturing allowed for a fully coherent interface between the Fe and YTO. Rotations about the <110> direction lead to streaks observed in pole figures. If the {110}YTO substrate could be strained, it is possible that the Fe orientations would also approach {100}Fe, as seen in embedded NOs.

10.3 Helium Implantation of Fe-YTO Bilayers

One {110} YTO single crystal was cut, polished, and cleaned in preparation for deposition. 20 nm of Fe was deposited using molecular beam epitaxy (MBE), followed by 200 nm of electron beam deposited Fe. The sample was then capped with 5 nm of AlO_x and coated with 9 nm of Pt. Electron backscatter diffraction (EBSD) analysis showed sub-micron Fe grains with an axiotaxial orientation relationship with the underlying {110}YTO substrate. The bilayer was then implanted with 25 keV He with a dose of $4x10^{15}$ He/cm^2. TEM images show a range of He bubble sizes, number densities, and volume fractions. The bubbles are slightly smaller near the capping layer, and larger at the interface $\langle d \rangle \approx 2$ nm. No bubbles were seen in the YTO substrate. The results will help inform first principle models of metallic oxide interfaces, as well as reaction-rate theory models for predicting NFA behavior.

Finally, mesoscopic-scale bilayer interfaces were fabricated by electron beam deposition of Fe films on {100}, {110}, and {111} $Y_2Ti_2O_7$ (YTO) bulk single crystal substrates. Four Fe-YTO orientation relationships were observed. After encapsulating the

bilayers with Ni, the Fe side was high temperature (700 ˚C) ion implanted using 1.6 MeV He^+ to a dose of $2.26x10^{16}$ He/cm^2. Radiation enhanced diffusion led to the intermixing of Ni and Fe, and to the formation of 1 μm Kirkendall pores at the Ni/Fe-YTO interfaces. Further, He bubbles were seen in all of the Ni/Fe films, as well as in the YTO substrates up to a depth of 80 nm. No bubbles were observed at the metal-oxide interfaces. Most of the He remained in the Fe layer and in Kirkendall pores. Importantly, unlike the low-temperature He implantation in the previous chapter, here He did diffuse through the metal-oxide interface and formed bubbles in the YTO substrate.

10.4 Closing Remarks and Future Studies

Nuclear fusion is a promising option for generating very large amounts of energy. The identification of first-wall and blanket structures capable of withstanding high heat fluxes and intense radiation environments is central to meeting the immense material challenges. The Fe-Cr-based NFAs are thermally stable up to 900 °C and remarkably irradiation tolerant [2–5]. NFAs typically contain a high number density (5×10^{23}/m^2) of Y-Ti-O nano-oxides (NOs) with average diameters $\langle d \rangle \approx 2.5$ nm [2,3]. The NOs impede dislocation climb and glide, stabilize dislocation and grain structures, and trap He in fine-scale bubbles at matrix-NO interfaces [2,5,6]. The high density of small bubbles prevents the formation of growing voids, and decreases He accumulation at grain boundaries which otherwise degrade the dimensional stability, creep, and fracture properties of most

structural alloys. The NOs, and especially the He bubbles, also act as recombination sites for vacancies and self-interstitial defects, thereby promoting radiation damage self-healing.

Research to characterize NO compositions, misfit strains, core shell structures, interface characteristics, and NO-matrix orientation relationships (ORs) is ongoing [7–11]. The research in this dissertation has added to the already growing knowledge-base of NFA characterization and functionality. Most of the smallest NOs are $Y_2Ti_2O_7$ (YTO) fcc pyrochlore [9–18]. The cuboidal NOs have multiple interfacial ORs, usually with low index {100}, {110}, and {111} YTO planes bonded to the surrounding matrix. Detailed characterization and analysis of the NO-matrix interfaces is needed to develop first principles and atomic-scale models that are part of multi-scale efforts to predict the behavior of NFAs during processing and in irradiation service environments. YTO-matrix ORs are of particular interest because they impact selection of compositions and processing paths, service stability, mechanical properties and irradiation tolerance of NFAs. Interface characteristics of interest include structures, local chemistries, defects, misfit strains, energies and NO interactions with He.

Some questions have been addressed in this dissertation, such as: what are the NO chemistries and structures? Are there compositional differences between small and large NOs? What are the bulk and interfacial ORs between embedded NOs and the ferrite matrix? What are the preferred bubble nucleation sites at the NO-matrix interfaces? Is there a relationship between NO size and bubble size? Do multiple bubbles nucleate on

NOs? What is the fate of He between YTO, the ferritic matrix, and the associated interface?

Future studies include:

- XAS characterization of the fluid that passed through the 10 μm filters. It is expected that many of the smallest $Y_2Ti_2O_7$ NOs were present in the fluid.
- Electron energy loss spectroscopy (EELS) measurements of He densities in bubbles in NOs. The annealed and He implanted alloys are ideal for experimentally measuring the quantities of He in bubbles of different sizes.
- Determination of experimental parameters to reliably produce {100}Fe films on YTO substrates. In this work, substrate cleaning procedures were developed to obtain high quality Fe films. Although the {100}Fe grains are now known to be caused by contaminations, it has not been determined what exactly those contaminations are, and how to prepare substrates to reliably obtain {100}Fe if the necessity arises.
- High temperature He implantations of Fe-YTO bilayers that are coated with Cu instead of Ni. The Ni coatings alloyed with the Fe films and led to the formation of Kirkendall pores at the Fe-YTO interfaces. A Cu coating would not react with the metallic film, and still trap He inside the bilayer system. The partitioning of he between Fe, YTO and interface could be clearly reported.

The characterizations and observations performed on NFAs provide crucial insight into the development and optimization of NFAs. By reporting, for the first time, the structures and chemistries of Fe depositions on YTO substrates, we have advanced the

complex and ever-evolving field of metal-oxide interfaces. The studies performed in this dissertation provide crucial experimental inputs for the development of computational models that accurately predict NFA in-service behavior. The results provide an important step into turning the promise of fusion energy into a reality.

10.5 References

[1] T. Stan, Y. Wu, G.R. Odette, K.E. Sickafus, H.A. Dabkowska, B.D. Gaulin, Metall. Mater. Trans. A Phys. Metall. Mater. Sci. 44 (2013) 4505–4512.

[2] G.R. Odette, JOM 66 (2014) 2427.

[3] G.R. Odette, M.J. Alinger, B.D. Wirth, Annu. Rev. Mater. Res. 38 (2008) 471–503.

[4] N. Cunningham, Y. Wu, D. Klingensmith, G.R. Odette, Mater. Sci. Eng. A 613 (2014) 296–305.

[5] Y. Dai, G.R. Odette, T. Yamamoto, The Effects of Helium in Irradiated Structural Alloys, 1st ed., Elsevier Inc., 2012.

[6] G.R. Odette, D.T. Hoelzer, JOM 62 (2010) 84–92.

[7] E.A. Marquis, Appl. Phys. Lett. 93 (2008) 10–13.

[8] S. Liu, G.R. Odette, C.U. Segre, J. Nucl. Mater. 445 (2014) 50–56.

[9] V. Badjeck, M.G. Walls, L. Chaffron, J. Malaplate, K. March, J. Nucl. Mater. 456 (2015) 292–301.

[10] Y. Wu, J. Ciston, S. Kräemer, N. Bailey, G.R. Odette, P. Hosemann, Acta Mater. 111 (2016) 108–115.

[11] Y. Miao, K. Mo, B. Cui, W. Chen, M.K. Miller, K.A. Powers, V. Mccreary, D. Gross, J. Almer, I.M. Robertson, J.F. Stubbins, Mater. Charact. 101 (2015) 136–143.

[12] J. Ribis, Y. De Carlan, Acta Mater. 60 (2012) 238–252.

[13] J. Ribis, S. Lozano-Perez, J. Nucl. Mater. 444 (2014) 314–322.

[14] K. Dawson, G.J. Tatlock, J. Nucl. Mater. 444 (2014) 252–260.

[15] M. Tamura, H. Sakasegawa, K. Shiba, H. Tanigawa, K. Shinozuka, H. Esaka, Metall. Mater. Trans. A 42 (2011) 2176–2188.

[16] Y. Wu, E.M. Haney, N.J. Cunningham, G.R. Odette, Acta Mater. 60 (2012) 3456–3468.

[17] A.J. London, B.K. Panigrahi, C.C. Tang, C. Murray, C.R.M. Grovenor, Scr. Mater. 110 (2016) 24–27.

[18] R. Kasada, N. Toda, K. Yutani, H.S. Cho, H. Kishimoto, A. Kimura, J. Nucl. Mater. 367–370 A (2007) 222–228.